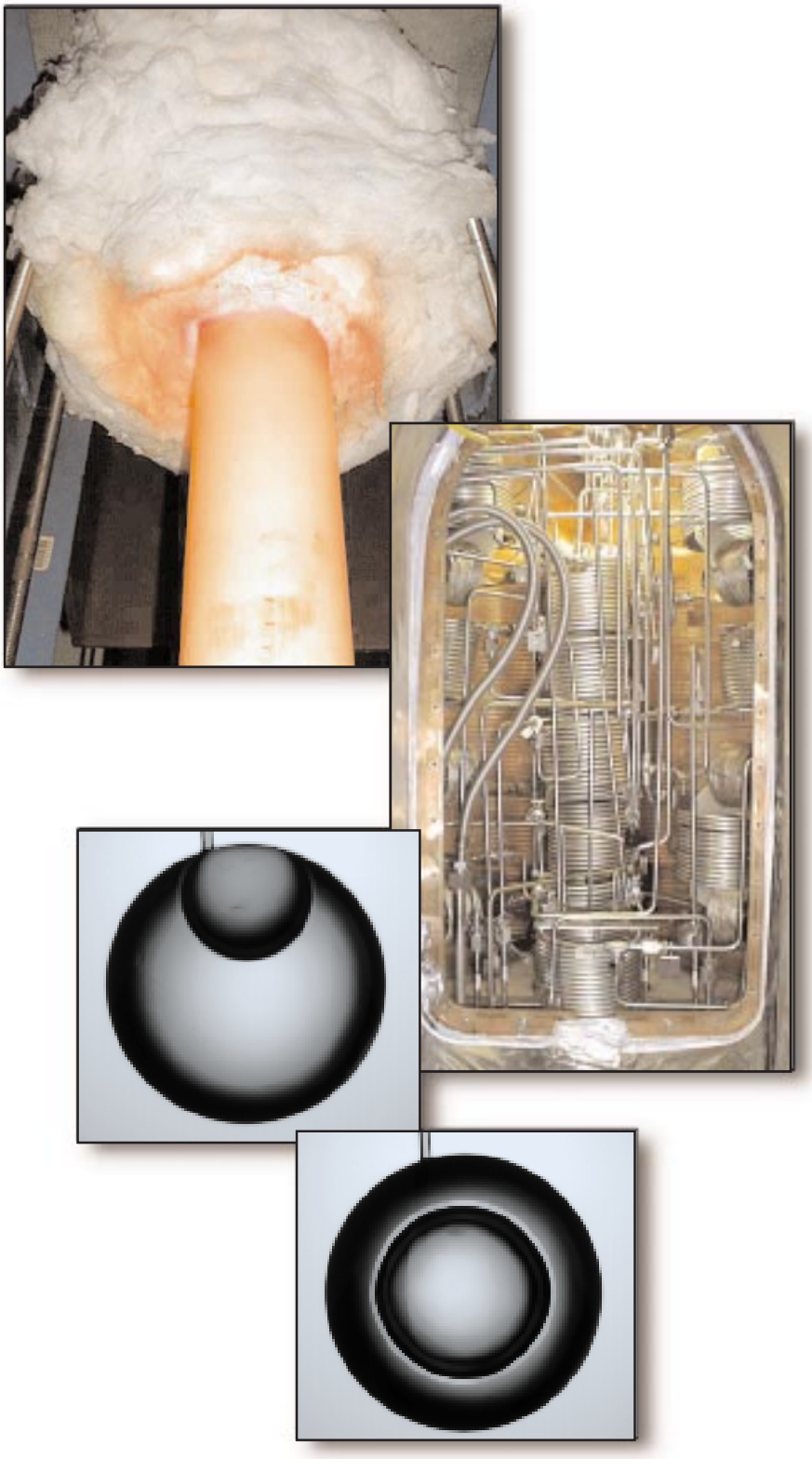

Inertial Confinement Fusion

ANNUAL REPORT

OCTOBER 1, 1997
THROUGH
SEPTEMBER 30, 1998

Schafer

GENERAL ATOMICS

GA–A22995
UC–712

INERTIAL CONFINEMENT FUSION TARGET COMPONENT FABRICATION AND TECHNOLOGY DEVELOPMENT SUPPORT

ANNUAL REPORT TO THE U.S. DEPARTMENT OF ENERGY

OCTOBER 1, 1997 THROUGH SEPTEMBER 30, 1998

by
PROJECT STAFF
Jane Gibson, Editor

Work prepared under
U.S. Department of Energy
Contract No. DE-AC03-95SF20732

GA PROJECT 03748
DECEMBER 1998

DISCLAIMER

THE FY98 TARGET FABRICATION AND TARGET TECHNOLOGY DEVELOPMENT TEAM

Dr. Kenneth Schultz
Program Manager

General Atomics
San Diego, California

Neil Alexander, Wes Baugh, Chuck Beal, Gottfried Besenbruch, Karl Boline, Lloyd Brown, Erwin Castillo, Sharon Considine, Don Czechowicz, Walt Egli, Fred Elsner, John Follin, Chuck Gibson, Jane Gibson, Kett Gifford, Dan Goodin, Steve Grant, Annette Greenwood, Eric Hoffman, Martin Hoppe, Dave Husband, Jim Kaae, Jim Kulchar, Barry McQuillan, Wayne Miller, Abbas Nikroo, Sally Paguio, Joe Pontelandolfo, John Ruppe, Chuck Schneidmuller, Clyde Shearer, John Sheliak, Joe Smith, Dave Steinman,Bob Stemke, Rich Stephens, John Vanderzanden, Don Wall, Jason Wall, David Woodhouse.

Schafer Corporation
Livermore, California

Tom Alberts, Thom Bahrs, Don Bittner, John Burmann, Frank Carey, Sue Carter, Derek Coker, Pat Collins, Steve Dropinski, Illges Faron, Scott Faulk, Chuck Hendricks, Ed Hsieh, Ephraim Hipolito, Earl Hodges, Derrick Mathews, Michael Monsler, Brian Motta, Craig Rivers, Jim Sater, Diana Schroen-Carey, Keith Shillito, Cheryl Spencer, Katie Strube, Tom Walsh, Kelly Youngblood.

ABSTRACT

On December 30, 1990, the U.S. Department of Energy entered into a contract with General Atomics (GA) to be the Inertial Confinement Fusion (ICF) Target Component Fabrication and Technology Development Support contractor. In September 1995, this contract ended and a second contract was issued for us to continue this ICF target support work. This report documents the technical activities of the period October 1, 1997 through September 30, 1998. During this period, GA and our partner Schafer Corporation were assigned 17 formal tasks in support of the ICF program and its five laboratories. A portion of the effort on these tasks included providing direct "On-site Support" at Lawrence Livermore National Laboratory (LLNL), Los Alamos National Laboratory (LANL), and Sandia National Laboratory Albuquerque (SNLA). We fabricated and delivered over 1200 hohlraum mandrels and numerous other micromachined components to LLNL, LANL, and SNLA. We produced more than 1300 glass and plastic target capsules for LLNL, LANL, SNLA, and the University of Rochester/Laboratory for Laser Energetics (UR/LLE). We also delivered nearly 2000 various target foils and films for Naval Research Lab (NRL) and UR/LLE in FY98. This report describes these target fabrication activities and the target fabrication and characterization development activities that made the deliveries possible.

During FY98, great progress was made by the GA/Schafer-UR/LLE-LANL team in the design, procurement, installation, and testing of the OMEGA Cryogenic Target System (OCTS) that will field cryogenic targets on OMEGA. The design phase was concluded for all components of the OCTS and all major components were procured and nearly all were fabricated. Many of the components were assembled and tested, and some have been shipped to UR/LLE.

The ICF program is anticipating experiments at the OMEGA laser and the National Ignition Facility (NIF) which will require targets containing cryogenic layered D_2 or deuterium-tritium (DT) fuel. We are part of the National Cryogenic Target Program and support experiments at LLNL and LANL to generate and characterize cryogenic layers for these targets. We also contributed cryogenic support and developed concepts for NIF cryogenic targets. This report summarizes and documents the technical progress made on these tasks.

TABLE OF CONTENTS

LIST OF TABLES

LIST OF FIGURES

1. TARGET FABRICATION PROGRAM OVERVIEW

On December 30, 1990, the U.S. Department of Energy entered into a contract with General Atomics (GA) to be the Inertial Confinement Fusion (ICF) Target Component Fabrication and Technology Development Support contractor. In September 1995, this contract ended and a second contract was issued to continue this ICF target support work. This report documents the technical activities of the period October 1, 1997 through September 30, 1998. GA was assisted by Schafer Corporation and we have carried out the ICF Target Fabrication tasks as a fully integrated team.

During FY98, the GA/Schafer team was assigned 17 formal tasks as shown in Table 1–1. These tasks are described briefly here (Section 1). Additional technical detail on selected topics is given in Sections 2 through 6 of this report.

TABLE 1–1
FY98 TARGET FABRICATION TASKS

Task No.	Task Title Description	Total $K	Task Leader
LL01	On-Site Support for LLNL	625	Miller
LL02	Micromachined Target Components	1,241	Kaae
LL03	Composite Polymer Capsules for LLNL	500	Miller
LL04	NIF Target Development and Support	500*	Sater/Alexander/Miller
LA01	On-Site Support for LANL	330	Miller
LA02	Composite Polymer Capsules	450	Miller
NR01	NRL Target Development and Deliveries	1,000	Hendricks
SL01	Target Components and Capsules for SNL	533	Kaae
SL02	Target Fabrication for SNL	577	Schroen-Carey
UR01	Target Production and Delivery for LLE	1,325	Miller
UR02	Capsule Development	125	Miller
UR03	Flat Foils	200	Hendricks
CR/LL1	Cryogenic Target Fielding Development	600	Sater
CR/LL2	Cryogenic Hohlraum Development for NIF	284	Alexander
CR/LA1	Beta Layering Support at LANL	209	Sheliak
CR/LA2	Design Support for LANL DT Fill Cryostat	20*	Goodin
CR/UR1	OMEGA Target Systems Engineering	2511	Besenbruch
	Total	$11,030	

*Additional support provided by the Lab.

1.1. LL01 — ON-SITE SUPPORT FOR LLNL

Our on-site team at Lawrence Livermore Laboratory (LLNL) was composed of Derek Coker, Derrick Mathews, Craig Rivers, and John Ruppe. They provided support in micromachining of target components, assembling target components into complete targets, and characterizing target components and capsules for use in NOVA and OMEGA ICF experiments.

1.2. LL02 — MICROMACHINED TARGET COMPONENTS

Under this task, we fabricated hohlraums, witness plates, and other target components. The hohlraums were fabricated by plating or coating various materials onto micromachined hohlraum mandrels. The mandrels are dissolved after delivery to the customer laboratory, leaving the empty shell to be assembled into a hohlraum. In FY98, this task was divided between LLNL and Los Alamos National Laboratory (LANL) although the major effort was directed toward production of components for LLNL.

- For LLNL the effort was to:
  1. Produce precision machined mandrels for use as coating substrates for hohlraum production.
  2. Produce precision machined target components.
  3. Provide supporting technologies such as electroplating, PVD, sub-component assembly, characterization and metrology.
  4. Supply production drawings and documentation.
- In FY98, we responded to 56 separate requests from LLNL for:
  1. 715 conventional gold-plated copper hohlraum mandrels.
  2. 134 thin-walled gold- and epoxy-coated copper hohlraum mandrels.
  3. 58 profiled plates (sine wave plates, flat plates, dimpled plates).
  4. 103 aluminum witness plates.
  5. 4 double gold-walled copper hohlraum mandrels.
- For LANL, the effort was to:
  1. Fabricate target components by micromachining.
  2. Supply characterization documentation.
- In FY98, we responded to 12 separate requests from LANL for:
  1. 189 conventional gold-plated copper hohlraum mandrels.
  2. 33 thin-walled gold and epoxy coated copper hohlraum mandrels
  3. 36 aluminum witness plates.

We responded to all of these requests promptly and produced components that met specification.

With the exception of the last month of FY98, the Precitech 2000 Lathe 1 (DOE-owned) and Lathe 2 (GA-owned) were operational over the FY98 period with only occasional down times of a few days. During the last month of FY98, these lathes experienced a series of operational failures that may be attributed to aging. As a result, each lathe was off line several times, each time for periods of several days to a week or more. By working to overcome these failures, we have become adept at repairing these lathes.

The Rocky Flats No. 3 Lathe operated with little down time. Because of its configuration, it is particularly useful for fabricating witness plates and other profiled plates, although it can also be used for machining hohlraum mandrels.

The new Precitech 2400 Lathe operated with virtually no down time this year. The 2400 Lathe maintains dimensional control better than the other lathes, probably because its slides are supported by high-pressure oil which does not vary in temperature during the day as much as the high-pressure air that supports the slides of the other lathes.

In FY99, we intend to purchase a high-accuracy milling machine to expand our machining capability. The upgrade of the air conditioning system that we intended to carry out in FY98 was postponed, primarily because the machining laboratory would have had to be shut down for an extended time for the modifications. We could not afford this loss of production time.

1.3. LL03/LA02/UR01/UR02 — COMPOSITE POLYMER CAPSULES

Flexibility, productivity, and rapid response continued to be guiding principles for the capsule delivery tasks. With the exception of the permeation barrier poly(vinylalcohol) (PVA) and glass shells, each layer was composed of glow discharge polymer (GDP). Target specifications required layer thicknesses ranging from 1 to 48 μm and dopants of deuterium, chlorine, germanium, titanium, or silicon, as shown by Fig. 1–1. Since about two-thirds of the requests were for multilayer targets containing up to four layers, flexibility in our production techniques was critical. Delivery schedules were irregular throughout the year since the ICF experiments requiring polymer capsules as targets occurred at irregular intervals. Usually, many different batches of capsules were required for an experiment and the target specifications were not known until three to four weeks before delivery. As a result, productivity and rapid response were essential to production. Overall, 92 batches for a total of 1062 targets were fabricated, characterized, and delivered. In addition, we delivered about 200 targets that did not require complete characterization and 40 “batches” of samples.

Although target production was by far our major activity, we made several improvements and discoveries. A major improvement was made to the GDP/poly(α-methylstyrene) (PAMS) process which is used to fabricate all the polymer capsules. At the beginning of the year, we had excellent control over the diameter, sphericity, and concentricity of PAMS shells. Unfortunately, nearly all shells had interior features that were found in the resulting GDP shells after pyrolysis. We found techniques to dramatically reduce the features and prepared over 25 batches acceptable for making target-quality GDP shells. Each batch has a tight diameter distribution, typically ±15 μm, so targets

will also have a tight distribution. The PAMS shell batches were made in a series that fully covers the range between 860 and 960 μm — the range needed for fabricating targets likely to be requested. In addition, we made considerable progress in developing techniques for making 2 mm PAMS shells for eventual use by the National Ignition Facility (NIF).

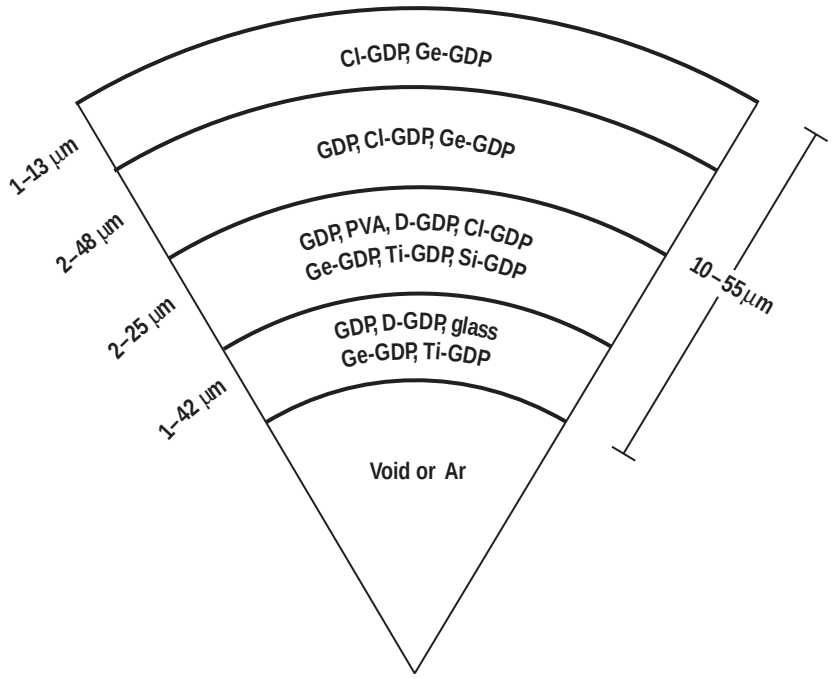

Fig. 1–1. Targets for ICF experiments may have several layers, each layer differing from the others by the type of dopant and the layer thickness. The layer thicknesses shown are the range of thicknesses that were requested, not the tolerances, e.g., a specific request for the third layer thickness could be 9 ± 1 μm. Only about one-third of the batches were for single layer targets.

Glass shells were about one-fifth of the targets delivered. The practical limit to the diameter of target-quality glass shells has been about 1200 μm. This year, we discovered two techniques that extend that limit by several hundred microns. In the first method, discovered by Abbas Nikroo, glass shells are permeation filled with a gas — typically helium or hydrogen. The filled glass shells are dropped down a heated vertical furnace; the glass softens and the shell expands from the pressure of the interior gas. In the second method, discovered by Martin Hoppe, a large fully pyrolyzed polymer shell is made by the GDP/PAMS method using GDP doped with a metal that, when oxidized, can form a glass or ceramic such as silicon, germanium, or titanium. Slowly heating in an oxygen-containing atmosphere turns the shell from polymer into glass or clear ceramic yet retaining excellent concentricity. Both methods require development to become reliable production techniques.

Additional improvements and developments include building a computer-controlled high pressure fill station, improved calibration for x-ray fluorescence (XRF) analyses, and characterizing the limits of atomic force microscopy (AFM) sphere mapping.

1.4. LL04 — TARGET DEVELOPMENT FOR NIF

This task was to provide additional support, above the level of effort that could be provided within our base program budget, to help LLNL in the development of targets for NIF. LLNL provided additional funds for this task.

1.4.1. MODELING AND SUPPORT

We provided support at LLNL to carry out Monte Carlo modeling studies of images produced by the shadowgraphy technique. This technique is used to form an image of an ice layer (DT, D_2 or HD) in a spherical plastic shell and is complicated by lensing effects of the shell and layer as well as by multiple reflections. Of particular interest, is the effect of bumps and dips in the layer on the intensity of the bright white ring that is typically associated with the layer surface. Support was also provided for thermally shimmed hohlraum development and construction and program development for a computer-based instrumentation system for the new cryogenic hohlraum test station at LLNL.

1.4.2. CRYOGENIC SUPPORT

A number of potential concepts for the NIF Cryogenic Target System, which fills targets with DT and cryogenically fields them in the NIF Target Chamber, were developed. They were discussed at the Tritium Filling Options Workshop held June 24, 1998, at GA. The four concepts are the temperature shimmed hohlraum for beryllium capsules, the in-hohlraum diffusion fill, the in-chamber cryogenic assembly, and the ex-chamber cryogenic assembly. The consensus of meeting attendees was that attention should be focused on a concept that fills multiple target assemblies in a fill cryostat, cold transports them to a transfer station cryostat, mounts an individual target assembly onto a target insertion cryostat, and layers and inserts the target using the target insertion cryostat. The target's DT fuel would be layered by temperature shimming the target's hohlraum. A work breakdown structure and schedule were started to aid with producing a cost estimate of this system.

The cryogenic target fielding option of using a cryogenic target that is assembled cryogenically in the NIF Target Chamber was examined for issues that would prohibit or render this option impractical. The two most serious issues found were alignment of the lasers to the target and building the miniature, high precision, cryogenic assembler. The laser beam alignment becomes problematic because the fully assembled target will only be available in fully assembled form for approximately 3 s before the shot. This is insufficient time to align the 192 beams and retract the Target Alignment System from the Target Chamber. The cryogenic assembler is a difficult project due to the required high precision, high force, low heating actuators that must be miniaturized to fit inside of the target insertion cryostat (TIC) shroud. A potential solution for the laser alignment issue was proposed. However, this solution may not be practical and would require expensive modifications to current NIF systems.

1.4.3. BERYLLIUM POLISHING

We completed our report, *Literature Review on Polishing, Polishing Techniques, and Sphere Polishing Equipment for Beryllium*. Of the polishing techniques described in the report, the one that has the highest probability of success in polishing beryllium spherical shells to NIF surface finish requirements, is relatively simple, and has fast removal rates is electromechanical polishing. This technique combines the best aspects of mechanical, chemical, and electrochemical polishing. Mechanical polishing can deform or work harden the surface of the beryllium due to the grinding action of the abrasive and this damaged zone can only be removed by chemical or electrochemical methods. The electromechanical polishing technique has been used successfully in producing metallographic samples and beryllium mirrors of the highest optical quality. The selection of the electromechanical polishing technique does not indicate the elimination of mechanical polishing or electrochemical polishing by themselves as possible techniques. Electromechanical polishing can be done using the basic design of the rotating plate machine. The design should be flexible enough to allow for either mechanical polishing or electrochemical polishing. The Los Alamos "Ring Lapping Machine" can easily be modified to an electromechanical polisher.

We completed the preliminary design for a device to polish NIF-sized beryllium shells and plan to fabricate the device early in FY99.

1.5. LA01 — ON-SITE SUPPORT FOR LANL

We provided two technicians to give on-site support for LANL under this task. At LLNL, Kett Gifford assembled and characterized numerous LANL targets. In addition, he provided some micromachining support to the target fabrication effort. At LANL, Steve Dropinski provided on-site support for target machining, assembly, and characterization of targets that were shot at NOVA, Trident, Z, and OMEGA. He also provided assistance during target campaigns at the University of Rochester/Laboratory for Laser Energetics (UR/LLE) when required.

1.6. NR01/UR03 — NIKE TARGET PRODUCTION AND OMEGA FLAT FILM DELIVERIES

The NR01 and UR03 tasks are, as in past years, closely related. The production of flat films for both the NIKE laser program and the Naval Research Laboratory (NRL) and the OMEGA laser program at UR/LLE utilizes many of the same techniques. However, there are also significant differences in film compositions and configurations as well as in the products delivered to the two Laboratories. Both programs require polymeric films which are flat and very smooth and films which are flat but have prescribed patterns on at least one of the surfaces. The patterns may be sinusoidal, step functions and in, some cases, are sinusoidal in two perpendicular directions. There are requirements for films which are 1.5 μm thick but which are composed of 20 interleaved layers: 10 layers of polyimide and 10 layers of gold. In Section 4 of this report, we discuss in more detail the varieties of targets produced and delivered and the techniques by which the targets are produced.

Several types of multilayered targets were produced. LLE targets include layered films of polystyrene and silicon-doped polystyrene — some with both surfaces smooth and some with applied perturbations such as sinusoids and orthogonal sinusoids. NRL targets include multilayer films, stepped aluminum layers, gold layers and metal layers which have various step functions imposed on their surfaces.

Because we deliver large area films to be made into many smaller target foils as well as discrete assembled targets, it is somewhat deceiving to count our target deliveries as a number of discrete items provided to the laboratories. The items delivered to LLE and NRL during FY98 add up to more than 1200. Some of these are films which are made into several hundred smaller target foils. Thus, the number of targets supplied approaches 2000 on the two tasks.

1.7. SL01 — CAPSULES AND COMPONENTS FOR SANDIA NATIONAL LABORATORY (SNL)

In FY98, this task was divided into two subtasks:

1. Micromachined Target Components
2. Capsule and Microshell Fabrication Development and Production

1.7.1. MICROMACHINED TARGET COMPONENTS

The micromachined target components subtask was devoted to fabrication of two types of components:

1. Thin-walled central cans
2. Shock breakout plates

The thin-walled central cans ranged in diameter from 2 to 10 mm and in lengths from 7 to 14 mm. All told, 210 of these central cans were fabricated, characterized, and delivered to SNL during FY98.

Most of the central cans produced in FY98 were copper. The technique that we have developed for fabricating these cans is to machine an acrylic mandrel with the internal dimensions of the can, then to sputter deposit a very thin copper layer on the can to supply conductivity for subsequent coating by electroplating, electroplate the specified can wall thickness on to the mandrel and, finally, remachine the mandrel to produce a flange and any specified holes. The cans are delivered to SNL on the mandrels because they are too fragile to survive shipping unsupported. The acrylic mandrels are removed at SNL by dissolution in acetone.

A substantial number of gold central cans were also produced in FY98. Copper mandrels are used for the gold cans; obviously, a sputtered conductive layer is not necessary; and the mandrel is dissolved in nitric acid. A typical central can is shown in Fig. 1–2.

We also produced glow-discharged-polymerized plastic cans by coating acrylic mandrels in a GDP coater of the type used to fabricate capsules.

Finally, in one case, we produced a set of silver central cans by sputter coating a silver conductive layer on to an acrylic mandrel and then electroplating the mandrel with silver.

For two particular sets of gold cans, a large number of holes were drilled along the length of the can as is shown in Fig. 1–3.

A total of 123 breakout plates (small, thin rectangular or circular plates either of uniform thickness or with a step-in thickness) were fabricated for SNL in FY98. Most of these plates were fabricated from aluminum but a few were fabricated from acrylic.

Fig. 1-2. A typical central can mandrel with a copper coating.

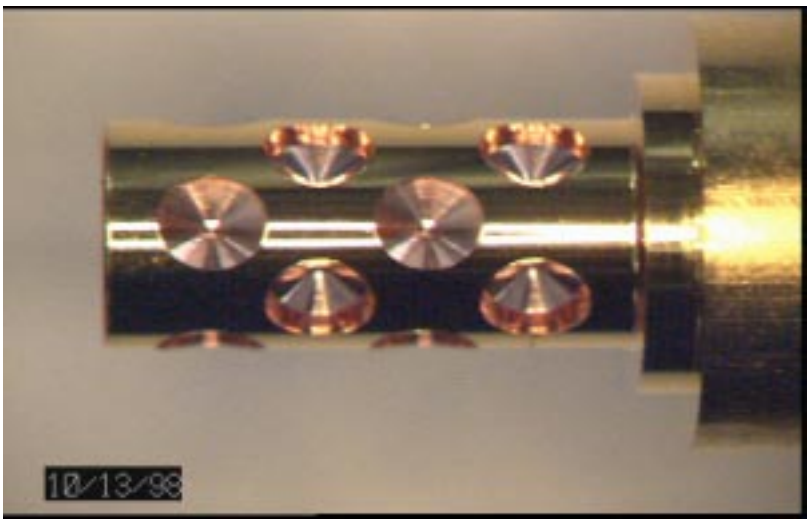

Fig. 1–3. A gold coated copper central can mandrel with holes drilled along the length of the can.

1.7.2. CAPSULE — FABRICATION DEVELOPMENT AND PRODUCTION

Five batches of capsules were shipped to SNL for experiments on Z. The first was a simple batch of PAMS shells. The remaining four batches for a total of eight composite polymer capsules required considerable development. The capsules have an inner diameter of 1650 μm and consist of a 30-μm inner layer of GDP or **Ge**-GDP and an outer layer of PVA and are filled with H_2 or D_2 and (except for one batch) SF_6.

A key problem was the permeation barrier. We had originally planned to use a thin (<5000Å) aluminum layer to permanently entrap the gas within the capsules. However, we found that thin aluminum coatings deposited on trial capsules did not adequately stop hydrogen or deuterium from leaking out. Though we suspected that capsule surface finish was the cause of the leakage, we had no time to investigate the matter further and instead chose to use the proven PVA coating process.

The shells were coated with PVA by dipping first one side in a PVA solution, drying the shell, then dipping and drying the other side. We later learned that some shells did not have sufficiently long gas fill half-lives. Thus, we applied a second layer of PVA over the first layer for most of the shells. We also found that the uniformity of the PVA coating was poor (a 2.5 μm average thickness PVA coating varied in thickness by ±1.0 μm). Adding to our difficulties, we found the PVA thickness uniformity was nonsymmetric. The time and budget constraints of this delivery required acceptance of this rather large error bar as a best effort. We will aim to improve PVA coating and characterization in FY99.

1.8. SL02 — FABRICATION OF TARGETS FOR SNL

In FY98, this task was divided into two subtasks:

1. On-site support at SNL
2. Fabrication and machining of low-density foams

On-site support was supplied by Tom Alberts who was assigned to SNL Albuquerque for the whole year. Tom led the effort in fabricating a variety of targets from components fabricated at GA and Schafer and other sources. This was a demanding task due to the increased number of targets and complexity of the target designs. His daily tasks were not limited to just assembly tasks but also the interfacing with experimenters and keeping detailed specifications of the load hardware. Tom Albert's efforts were recognized by SNL by presenting him with an "Award for Excellence" for his support of the dynamic hohlraum experiments that created temperatures >155 eV.

The foam subtask delivered 179 foam components in FY98. This represents a 380% increase from the previous year and 250% more than required by the task statement. This increase in quantity was accomplished by streamlining the production techniques and by improving the process for ordering foams. The ordering process became critical as the complexity of the components increased. Foam orders are now received by e–mail in AutoCAD format, subtleties of the requirements are discussed by telephone, and production is begun.

With the increase in quantity, we also achieved improvements in quality. The most requested foam in FY98 was made of TPX, the polymer produced from 4-methyl-1-pentene. The density range for this polymer was extended down to 3 mg/cc. For foams with a more routine density of 6 mg/cc, dimensional tolerances of less than 2% were routinely attained. Figure 1–4 shows an example of the foams that were produced. This foam is an annulus with a radius on one end and a 5-deg slope toward the center on the other.

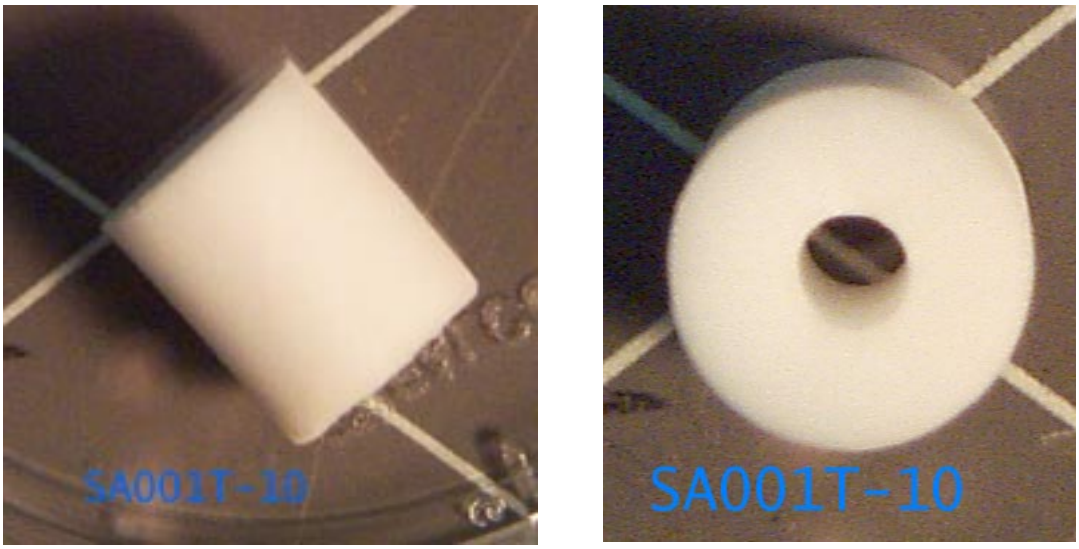

Fig. 1–4. Side and top views of a 6 mg/cc foam annuli with a radius on one end and a central slope on the other. The nominal dimensions of this foam are 9.0 mm height, 7.75 mm o.d., 2.25 mm i.d.

1.9. CR/LL1 — CRYOGENIC LAYERING DEVELOPMENT

High gain cryogenic targets for ICF are spherical shells which contain a layer of DT ice surrounding a volume of DT gas in thermal equilibrium with the solid. The roughness of the inner surface of the cryogenic fuel layer inside of these targets is one of the sources of imperfections which cause implosions to deviate from perfect one-dimensional performance. Reductions in the surface roughness of this fuel layer improve the ability of NIF to achieve ignition. We have worked closely with the cryogenic group at LLNL in developing smoothing techniques during the past year.

One technique, infrared (IR) heating, uses monochromatic infrared radiation to selectively excite rotational-vibrational bands of specific molecular hydrogen isotopes (HD in recent experiments). This technique causes volumetric heating of the ice layer and is an analog of the ß layering smoothing technique. The amount of IR heating in the bulk ice layer is controllable. IR heating is the only known solid layering technique for nontritiated hydrogen. With this technique, D_2 ice layers in 1 mm o.d. plastic capsules have been generated with layers as smooth as 1.6 µm rms. The geometry in which we carry out experiments has been purposely chosen to closely adhere to University of Rochester design constraints for the cold transfer cryostat.

A major part of effort over the past year has been adapting key pieces of the IR layering apparatus for use in the OMEGA Cryogenic Target System (OCTS). We have successfully designed and tested a simple and reliable optical fiber parting joint for transmitting the IR radiation into the removable shroud of the OCTS. We have suggested modifications to the layering shroud to make it more amenable to IR layering. These modifications included a smaller window to increase the efficiency of the layering shroud/integrating sphere and a different cut plane in the shroud to allow for easier coating of the interior with a diffuse gold coating. We have also identified and tested commercial components for the layering system.

The point target design for the NIF calls for a gas density of 0.3 mg/cc in the center of the cryogenic target. This is equivalent to the saturated vapor pressure over an 18K DT solid. Since DT's triple point is at 19.79 K, the effects of cooling smooth layers to 18 K have been investigated. We have observed that both D_2 and DT layers become dramatically rougher in spherical geometries. This contrasts with the results obtained at LANL by Jim Hoffer and John Sheliak. The LANL experiments are carried out in a cylindrical sample allowing direct observation of the layer surface. They find that layers become smoother with temperature cycling. This discrepancy is not understood but may be geometry related. We are currently working on methods to cool a smooth layer to 18 K without destroying the surface finish.

Technical support has been provided for NIF layering and cryogenic efforts. This has included providing 1 mm shells with 20 to 30 μm o.d. fill tubes for use at LLNL as well as at LANL.

1.10. CR/LL2 — CRYOGENIC HOHLRAUM DEVELOPMENT FOR NIF

A design for a cryogenically assembled hohlraum (CAH) target for NIF was developed. In this concept, the capsule is film mounted in a ring. The ring is mounted to the TIC, inside of a spherical layering cavity in the TIC's shroud. The hohlraum assembly mechanism is located in the shroud. After the DT in the capsule has been layered and the TIC inserted into the NIF Target Chamber, the cryogenic assembler actuates to fasten the hohlraum halves to the capsule's mounting ring and, hence, forming the complete target. The TIC's shroud is then immediately removed and the target is shot.

For this design to work, the perturbation to the layering cavity's spherical isotherms caused by the capsule's mounting ring must be small enough to permit the beta-layering of the DT fuel layer to produce a sufficiently uniform layer. The total mass of the target should be less than 1 g. The CAH design we developed has a mass of 0.5 g. Thermal analysis of the capsule and mounting ring in the layering cavity was conducted. The CAH design predicts a DT fuel layer nonuniformity of less than 0.2%.

A number of concepts were developed for the seals that are needed to join together the CAH target hohlraum. These seals must hold the tamping gas inside of the hohlraum once it is assembled. Experimental tests were carried out on two types of seals at both room temperature and cryogenic temperature. The results of the seal testing ranged widely, even for tests of nominally identical samples. At present, the reason for the variation is not clear. There were cases where the leak rate was

small enough that would likely be acceptable for the CAH target. In the best case, a seal pressed together with an assembly force of 980 N had a leak rate of 7×10^{-10} STD mbar l/s (helium) when pressurized to 690 kPa and the assembly force was released to zero. On the high side, other samples have had leak rates as high as 11 STD mbar l/s (helium).

A conceptual design for a cryostat for the D_2 Test System was produced. The cryostat is to be used to house a permeation cell and cryogenic manipulator for full-scale NIF cryogenic target assemblies. The system is to be used to fill targets to full density with deuterium in the permeation cell, to remove targets from the cell to where they can be observed and layered (including enhanced IR layering), and to test key components and interfaces for the NIF Cryogenic Target System. Tests would include the attachment of a tamping gas fill tube line to the hohlraum through its base, manipulating target assemblies out of the permeation cell, and attaching them to Target Insertion Cryostats.

1.11. CR/LA1 — BETA LAYERING SUPPORT AT LANL

Beta-layering work by John Sheliak at LANL during FY98 included the continuation and completion of DT solid layering experiments inside a 2-mm diameter beryllium torus in which the ratio of tritium/deuterium was progressively reduced for each successive experiment. Work also included the completion of a preliminary design of the data acquisition and motion control systems for the cryogenic pressure loader (CPL) optical, target insertion, and layering sphere apparatus.

The DT solid layering work consisted of experiments in which the fraction of tritium in the DT mixture [f = T/(T + D)] was varied from 98.5% down to 3.9%. This was done by progressively removing a portion of the old DT mixture and diluting the remaining mixture with additional D_2. RMS surface roughness (σ_{rms}) was then measured as a function of tritium fraction, for each dilution. The experiments performed this year were a continuation of tritium fraction experiments begun during the last quarter of FY97 [Project Staff, "Inertial Confinement Fusion Target Component Fabrication and Technology Development Support, Annual Report to the U.S. Department of Energy, October 1, 1996 through September 30, 1997," General Atomics Report GA–A22816 (1997) p. 5–15]. Results show that (σ_{rms}) is weakly dependent on tritium fraction down to about 30% T (average σ_{rms} = 1.45 mm), after which the surface roughens progressively to 4.1 mm at 3.9% T. The overall data set exhibits a very close fit to a hyperbolic function with asymptotes at σ_{rms} = 1.34 mm, and T/(T+D) at 0. These results demonstrate that beta-layering can produce reasonably smooth DT surfaces even at low tritium fractions.

The CPL apparatus consists of a cryostat with integrated permeation cell, layering sphere, and target insertion mechanism. The CPL apparatus also includes an optical system external to the cryostat, which functions as an image acquisition and monitor for the target, once it has been filled in the permeation cell and lowered to the DT layering sphere position. This apparatus will be used to test DT target filling and solid layering operations, as well as measuring the amount of DT release from the target filling permeation cell to the cryostat volume. This testing is being done to provide process and operational data relevant to DT operations with the OMEGA (UR/LLE) Cryogenic Target

System. The apparatus will also demonstrate the ability to produce β-layered targets as well as perform optical target characterization.

The CPL control system will control target insertion and layering sphere positioning mechanisms as well as the x-y-z stage positioning mechanisms for the image acquisition and real-time monitoring cameras and optics. The image acquisition and monitoring systems will acquire and save images of the solid layering process as well as provide on-going monitoring of the process in real-time. The preliminary design of the control, acquisition, and monitoring systems has been completed with all components either on order or in-house ready for assembly and testing. Control, data acquisition, and monitoring functions will all be performed in the LabView integrated software environment.

1.12. CR/LA2 — CRYO DESIGN SUPPORT

LANL has designed and is currently assembling the CPL to investigate tritium aspects of direct drive targets at cryogenic temperatures. Specifically, the CPL is designed to demonstrate the beta layering of permeation filled OMEGA targets. In addition, this cryostat will be used to examine tritium migration issues and to establish procedures for tritium containment for the OCTS at UR/LLE.

GA provided engineering support during the design phase of the CPL program under "extra" funding provided by LANL. This support consisted primarily of reviewing LANL's cryostat design and included participation in the CPL Preliminary Design Review. GA also took an active role in the design of the CPL manipulator, based on our experience with vacuum manipulators on the OMEGA system. The manipulator design was constrained by the limited height of the glove box and by the desire to use standard commercial products. The manipulator has been fabricated by Thermionics N.W. and delivered to LANL.

1.13. CR/UR1 — OMEGA CRYOGENIC TARGET SYSTEM ENGINEERING

During the past year, the team of UR/LLE, LANL, GA, and Schafer made great progress in the design, procurement, installation, and testing of the OCTS. The following major achievements occurred in FY98:

1. The design phase was concluded for all components of the OCTS.
2. All major components were procured and nearly all were fabricated.
3. The majority of the fill/transfer station (FTS) and associated components were assembled, tested and shipped to UR/LLE.
4. Significant portions of the moving cryostat (MC) and moving cryostat transport cart (MCTC) were assembled and tested.
5. The Upper Pylon housing and vacuum feedthrough were installed at the GA test facility.

Remaining tasks include: (1) delivery of the FTS to UR/LLE; (2) delivery and assembly of the MC thermal shrouds; (3) final assembly of the MC and the MCTC; (4) delivery of the Shroud Puller linear motor, lower pylon, and chain locker; and (5) assembly and testing of the target insertion and shroud pulling process in a simulated target chamber environment. These tasks are scheduled for completion in the third quarter of FY99 with shipment to UR/LLE in June 1999.

The year was not without its challenges, however. Recognizing early on that some of the components were complex and would require significant delivery times, we ordered long delivery items, like the FTS cryostat and Shroud Puller motor, early in the design phase. We also developed surrogates simulating the actual geometry of the host system to carry out installation and mechanical checkout of components. However, most of the difficulties were still associated with the inability of vendors to supply and fabricate components on schedule. This resulted in technical compromises to maintain the overall schedule of shooting cryotargets in early FY00. For example, the FTS cryostat is being shipped directly to UR/LLE from the vendor without prior assembly and testing at GA. Therefore, no cryogenic testing of the FTS was possible prior to shipment of the FTS-related components to UR/LLE. This testing will be carried out at UR/LLE in FY99 with GA support.

2. CAPSULE DEVELOPMENT AND PRODUCTION

A major element of the ICF target fabrication activity is development of new techniques for producing improved targets for future deliveries. Some of these activities are described here.

2.1. CAPSULE DEVELOPMENT

We made substantial progress in improving the quality and size range of our shells. We have developed techniques for making large and thin-walled poly(α-methylstyrene) (PAMS) shells and identified two potential sources of interior deposits, increased diameters of glass and polymer shells by using a re-blowing technique, and developed a novel way to make titania and glass shells.

2.1.1. POLY(α-METHYLSTYRENE) (PAMS) MANDRELS — PROCESS CONTROL

Following upon the PAMS shell work developed in FY97, one major task in the first seven months of this year was control of interior deposits in PAMS shells. (Other shell specifications, such as outside diameter, wall thickness, out-of-round (OOR), and nonconcentricity, have remained controlled within desired specifications.)

Interior Deposits. The interior deposit problem bedeviled us. For several months, we pursued the possibility that poly(vinylalcohol) (PVA) in the exterior water was somehow getting inside the shell to form the deposits. We had previously found $CaCl_2$ in the exterior water had migrated from the exterior to the interior, and we had replaced the $CaCl_2$ with ammonium chloride. However, after diverse lab efforts to identify the deposits, infrared spectroscopy failed to see any PVA on the inside. This data forced us to look elsewhere for sources of deposits. Ultimately, we identified two potential sources:

- The fluorobenzene used for the O1 phase had a deeply colored nonvolatile impurity. Distillation purified the fluorobenzene. We now routinely distill the fluorobenzene.
- The O1 phase is routinely filtered at 0.2 μm with a syringe filter. We found that the PVDF filter (Gelman) had a wetting agent whereas the PTFE filter does not have a wetting agent. We now use only PTFE filters.

Once we made these two process changes (distilled fluorobenzene and PTFE filters), the interior deposits were reduced, with many batches "free" of deposits. There still remains at least one minor source of deposits, which we think may be in the starting polymer.

Control of o.d. and OOR. In the previous fiscal year, we improved o.d. control by use of a strobe. OOR was controlled to below 1 μm by controlling the bath curing temperature to obtain a density match. In this fiscal year, those shell specifications were maintained by these process parameters.

After we had significantly reduced interior deposits, we prepared an inventory of PAMS shells at every 10 μm from 860 to 960 μm diameter. This inventory was required to meet new target specifications for the University of Rochester/Laboratory for Laser Energetics (UR/LLE) experiments. We were able to complete this task while maintaining all other shell specifications.

Large PAMS Mandrels. A major effort was carried out during FY98 on development of large PAMS mandrels. This work involved both development of approximate 2 mm diameter PAMS shells and PAMS beads. Initial scoping studies to increase the size of 1 mm shells to 2 mm by using an extension of 1 mm shell processing conditions were unsuccessful. At first, it was necessary to utilize quite different processing conditions to fabricate quantities of large 2 mm shells and beads. These conditions included use of a density mismatch between shell/bead preforms and the external water phase during the curing process, keeping shell/bead preforms out of the path of impeller blades during stirring, and the use of higher oil concentrations for the preforms. Using this approach, quantities of large ~2 mm shells were fabricated having batch average OOR from 10 to 50 μm ($rad_{max} - rad_{min}$).

Later work began to make use of density matching conditions during the shell/bead curing process. Density matching greatly improved OOR for large shells and beads. Shells and beads produced using density matching conditions were fabricated having 1 to 3 μm OOR. However, size control was difficult particularly for the fragile shell preforms and final shells. Conditions which should have produced 2.0 mm diam shells were producing 1.7 to 1.9 mm shells. The size decrease was from slicing of shell preforms that were intimately in contact with impeller stir blades during the density matched curing process. Below are two power spectra for a ~2.0 mm PAMS shell and a ~2.0 mm PAMS bead produced using density matching conditions (Figs. 2–1 and 2–2).

1.7 mm Beads for Sandia National Laboratory (SNL). After success was observed during fabrication of highly spherical ~2 mm PAMS mandrels, requests came from SNL to produce 1.7 mm PAMS mandrels on a “best effort” basis for use in fabricating capsules for experiments on Z by the decomposable mandrel technique. Since size control was a problem for large shells, it was decided to fabricate 1.7 mm beads to satisfy the SNL request. During the fabrication campaign to produce these beads, 15 to 20 batches of 1600 to 1800 μm diameter beads were produced. The average OOR for the bead batches was typically ≤1 μm. The resulting glow discharge polymer (GDP) shells had similar OOR.

There is considerable time savings in the fabrication of beads relative to shells. When beads are used as mandrels in the PAMS/GDP process, one does not have to extract water from the beads. The initial work to fabricate the SNL capsules showed that beads could be used to produce very spherical capsules. Future efforts may determine if there are advantages in the use of beads with regard to final capsule quality.

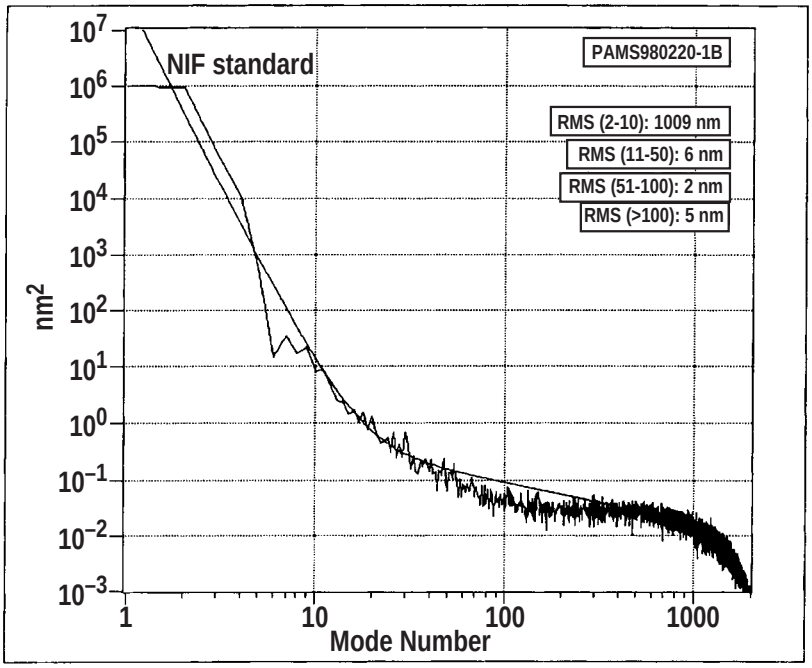

Fig. 2–1. Power spectrum of a ~2 mm PAMS shell.

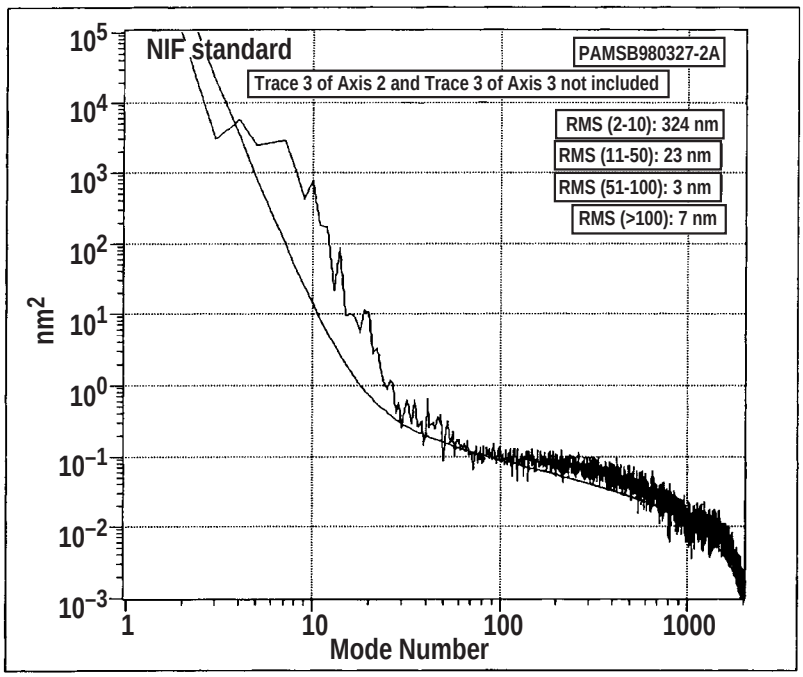

Fig. 2–2. Power spectrum of ~2 mm PAMS bead.

Large Mandrel Curing Monitored by Diameter Measurement. During work on processing of large PAMS mandrels, a technique was developed to monitor the curing process by way of shell/bead preform diameter measurements. The information obtained from the diameter measurements could be used to yield oil (polymer) concentration and solvent loss rate for the preforms. The technique made use of careful on-the-fly measurement of shell/bead diameters through the typical 3 to 8 h curing process. This study showed that many parameters influence the curing process; among them, bath temperature, polymer (solvent) concentration, solvent layer thickness, preform surface/volume, total amount of solvent, mixing and transport in water-2 phase, and water-2 surface area. The data on polymer concentration versus time and the solvent loss rate can allow one to modify conditions in the mixing of shells/beads to accommodate changing shell/bead properties and produce highly spherical mandrels.

Extended Cure Studies for Large Shells. Through the use of extended cure times (12 to 48 h) and gentle agitation, we recently produced 1800 to 1900 μm diameter PAMS shells with 8 μm wall thickness, having an average OOR of 0.5 μm. Large shells and beads typically have used a 3 to 8 h curing scheme. It is believed that the extended cure time along with thinner shell walls may be beneficial in producing highly spherical mandrels. These recent results for large shells are very encouraging and more extensive studies are planned in FY99.

Thin-Walled Capsules. We have developed a good understanding of the reference process parameters for the production of Omega sized (~950 μm o.d.) capsules with a wall thickness of ~18 μm. In the production of these reference shells, an 11% solution of 400K MW PAMS dissolved in fluorobenzene is used. LLE asked us to produce some thin wall PAMS shells, from both 400K and 100K MW PAMS. We anticipated increased shell breakage both during curing and during the ethanol extraction of the interior water with sonication due to the greatly reduced strength of the fully cured shells.

To produce thin-walled shells, we examined two options:

1. Reduce the ratio of O1/W1 in the wet shell to below 1.00, and thus thin the 11% PAMS O1 layer.
2. Keep the O1/W1 ratio near 1.00, but reduce the O1 concentration below 11%.

For 11% 400K PAMS O1 (Option A), reducing the ratio O1/W1 resulted in egg-shaped shells with poor OOR (Table 2–1).

TABLE 2–1
THIN-WALLED PAMS SHELL PRODUCTION — OPTION A

O1/W1 Ratio	1.00	0.45	0.33
Nominal Wall Thickness	18 μm	8 μm	6 μm
4π OOR ($rad_{max} - rad_{min}$)	<1 μm	4 to 14 μm	15 μm

The poor OOR led us to abandon this approach.

For runs near a O1/W1 ratio of 1.00, and decreasing the 400K O1 concentration (Option B), we obtained better OOR, but at the expense of a much poorer yield of shells (Table 2–2).

TABLE 2–2
THIN-WALLED PAMS SHELL PRODUCTION — OPTION B

400K, O1 Concentration	11%	7.9%		5%	
Nominal Wall Thickness	18 μm	8 μm	6 μm	8 μm	6 μm
4π OOR ($rad_{max} - rad_{min}$)	<1.0 μm	2.3 μm	2.1 μm	0.9 μm	0.8 μm

The yield of shells in the reference process is typically 95% to 99% in both the curing step and in the extraction/sonication step. For thin-walled shells, the yield coming out of the curing step is about 10%, and the yield out of extraction/curing is 10% to 40% for an overall range of 1% to 4% of all shells made. An additional minor effect is the greater shrinkage of the cured shells. In the reference process, the shells shrink some 20 to 40 μm. For these thin shells, the shrinkage was more typically 70 μm, so the shells resulted in 910 to 930 μm o.d. rather than 950 to 970 μm. Deliveries were made from these batches of 400 K material.

For shells made from 100 K PAMS, we continued with the option of more dilute O1 to make shells. The yield of shells decreased even further (Table 2–3).

TABLE 2–3
THIN-WALLED PAMS SHELL PRODUCTION — EXPERIMENTAL RESULTS

100K, O1 Concentration	8%	6.5%	5%
Nominal Wall Thickness	8.6 μm	10.6 μm	8 μm
4π OOR ($rad_{max} - rad_{min}$)	0.8 to 1.0 μm	0.7 μm	0.7 μm
Yield of final shells	3.8%	0.1% to 0.5%	0% to 0.1%

This thin-walled shell work is continuing into the next fiscal year.

Ethanol Extraction/Sonication. The cured shells are filled with water which must be extracted through the shell wall. Until a bubble nucleates, the extraction leads to a mechanical stress on the shell wall which can dimple or crack the shell. In the reference process, we induce the bubble nucleation by putting the shells in a standard (40 kHz) laboratory sonication bath. We knew that the standard sonication bath would stress and crack these thin-walled shells. We obtained a 104 kHz microsonication bath and a 170 kHz microsonication bath, which are purported to be gentler for washing purposes. The bulk of the work has been done with the 104 kHz bath. We monitored when the shells nucleated as a function of time extracted and the concentration of ethanol. Typically, we

saw bubble nucleation after 3 to 7 h in 25% ethanol and a resulting yield of 10% to 40% final floaters. The extraction data is somewhat variable, possibly due to the varying amount of gas dissolved in the 25% solution. (Air seems to be supersaturated in the 25% solution, but a varying amount comes out during the extraction before the first sonication.) However, the gentler sonication did permit us to obtain nucleated and crack-free shells.

For further information, contact Dr. B. McQuillan, D. Czechowicz, or F. Elsner (GA).

2.1.2. INCREASING SHELL DIAMETER BY REBLOWING

We developed a technique that enables us to produce good quality glass shells up to 2 mm in diameter. Smaller (less than 1500 μm diameter) glass shells made using the traditional drop tower technique are first filled with helium. They are then redropped through a short tower which has an approximately 1-ft long hot zone heated to 950°C. The glass shells soften at that temperature and the increased internal gas pressure blows the shells larger (Fig. 2–3). Because the heated zone is short, the enlarged glass shell exits the hot zone and freezes before helium can permeate out. We have also used the same concept to enlarge plastic shells. We used both GDP shells made by the depolymerizable mandrel technique and PAMS shells. Enlargement of the plastic shells is done at much lower temperatures (~200°C) and air is used as the fill gas.

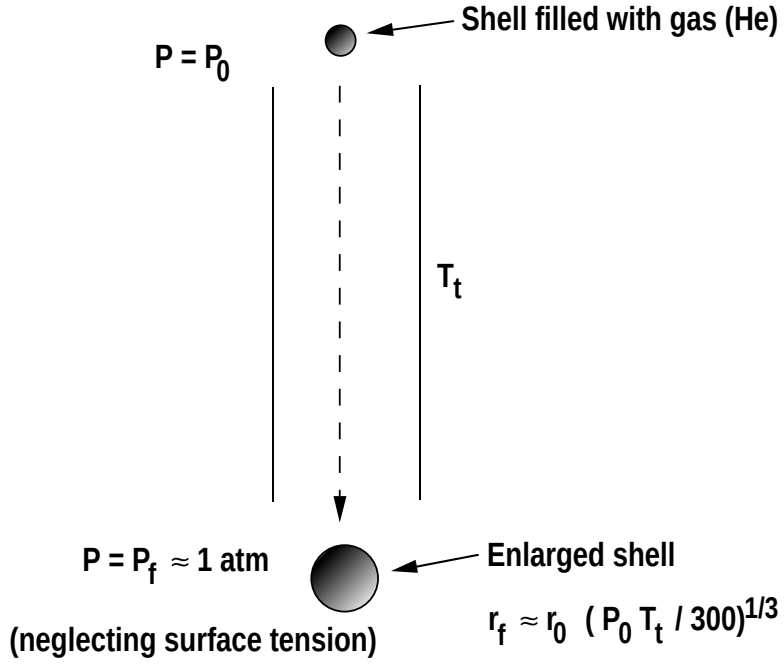

Fig. 2–3. Schematic of the reblowing technique. Gas-filled shells expand when they soften as they fall down a short heated tower. If surface tension is neglected, the initial radius should expand by the cube root of the fill pressure when expressed in atmospheres.

A short (~1 ft) tower heated to 950°C was needed to obtain the desired results. Figure 2–4 shows optical and interferometric images of shells expanded to over 1700 and 2000 μm. The starting shells were about 1200 μm in diameter. The outward pressure of the gas as the shells expand appears to smooth out any wrinkling in the shells. The smooth interferometric image in Fig. 2–4(b) is a good indicator of this effect. To investigate this further, we used this technique on shells that had severe dents. The re-blowing process actually removed the dents from the shells.

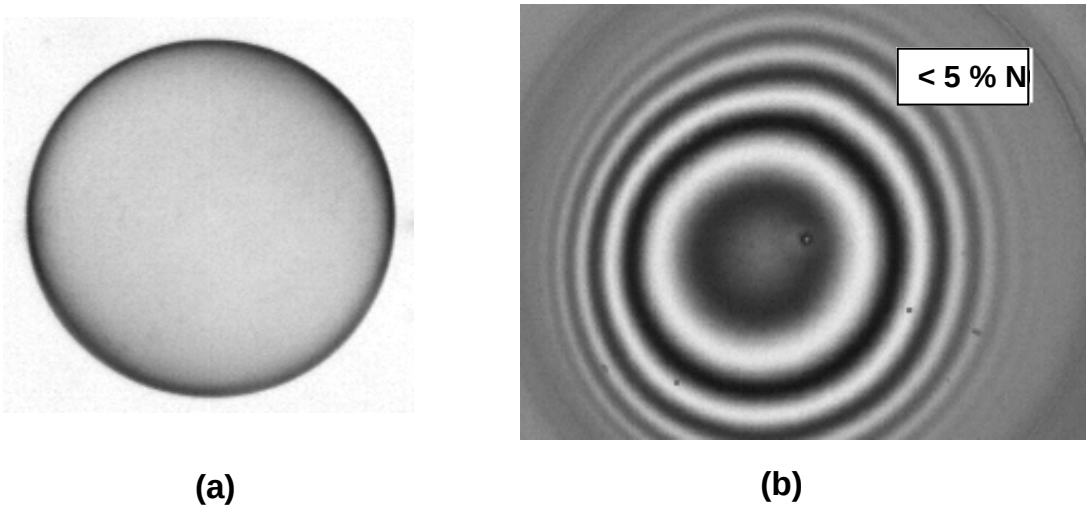

Fig. 2–4. Images of enlarged glass shells. (a) Transmission microscope image of a 1740 μm glass shell expanded from a 1200 μm starting mandrel. Note the absence of any wrinkles or dents. (b) Interferometric image of a 2002 μm glass shell made from a ~1300 μm starting mandrel. The smooth fringe pattern indicates absence of wrinkling or major wall thickness variations in the shell. The wall thickness nonconcentricity is less than 5%.

For further information, please contact Dr. A. Nikroo (GA).

2.1.3. FABRICATION OF GLASS AND TITANIA SHELLS BY PYROLYSIS OF DOPED GDP

We have developed a new pyrolysis technique for fabricating glass and titania shells. The first shells made by using this technique were composed of TiO_2. The precursors for these shells were prepared from titanium-doped glow discharge polymer (**Ti**-GDP) utilizing trans-2-butene and titanium tetrachloride deposited onto ~1 mm PAMS mandrels. The **Ti**-GDP layer deposited onto the PAMS mandrel was ~6 μm thick and contained about 5 at.% titanium as measured by x-ray fluorescence (XRF).

Immediately after deposition of the **Ti**-GDP was complete, the coated shells were put into a tube furnace for pyrolysis in a nitrogen atmosphere. Prior to this pyrolysis step, exposure to air was kept to a minimum because the **Ti**-GDP is air sensitive and decomposes, resulting in poor coating quality after pyrolysis. The shells were pyrolyzed according to the following schedule: (1) room temperature to 265°C at 10 deg per minute; (2) then ramp-up to 290°C at 1 deg per minute; (3) hold for 10 h; (4) cool to room temperature. This pyrolysis step removes the inner PAMS mandrel and significantly

stabilizes the **Ti**-GDP layer with respect to exposure to air. After pyrolysis the titanium concentration was measured to be ~4.8% by XRF.

In order to convert the **Ti**-GDP preforms into TiO_2 mandrels, the preforms were put into a platinum boat and then pyrolyzed in air as follows: (1) room temperature to 280°C at 10 deg/min; (2) hold for 30 min at 280°C; (3) ramp to 500°C at 1 deg/min; (4) hold for 6 min; (5) ramp to 800°C at 10 deg/min; (6) hold for 60 min; (7) cool to room temperature. This process resulted in the formation of the uniform-walled, transparent shells shown in Fig. 2–5.

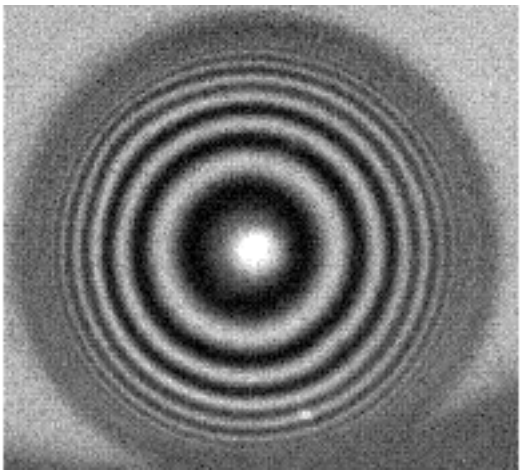

Fig. 2–5. A TiO_2 shell resulting from the pyrolysis of **Ti**-GDP. The interferometric fringe pattern demonstrates the transparency and wall uniformity of the shell.

Energy dispersive XRF analysis, along with x-ray diffraction analysis of the shells confirmed that these shells are essentially pure TiO_2 in rutile form. These TiO_2 shells also prove to be mechanically stronger than equivalent glass shells; a 510 μm o.d. × 2.5 μm wall shell survived a 1100 psia buckle test with helium.

These shells were shown to be impermeable to argon at 140°C and helium at 380°C. This was confirmed by subjecting the shells to an overnight 1 atm argon fill at 140°C and using our XRF system to verify the absence of argon in the shell. Likewise, the shells were subjected to an 18 h 50 atm helium fill at 380°C. No helium permeated into the shell as measured by interferometry. This was confirmed by breaking the shell under glycerin (Fig. 2–6). The shell breaking test showed that the pressure inside the shell was less than one atmosphere (the air bubble was significantly smaller than the inner diameter of the shell) indicating that essentially no helium had permeated into the shell.

In addition to making TiO_2 shells from **Ti**-GDP, we made SiO_2 shells from **Si**-GDP (Fig. 2–7) demonstrating that this process is not unique to **Ti**-GDP. This process has yet to be optimized or fully explored.

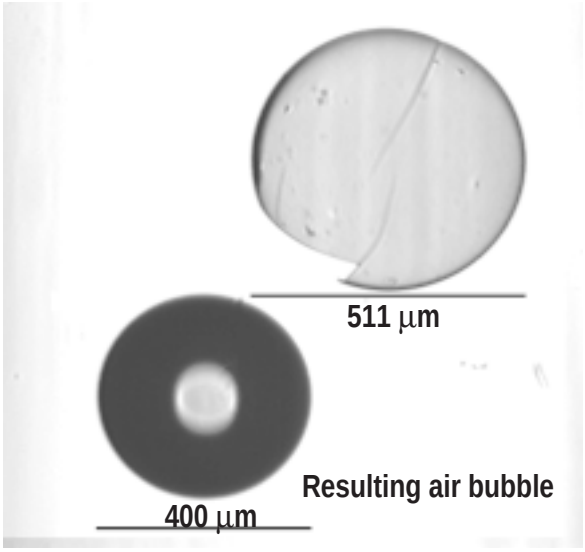

Fig. 2–6. The resulting air bubble was smaller than the inner diameter of the shell, confirming that the shell was not permeable to helium under the conditions tested.

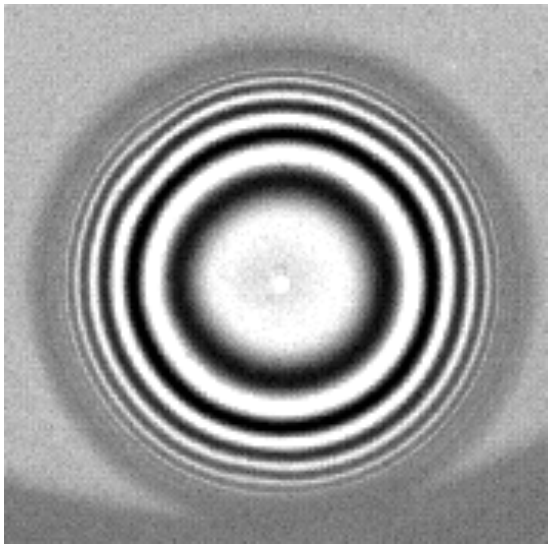

Fig. 2–7. An SiO_2 shell resulting from the pyrolysis of **Si**-GDP confirms that this process is not unique to **Ti**-GDP.

For further information, please contact Dr. M. Hoppe (GA).

2.2. CAPSULE GAS FILLING AND PERMEATION BARRIER IMPROVEMENTS

2.2.1. COMPUTER-CONTROLLED HIGH-PRESSURE FILL STATION

In order to improve our ability to meet our customers' requirement to burst test and/or reliably fill target capsules with helium, hydrogen, or deuterium to precise pressures, a new fill station was designed and built. Our original station (still operational) was designed to enable very high pressure fills (≥10,000 psi) but requires frequent operator attention and is not as precise for low to medium pressure fills. The design of the new station incorporates a computer, a computer-controlled pressure regulator, and cryo-intensifier for fill/burst pressures up to 6000 psi. In conjunction with the computer control, the minimal internal volume of the new fill station and the improved design of the permeation cell allow for very little operator attention once the fill is in progress. The central part of the new fill station is shown in Fig. 2–8.

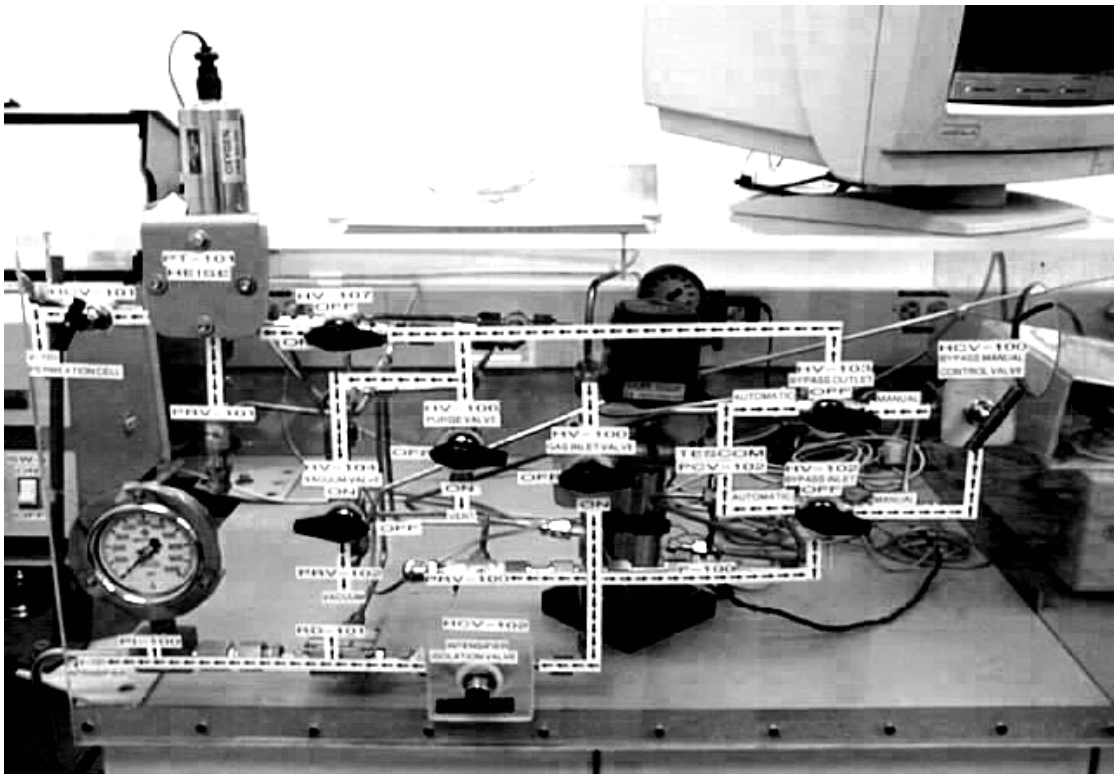

Fig. 2–8. The central portion of the new fill station with computer-controlled pressure regulator.

For further information, please contact S. Grant or Dr. M. Hoppe (GA).

2.2.2. PERMEATION BARRIERS

Glass. Several target designs for the National Ignition Facility (NIF) involve plastic mandrels [2–1] made by the GDP/PAMS technique [2–2]. Because the permeation rate of D_2 through a GDP shell is very fast (half-life of less than 1 h), these targets require a permeation barrier if room

temperature handling or experiments are required. PVA has been used successfully as the permeation barrier for Nova shells for many years [2–3]. However, the drop tower PVA coating process has a very low yield (~3%) and the final coating thickness is nonuniform, leading to undesired wall thickness variations around the shell [2–4]. Therefore, an alternative to this technique is highly desirable.

Glass has ideal permeation characteristics for D_2. D_2 can be permeated through a thin glass shell at elevated temperatures (~360°C) in a few days and will be trapped inside the glass shell at room temperature for months. Therefore, we explored providing GDP shells with an alternative permeation barrier by sputter-coating them with glass. The presence of thick glass layers (>1 μm) in ignition targets has been traditionally undesirable, although a current design does incorporate rather thick glass layers [2–5]. Therefore, we pursued determining the thinnest possible coating that would retain its integrity and provide good permeation characteristics against D_2. We initially determined helium permeation rates and also explored the possibility of permeating argon into the glass-coated shells as well.

GDP shells, ~900 μm in diameter and 10 to 20 μm thick, were used as the starting mandrels. Sputtering was performed in a Temescal sputtering system. All sputtering runs were done at 500 W at 13.6 MHz. The system pressure was varied to obtain the densest coatings as described below. 99.95% pure quartz discs were used as the sputtering targets. A Labworks electromagnetic shaker driven between 10 to 1000 Hz was used as the agitation system. Shells were bounced in pans, normally used for GDP coatings, mounted onto the electromagnetic shaker. The ideal driving frequency was about 60 Hz. At this frequency, the mandrels skated around the bounce pan instead of bouncing up and down.

The coated shells were examined optically and by scanning electron microscope (SEM) for microcracks and general integrity. The coating thickness was measured by interferometry. We measured the permeation half-life of helium, argon, and D_2 at room temperature as a measure of the permeability of the coatings to these gases. The coated shells were first permeation filled with the desired gas at elevated temperatures and then the rate of out gassing of that gas was measured in several ways. Since we found that prolonged exposure at ~300°C in the filling process led to dissociation of the inner GDP mandrels, we performed the fills at 250°C or lower to avoid damage to the GDP mandrel. Weight loss and diameter shrinkage of the filled shells as a function of time provided half-lives for helium and D_2. Direct out gassing into a sealed evacuated volume was also used for D_2 and helium half-life determinations. The decrease in the x-ray microfluorescence signal from argon inside the shell was used to determine half-lives for argon. Consistency of results obtained from the above methods provided added confidence in the measured half-lives.

The background pressure in the coating process can affect the structure and quality of the coating tremendously. Coatings deposited at 2 mtorr appeared very dense in cross-sectional SEM examination, while a coating deposited at 10 mtorr had a columnar structure. Therefore, we performed all our coatings at ~2 mtorr. This was the lowest pressure at which we could reliably sustain a plasma in our system. A typical coating rate was ~0.3 μm/h.

We initially attempted to deposit as thin a coating as possible. We found that the coating developed thousands of microcracks at a coating thickness of 0.2 μm (Fig. 2–9). However, microcracks were not observed when the glass layer was greater than 0.4 μm. We deposited coatings as thick as 3 μm. The surface finish generally deteriorated as the coating thickness was increased. The results of our experiments are summarized in Fig. 2–10. The helium permeation half-lives compare well to those of similar sized thermally prepared glass shells. The half-life appears to have a linear dependence on the glass thickness. However, the situation is markedly different for D_2 and argon. The D_2 half-life is much lower than expected for coating thicknesses of less than ~2 μm, 5 to 10 h. For comparison, a 900 μm diameter, 0.5 μm thick thermally prepared shell has a D_2 half-life of days. When the coating thickness reaches ~2 μm, the D_2 half-life increases dramatically compared to thinner coatings. Thermally prepared glass shells are virtually impermeable to argon at room temperature or at 250°C, having half-lives of several years or longer. Our coatings, however, are much more permeable to argon. Shells with coatings of all thicknesses in the range we investigated could be filled with argon at 250°C. As in the case of D_2 at room temperature, coatings thicker than ~2 μm had much longer permeation half-lives for argon when compared to thinner coatings. These results were puzzling when compared to results for helium.

Closer examination of the sputtered glass coatings on shells by SEM and atomic force microscopy (AFM) revealed a very granular structure at the submicron scale. In addition, pinhole-type defects could also be seen. SEM images showed the presence of larger nodules scattered about the surface. Pinholes may have resulted when large nodules were knocked off the surface when shells collided against each other during bounce coating. The presence of numerous grain boundaries and pinholes in the coatings on shells makes the observed relatively fast permeation rates for argon and D_2 somewhat understandable.

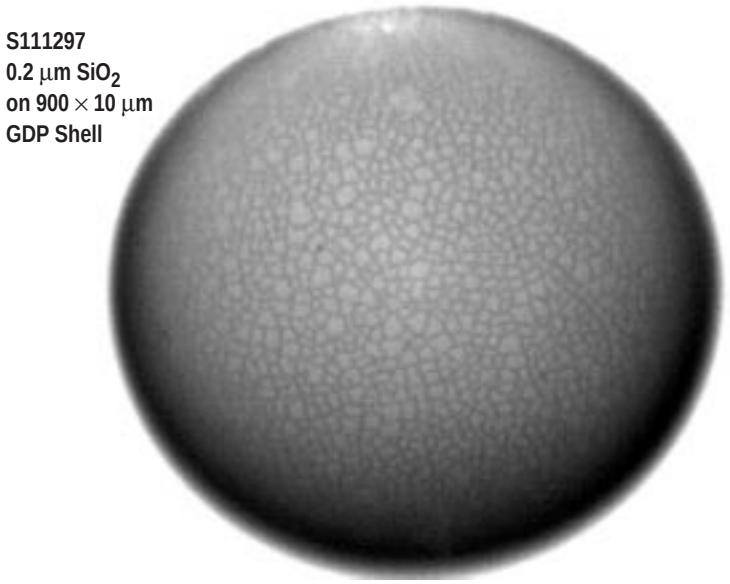

Fig. 2–9. Optical picture of a 0.2 μm glass coating on a ~900 diameter × 10 μm GDP shell. The coating had developed numerous microcracks when examined after coating. This did not happen for coatings of 0.4 μm or thicker.

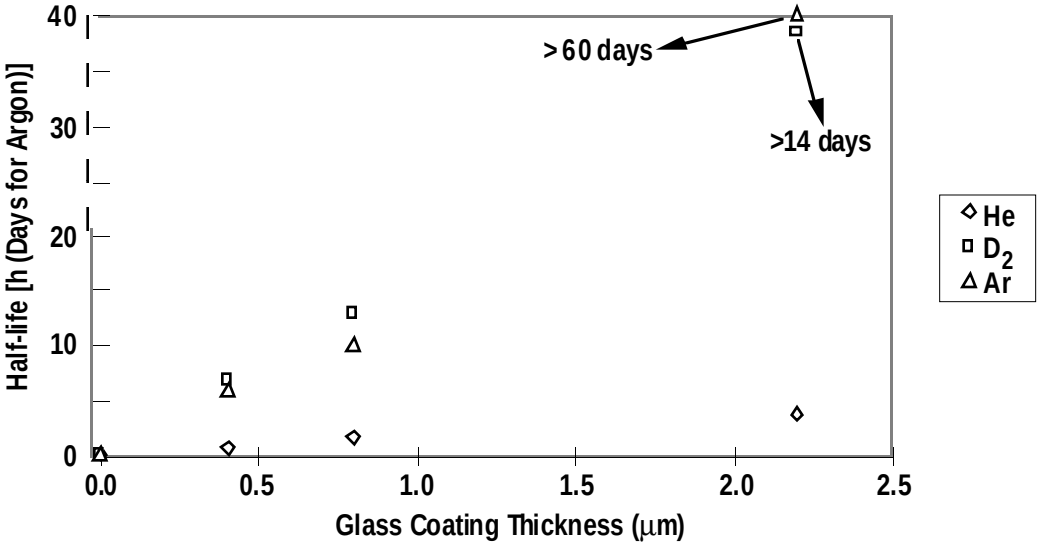

Fig. 2–10. Results of the permeation half-life measurements of argon, He, and D_2 through glass coatings of various thicknesses on 900 μm diameter GDP shells. Zero coating thickness corresponds to values for bare GDP shells. Note the different scale on the y-axis for argon. The values for He are similar to what is observed for thermally prepared glass shells of similar dimensions. However, permeation half-lives for D_2 and argon for coatings thinner than ~2 μm are appreciably lower than those expected for thermally prepared shells (see text). The permeation half-lives increase dramatically for coating thickness of ~2 μm.

This work shows that glass has potential for providing an excellent permeation barrier. However, cracking in thin layers and poor surface finish in thicker layers are significant technical challenges. Development should continue in FY99.

For further information, please contact Dr. A. Nikroo (GA).

PVA for 1.6 mm Z Capsules. SNL's recent Z experiment successes have resulted in the scheduling of ICF capsule implosion experiments for fall 1998. We fabricated the first of the fuel capsules planned for these experiments. SNL requested a variety of capsules, some of pure polystyrene (CH) and others of CH doped with 3.0 at.% germanium. The requested capsules had an inner diameter of 1600 μm and a wall thickness of 30 μm. What made these capsules challenging to fabricate was the fill gases requested, 0.1 atm of a diagnostic gas containing sulfur, and 15 to 18 atm of hydrogen or deuterium. Sulfur-containing gases consist of very large molecules and thus do not permeate easily. Hydrogen and deuterium on the other hand, readily permeate through a polymer capsule.

A PAMS bead was over coated with GDP and then pyrolyzed to remove the PAMS mandrel, leaving a hollow GDP shell behind. We used SF_6 as the diagnostic gas due to its generally inert and nontoxic nature. We found we could permeate this gas into the bare GDP shell, without damaging the shell, using a fill temperature of 200°C. At this temperature, 1600 × 30 μm GDP shells had an SF_6 fill half-life of about 4 h while at room temperature they had a half-life of over two weeks. Thus, we filled the shells at 200°C to over 90% of the final fill pressure (0.1 atm) in a day.

To hold hydrogen or deuterium in the capsule, we coated the now SF_6-filled shells with PVA, a polymer having very low permeability compared to other polymers. Figure 2–11 below shows how this was done. We picked up the shell with a vacuum chuck and immersed about two-thirds of the shell in a solution of ~5% PVA in water. We withdrew the shell and inverted it so that the PVA solution would more uniformly cover the shell while it dried under a fiber optic light source. Next, we transferred the shell to a second vacuum chuck that held it by the PVA-coated side and repeated the process of coating and drying the rest of the shell. The PVA layer averaged about 2.5 μm in thickness. We found the capsule fill half-life for hydrogen or deuterium at room temperature to be on the order of 10 days, providing enough time to mount the capsule and shoot with a nearly full gas load.

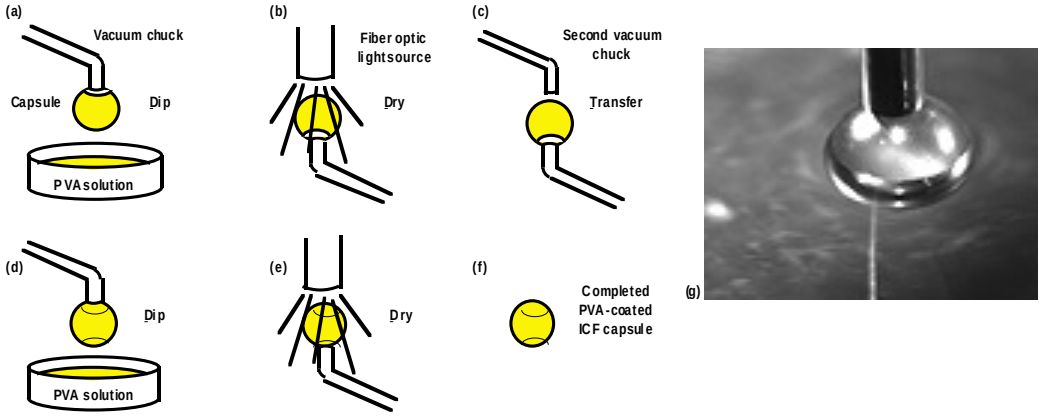

Fig. 2–11. The PVA coating process for SNL ICF implosion capsules. (g) Photograph of a 1.6 mm SNL fuel capsule being dipped into the PVA solution.

For further information, please contact Dr. A. Nikroo (GA).

2.3. CHARACTERIZATION

New experiments require new or improved characterization techniques to evaluate the deliverables. Several advances in characterization techniques are described below.

2.3.1. CALIBRATION FOR X-RAY FLUORESCENCE (XRF) ANALYSES

During FY98, we improved our XRF analysis capabilities by extending the number of elements for which our system is calibrated and by upgrading our *XRFer* x-ray analysis software. The ability to accurately model flat films was added to the *XRFer* program which in turn made it relatively simple to calibrate the XRF system for a fairly extensive number of elements simply by utilizing pure, single-element, flat foil standards. Figure 2–12 shows the measured *XRFer* count multiplier (CM) factor for many of the elements between atomic number 14 (Si) and atomic number 50 (Sn). The CM factor relates the computer model calculations to the experimental results by accounting for geometry, and fluorescence and detection efficiency for each element.

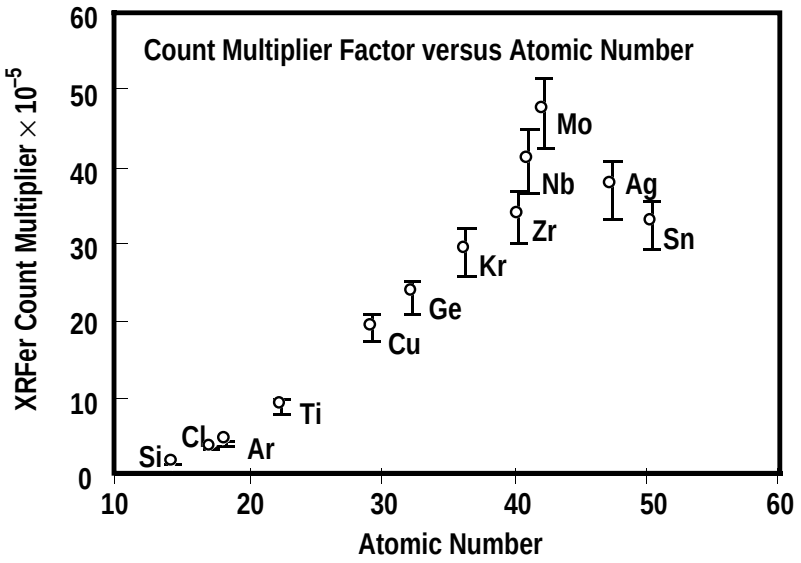

Fig. 2–12. The experimentally determined *XRFer* CM factor is shown as a function of atomic number. These values were determined at 40 kV excitation voltage using a molybdenum x-ray tube.

Interpolation between the measured elements on the graph allows us to readily determine the approximate CM for all the elements between silicon and tin. In addition, in order to confirm agreement between the *XRFer* analysis of flat-film and spherical targets, a group of **Ti**-GDP mandrels was analyzed via XRF with *XRFer* and then pyrolyzed in air to yield essentially pure TiO_2. A comparison of the calculated mass percent of titanium as determined via XRF to that determined by the thermogravimetric analysis (TGA) pyrolysis technique showed very good agreement (Table 2–4).

TABLE 2–4
COMPARISON OF THE CALCULATED MASS PERCENT OF TITANIUM AS DETERMINED VIA XRF TO THAT DETERMINED BY TGA

Sample	Pre-Pyrolysis Mass Ti-GDP (mg)	Post-Pyrolysis Mass TiO_2 (mg)	TGA (Mass % Ti)	XRF (Mass % Ti)
CH5052098	0.1120	0.0518	28 ± 1	26 ± 2

In confirming the calibration of the XRF system for titanium, an unexpected, and potentially significant benefit resulted. The combustion of the **Ti**-GDP mandrels did not lead to the expected formation of TiO_2 powder. The combustion instead resulted in the formation of high-quality, fully dense, strong and transparent TiO_2 shells (discussed in Section 2.1.3).

For further information contact Dr. M. Hoppe (GA).

2.3.2. SPECTROSCOPIC THICKNESS DETERMINATION OF SHELL LAYERS

Reflection spectra of thin films (from <1 to >50 μm thick) show intensity oscillations (Fig. 2–13) which allow one to accurately calculate their thickness. The oscillations come from interference between the film's front and back surface reflections. The path difference between the two beams is twice the optical thickness of the film (optical thickness = physical thickness × index of refraction). Even (odd) multiples of one-half give minima (maxima) in the reflected intensity. This is complicated because the index, hence optical thickness, is wavelength dependent; the resulting fringe frequency varies inversely with optical thickness.

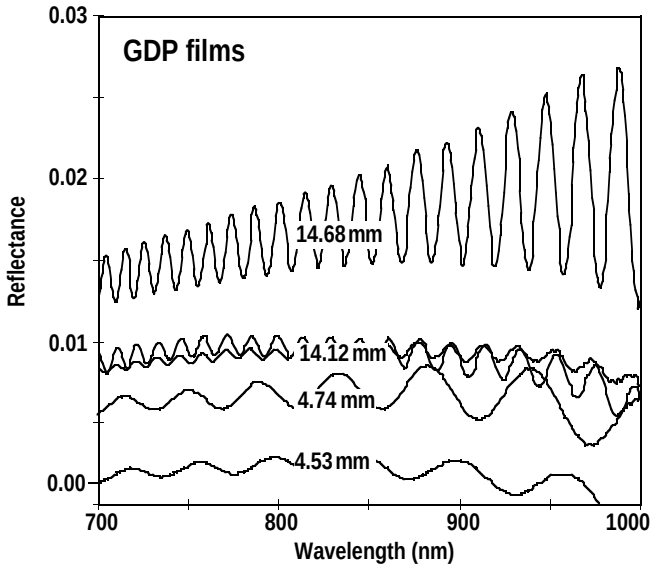

Fig. 2–13. Reflections from thin GDP films from the bottom of the GDP coater bounce pan.

We have acquired the equipment to make these measurements [2–6]. The setup is compact, convenient, and fast consisting of a fiber optic probe, a book-sized light source/spectrometer, and a portable computer. The probe, inside a ~1/8 in. o.d. steel tube, is terminated with a gradient index (GRIN) lens to focus the light (Fig. 2–14). This arrangement defines a measured region on the shell about the same size as the diameter of the fiber (50 to 100 μm). Measurements take only seconds, and compensation for varying light intensity and detector sensitivity is not generally required.

Fig. 2–14. Schematic showing how a GRIN lens improves the light collection efficiency of the numerical aperture = 0.22 fibers. The lens has a 1 mm o.d. and focuses 1 mm from the end.

We have mounted this apparatus on our AFM spheremapper and have modified the software so that it can take thickness measurements on rotating shells along the same path as a simultaneous surface profile with matched angles.

Repeated measurements on a single spot of a shell show a reproducibility in wall thickness of ~80 nm out of ~1700 nm. The angular information is not yet included. It will pick up the signal from the air bearing shaft encoder, just as the Spheremapper does, so it will be possible to match profiles and thicknesses.

For absolute thickness measurements, it is necessary to accurately know the index of refraction of the shell material(s). The value of the index for typically used materials has been determined. The index of GDP changes both during processing and with the addition of dopants (Fig. 2–15), introducing an error of ~1% if the index of GDP as measured is not independently determined.

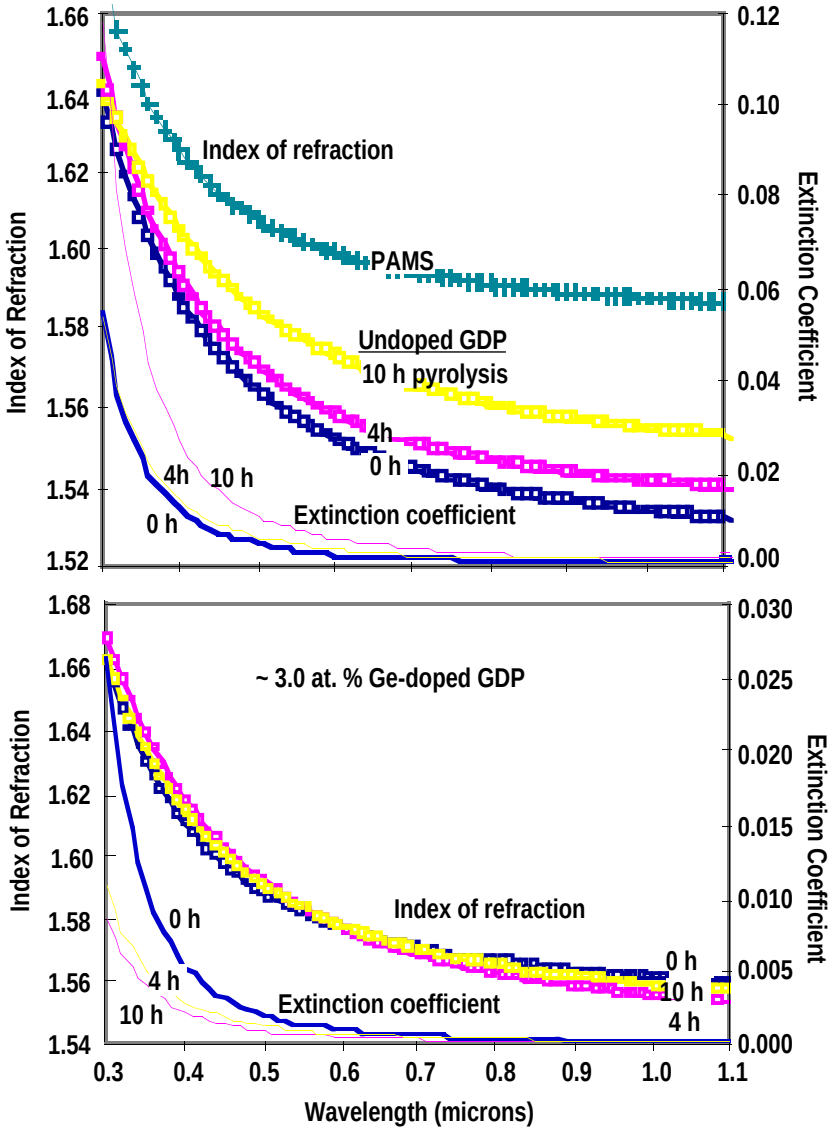

Fig. 2–15. The index of refraction and absorption (extinction) of PAMS and GDP films as a function of exposure to the pyrolysis oven and Germanium doping.

For further information, please contact Dr. R. Stephens (GA).

2.3.3. CHARACTERIZING THE SEALING JOINT OF BERYLLIUM CAPSULES

Los Alamos National Laboratory (LANL) is developing techniques to fabricate beryllium ICF capsules for the NIF using a technique to micromachine beryllium hemi-shells and to join them by diffusion bonding. The surfaces to be joined are coated with a low melting point metal, pressed together, and heated until the coating diffuses into the volume surrounding the joint. Since the added metal (Cu, Ag, or Au) is much more opaque to x-rays than the Be, (Fig. 2–16), its presence can add an asymmetry to the compression of the shell if it is not uniformly distributed. Knowledge of its distribution in the shell is critical to evaluation of this technique.

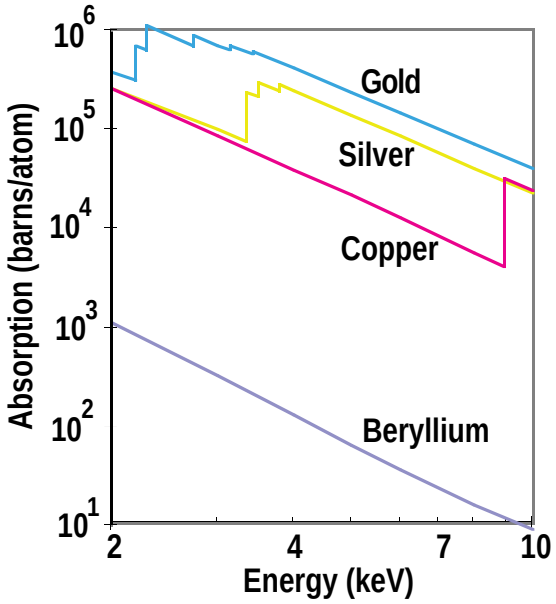

Fig. 2–16. X-ray absorption versus energy for the bonding metals (copper, silver, and gold) compared to pure beryllium.

GA has developed capability for very precise, low energy x-ray analysis of ICF targets. We have used this capability to assist LANL in evaluation of their beryllium hemi-shell bonding techniques. We have used the increased x-ray opacity to directly measure the metal diffusion. Because of the high absorptivity of the added metal, radiographs of diffusion bonded ~1 mm thick beryllium blocks (Fig. 2–17) show the concentration profile of the added metal down to <0.01 at.%. Copper is completely soluble in beryllium; the peak concentration is estimated at ~0.2 at.%, which increased the opacity by ~50%. Silver is much less soluble in beryllium. One can see from the intensity fluctuations in the radiograph that it propagates along grain boundaries. The peak concentration in that distribution is also ~0.2 at.%, but because of its higher Z, the opacity in that region was increased by ~300%. These concentrations might be satisfactory since optimized shell material composition contains a few percent copper. If the shells had been made of Be:2at.% Cu, the bars would be much more opaque to begin with, and the added opacity from these diffusion bonds would be insignificant.

Fig. 2–17. Radiographs through diffusion bonded Be joints using (a) Cu and (c) Ag. The metal concentration profile in (a) and (c) is shown by the horizontally averaged pixel values in (b) and (d).

For further information, please contact Dr. R. Stephens (GA).

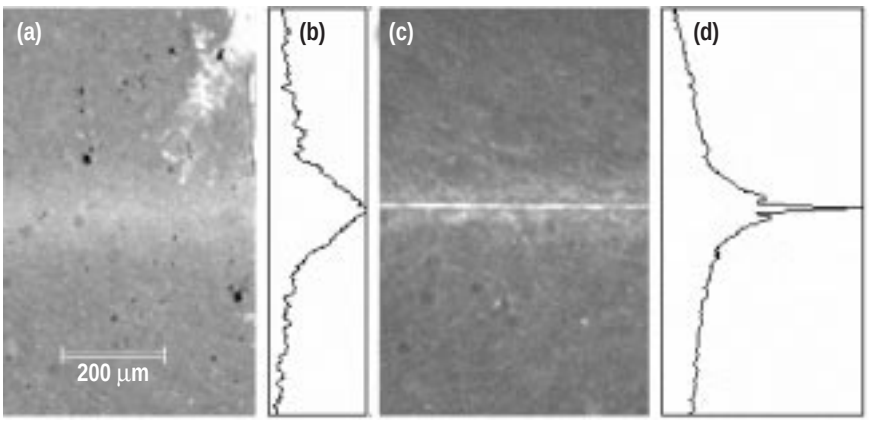

Fig. 2–17. Radiographs through diffusion bonded Be joints using (a) Cu and (c) Ag. The metal concentration profile in (a) and (c) is shown by the horizontally averaged pixel values in (b) and (d).

For further information, please contact Dr. R. Stephens (GA).

2.3.4. CHARACTERIZING THE LIMITATIONS OF AFM SPHEREMAPPING

This year, we searched for and characterized the noise sources in our AFM spheremapper. We determined that the noise intensity is generally below the NIF standard curve, so it does not usually interfere with our judgment on the acceptability of deliverable shells. However, the power spectra of our best shells drop below the instrumental noise level above mode ~20. The dominant noise source appears to be external to our building and is somewhat variable.

The AFM spheremapper setup is sketched in Fig. 2–18. Accurate measurement of the profile depends on smoothly rotating a shell under a fixed AFM head. Noise added to the actual shell profile could come from among other things: air currents moving the shell, fluctuations in vacuum pressure holding the shell down or air pressure supporting the air bearing, roughness in the air bearing, electrostatic forces on the AFM head, vibrations from the drive motor, displacement of the AFM relative to the air bearing from ground vibrations or temperature change, piezo drift, electronic pickup or drift.

There is not, to our knowledge, a sphere with a known surface roughness smooth enough to act as a reference surface, so we broke down the measurement process into component parts. Pseudo profiles were made while the AFM head was:

1. On air — not touching anything.
2. Resting on a Si wafer supported by the opposing x,y,z stage.
3. Resting on a nonrotating shell/bead supported by the opposing x,y,z stage.
4. Resting on a nonrotating shell/bead supported by the vacuum chuck.
5. Following a rotating shell/bead supported by the vacuum chuck.

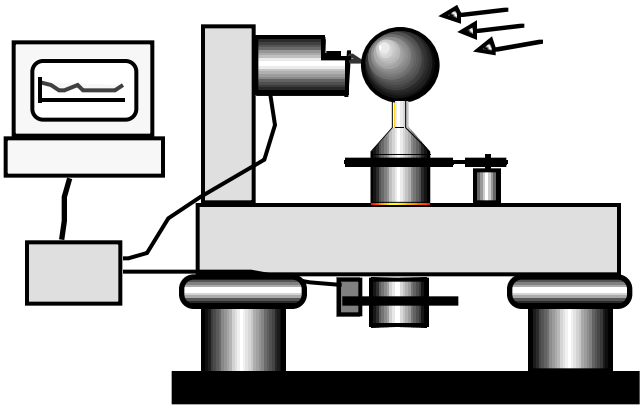

Fig. 2–18. Spheremapper schematic: the shell is held down on a vacuum chuck rotating in an air bearing next to an atomic force microscope head. The whole assembly sits on a vibration-isolated table. It is driven with a small electric motor coupled with an O–ring. Measurements of AFM height are made every 0.1 deg triggered by an encoder mounted on the bearing shaft.

Collecting these "profiles" without having a rotating shell required fooling the software because the data acquisitions are triggered by square waves from the air bearing's shaft encoder. Therefore, the air bearing was rotated (1 rpm in most cases) for setups (1) to (3), but the bearing was not touching the measured surface. For setup (4), the air bearing was not rotating; we substituted a 1 Hz square wave for the shaft encoder signal. Setup (5) is our normal configuration; in that case, we looked at differences in successive profiles over the same path.

Fluctuations recorded when the AFM tip was not touching anything were insignificant [Fig. 2–19(b)]. However, we recorded significant noise whenever the tip was touching a solid surface. The power spectrum was slightly lower when the surface was solidly supported (Fig. 2–19) than when it was on the nonrotating vacuum chuck (Fig. 2–20).

These noise levels are variable. Occasionally they exceed the NIF reference spectrum around modes 10 to 50. The frequencies corresponding to those modes are very low, «1 Hz, and appear to come from outside our building. Even when they are low, they are, for our best shells, large enough to dominate our spheremapper measurements at modes >20 (Fig. 2–21).

Modifications to make the spheremapper structure more rigid might reduce the noise level; we have some ideas in that direction. However, given the standards we are presently working toward, the noise spectrum is already so low as to not interfere with decisions about the acceptability of a measured shell. For very precise measurement of shells below the reference spectrum, it may be desirable to reduce the noise variability by taking multiple traces of the shell.

For further information, please contact Dr. R. Stephens (GA).

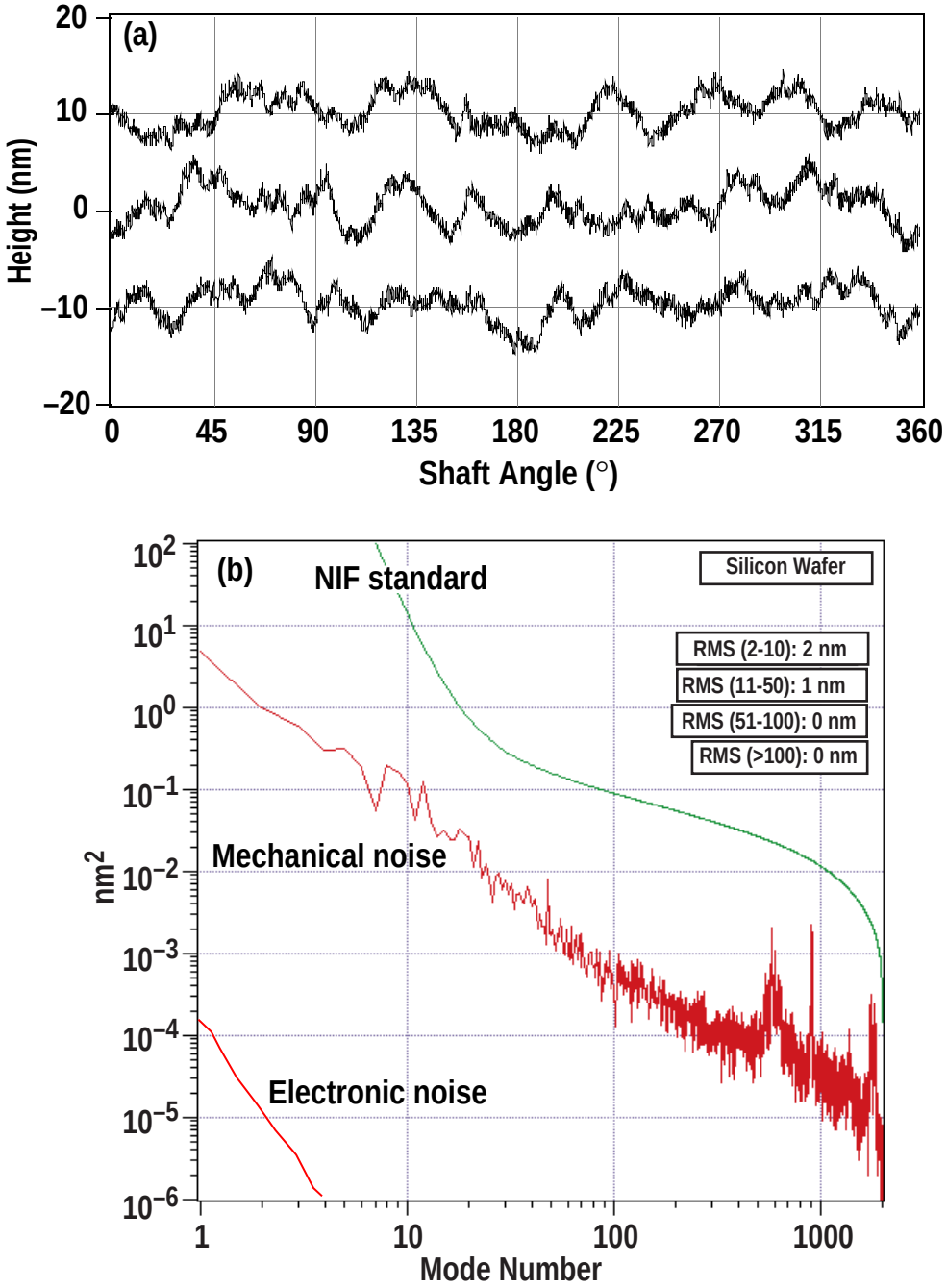

Fig. 2–19. (a) Three profiles produced when the tip was touching a flat Si wafer. The wafer was on a post supported by an xyz stage ~3 cm away. (b) The power spectrum calculated for these profiles labeled as "Mechanical Noise" and the power spectrum for profiles obtained when the AFM tip was not touching anything, labeled "Electronic Noise." The resonance at modes ~580 corresponds to a frequency of ~10 Hz.

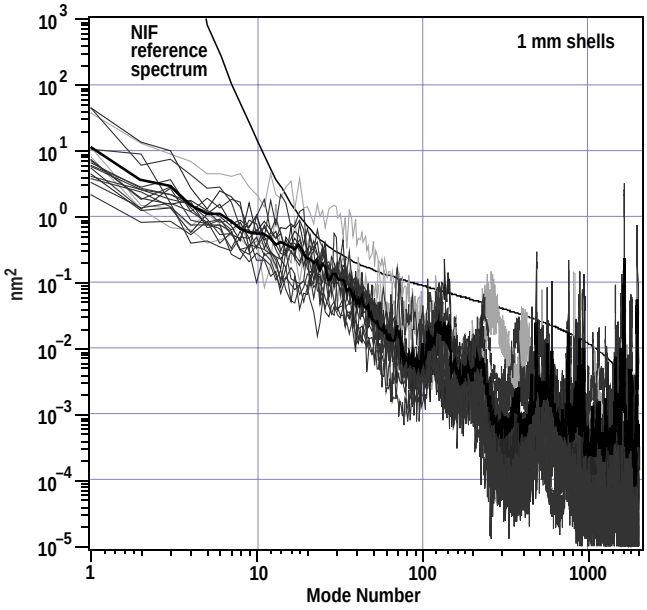

Fig. 2–20. Power spectrum from pseudo profiles collected off of nonrotating 1 mm PAMS shells (light and dark gray curves). The black curve is the average of the dark gray curves. The light gray curves are rare occurrences which have intensities larger than the NIF reference spectrum at some mode numbers.

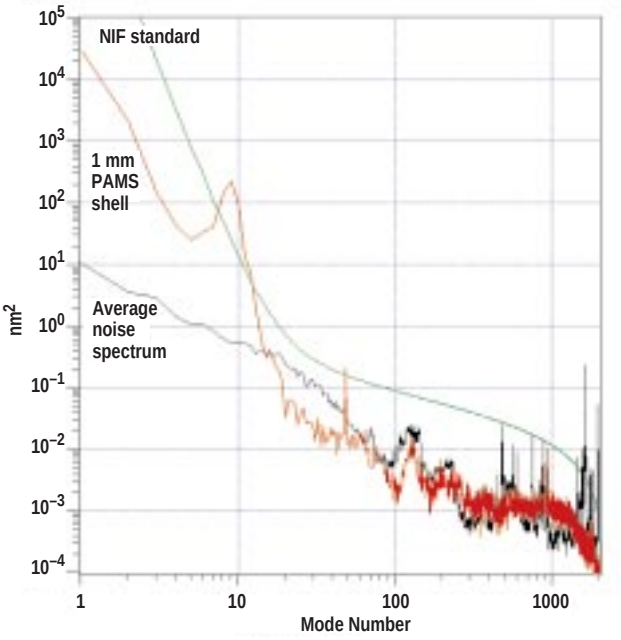

Fig. 2–21. Power spectrum of a 1 mm PAMS shell (from three orthogonal traces of a rotating shell) compared to the average noise power spectrum for 1 mm shells on our spheremapper. The dip of the shell power spectrum below the average noise power spectrum in modes 20 to 50 is due to the variability in the noise spectrum.

2.4. REFERENCES FOR SECTION 2

[2–1] T.R. Dittrich, S.W. Haan, S. Pollaine and A.K. Burnham, "NIF Capsule Design Update," Fusion Technol. **31**, 402 (1997).

[2–2] B.W. McQuillan, A. Nikroo, D.A. Steinman, F.H. Elsner, D.G. Czechowicz, M.L. Hoppe, M. Sixtus, and W.J. Miller, Fusion Technol. **31**, 381 (1997).

[2–3] A.K. Burnham, J.Z. Grens, E.M. Lilley, "Fabrication of PVA-Coated Polystyrene Shells." J. Vac. Sci. Technol. **A 5**, 3417 (1987).

[2–4] Project Staff, "Inertial Confinement Fusion Target Component Fabrication and Technology Development Support, Annual Report to the U.S. Department of Energy, October 1, 1993 through September 30, 1994," General Atomics Report GA–A21966 (1994) p. 1–8.

[2–5] D. Wilson, "Target Requirements on the Path to Ignition," Proc. 12th Target Fabrication Specialists' Meeting, June 7–11, 1998, Jackson Hole, Wyoming.

[2–6] Filmetrics F20 from Filmetrics, Inc., 10655 Roselle St., Suite G, San Diego, California 92121, info@filmetrics.com.

3. MICROMACHINED TARGET COMPONENTS

This section describes technical accomplishments made in FY98 in micromachining and foam target production. The first subsection describes improvements we have made in our micromachining capability, primarily by isolating and correcting errors in the diamond-turning machines that are used to produce machined target components. The second subsection describes a very complex double-walled hohlraum that we were asked to produce in FY98 and the steps that were required to fabricate the part. The third subsection describes foam components that we were asked to produce in FY98 and the improvement that we have made in foam component production.

3.1. IMPROVEMENTS IN MICROMACHINING CAPABILITIES

The development activities in the micromachining program at GA during the past year have been devoted to isolating and correcting errors in the diamond-turning machines that contribute errors in the parts that are produced. These errors can be separated into the categories of errors in witness plate thickness, witness plate width, and errors in remachining flats on hohlraum mandrels.

3.1.1. ERRORS LEADING TO INCORRECT WITNESS PLATE THICKNESS

Two types of error were uncovered, both of which lead to incorrect witness plate thickness. The first was misalignment of the spindle of the Rocky Flats No. 3 machine and the second was distortion resulting from rolling stresses in the aluminum flat stock employed to make the witness plates.

Alignment of Spindle. The work-holding spindle of the Rocky Flats No. 3 machine, like all diamond-turning machines, moves on air slides in a direction perpendicular to the axial travel of the cutting tool. This gives rise to two types of possible misalignment of the spindle: lack of perpendicularity between the spindle slide and the tool slide, and lack of perpendicularly between the spindle slide and the spindle axis that is mounted upon it. The first sort of misalignment results in error in facing cuts, while the second gives rise to tapered barrel cuts.

While, in principle, parts programs can be written to include corrections for such misalignments, most machines cannot respond adequately to the very small machine steps required. The standard G01 linear interpolation command used in computer numerical controlled (CNC) programming implements a taper correction each machine count, or 1.58 nm in the Rocky Flats environment, and 8.6 nm in the Precitech environment. The measured misalignment in the present case was about 0.1 deg, which means that corrections will be stored and implemented only every 10 counts ($\tan\varnothing \rightarrow \varnothing$ as $\varnothing \rightarrow 0$) in a noise-free system. In their present configurations, the Rocky Flats and the Precitech machines have noise levels ranging from 20 to 100 machine counts. The result, for the Rocky Flats machine, is that taper corrections are implemented approximately every micrometer, yielding steps

about 0.1 μm high. Such random steps were observed in slightly tapered facing cuts. The only way to correct the situation is to physically correct the misalignment and this was done during the present reporting period.

Angular displacements from perpendicularity between the spindle axis and the axis of the linear slide that carries it cause lack of flatness in facing cuts, independent of perpendicularity between the two linear axes. As long as perpendicularity exists between the spindle axis and its linear slide, flat facing cuts will be produced (recall that these cuts are accomplished by moving the part). On the other hand, three-axis perpendicularity must exist to eliminate taper in mandrel cuts. Therefore, the former correction must be made first.

The only way to change the alignment between the spindle axis and the slide axis in the Rocky Flats No. 3 machine is to loosen the 16 cap screws that hold the two components together, jostle the block-head spindle slightly with respect to the slide, tighten the screw and do a facing cut, then determine its flatness. This procedure was iterated until the original 0.1 deg error was reduced to about 0.004 deg. Then the perpendicularity between the two linear axes was adjusted by placing shims beneath the frame of the spindle slide. A correction of 0.0025 deg (accomplished with 0.002 in. shim stock) was sufficient, as determined by examining test mandrels for taper.

These two adjustments reduced the resulting spread of witness plate thicknesses from ±20 to ±5 μm.

Potato-Chipping. The "glue-up" technique employed to make witness plates was described in last year's annual report [3–1]. For this technique to be accurate, it is necessary that the thin aluminum disc into which the witness plate profile is cut be flat after it is glued to the mounting block.

Aluminum discs for the witness plates are routinely cut from 2 mm thick sheet stock of the desired purity. Face-cutting the discs removes rolling stress in the surface regions and causes the discs to deform into a shape resembling an old-fashioned potato chip with a center-to-edge distortion of 20 to 60 μm. Two procedures were implemented to eliminate this problem. First, the discs were vacuum-annealed at 550°C prior to machining. Secondly, a hydraulic press was assembled and dedicated to the gluing step in the fabrication so that any remaining "potato-chipping" would be removed.

3.1.2. ERRORS LEADING TO INCORRECT WITNESS PLATE WIDTH

The witness plate longitudinal profiles (steps, tapers, etc.) are produced in annular patterns on the aluminum discs that are discussed above, then pairs of parallel diametral lines are milled through the discs and into the supporting block. It is the separation between these parallel lines that governs the width of the resulting witness plates after the glue holding them to the block is dissolved.

These parallel lines are cut by a rotating tool mounted upon the spindle of an air turbine mounted vertically upon the tool slide. The tool is located one-half the width of the desired witness plate above the centerline of the lathe chuck holding the disc. After a diametral cut is made, the disc is rotated exactly 180 deg and a second diametral cut is made. Because of the rotation, the second cut is, in principle, exactly one witness-plate-width above the first one.

In actuality, the resolution of the shaft encoder on the spindle encoder on the lathe chuck axis is able to resolve to only 0.1 deg, which translates into an uncertainty in the distance between the cuts of ±50 μm at the location of the outermost annular pattern.

In the near term, this problem is approached by culling through the parts and rejecting those which fall outside of specifications. In the long term, we have designed and fabricated a precision indexing plate for the vacuum chuck of the Rocky Flats No. 3 machine, which will permit rotations of 180 ±.05 deg or better. It is in the process of being installed and should be available early in the next fiscal year.

3.1.3. ERROR ENCOUNTERED WHEN REMACHINING FLATS ON THIN-WALLED HOHLRAUMS

The fixturing and procedures employed in the fabrication of thin-walled hohlraums was discussed in the last annual report [3–2]. Not only is it necessary to relocate the part exactly on the spindle centerline, with the ability to rezero the axial tool positions, but it is necessary to assure that the flat machined in the hohlraum mandrel is in precisely the same (exactly horizontal) position when it is relocated after plating with metal and coating with plastic.

Occasional problems were encountered with the newest Precitech diamond turning machine when remachining the flats. It was found that sometimes the mill cut through the plastic was misaligned with respect to the original flat by as much as 6 deg, which meant that the second cut went through the plastic overcoating, the gold plating, and penetrated into the underlying copper.

While the immediate problem could be solved by installing a new shaft encoder, a more direct solution was to rely on a pair of scribe lines, one located upon the stationary housing of the spindle and the other upon the spindle itself, to position the mandrel for the mill cut, both initially and after coating and reinstallation.

A long-term solution has been bread-boarded and is being tested. It incorporates a diode laser and a photocell in conjunction with a small mirror glued into a recess cut in the side of the flange holding the mandrel (see Figs. 3–2, 3–3 of last year's annual report [3–3]). The laser and photocell are mounted upon a sturdy bracket attached to the tool table. The laser beam is reflected into the photocell by the mirror, allowing the angular position of the hohlraum to be relocated with an accuracy better than ±0.05 deg. It is important to note that this does not afford an absolute measure of spindle angle, but does allow an accurate reorientation of the hohlraum mandrel to be accomplished.

For further information, please contact Dr. Joe N. Smith, Jr. (GA).

3.2. DOUBLE-WALLED HOHLRAUMS

In the latter part of FY98, GA was asked to fabricate gold double-walled hohlraums for experiments at LLNL. As shown in Fig. 3–1, the final desired product consists of two concentric cylinders of different lengths, the outer cylinder having an external flange. In addition, the cylinder walls are separated by a distance of 50 μm but are joined together at one face. The production of each hohlraum required four separate machining efforts which were integrated with three separate electroplating operations. GA fabricated these hohlraums using the following procedure:

1. Micromachine a copper mandrel to match the internal dimensions of the inner cylinder.
2. Electroplate gold to 30 μm thickness.
3. Micromachine the gold to the length of the inner cylinder.
4. Electroplate copper to >750 μm thickness.
5. Micromachine the plated copper to the internal dimensions of the outer cylinder (exposing the underlying gold plating at the face and creating an external edge to build the flange).
6. Electroplate gold to 50 μm thickness.
7. Micromachine the extraneous gold beyond the flange and cut through a stud on the front of the part to produce a front hole when the copper was dissolved.

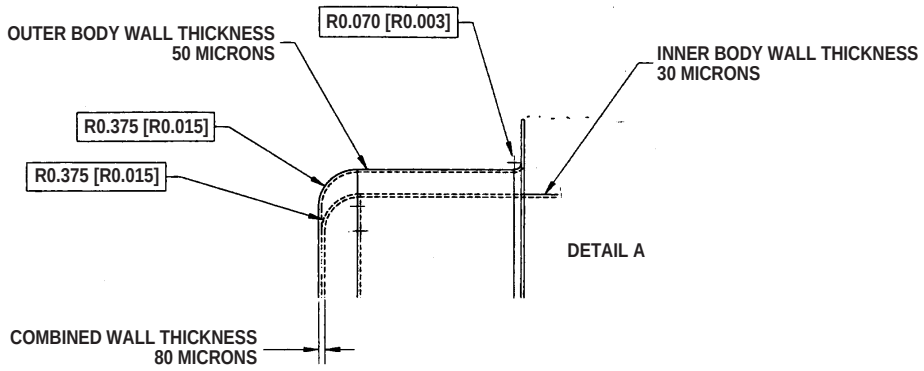

Fig. 3–1. Schematic for double-walled gold hohlraum.

After removal of the copper in nitric acid, the final double-walled hohlraum as shown in Fig. 3–2 was obtained.

Using this procedure, we were able to fabricate and deliver four double-walled hohlraums to partially satisfy the request by LLNL. More of the hohlraums are under production.

3.2. DOUBLE-WALLED HOHLRAUMS

In the latter part of FY98, GA was asked to fabricate gold double-walled hohlraums for experiments at LLNL. As shown in Fig. 3–1, the final desired product consists of two concentric cylinders of different lengths, the outer cylinder having an external flange. In addition, the cylinder walls are separated by a distance of 50 μm but are joined together at one face. The production of each hohlraum required four separate machining efforts which were integrated with three separate electroplating operations. GA fabricated these hohlraums using the following procedure:

1. Micromachine a copper mandrel to match the internal dimensions of the inner cylinder.
2. Electroplate gold to 30 μm thickness.
3. Micromachine the gold to the length of the inner cylinder.
4. Electroplate copper to >750 μm thickness.
5. Micromachine the plated copper to the internal dimensions of the outer cylinder (exposing the underlying gold plating at the face and creating an external edge to build the flange).
6. Electroplate gold to 50 μm thickness.
7. Micromachine the extraneous gold beyond the flange and cut through a stud on the front of the part to produce a front hole when the copper was dissolved.

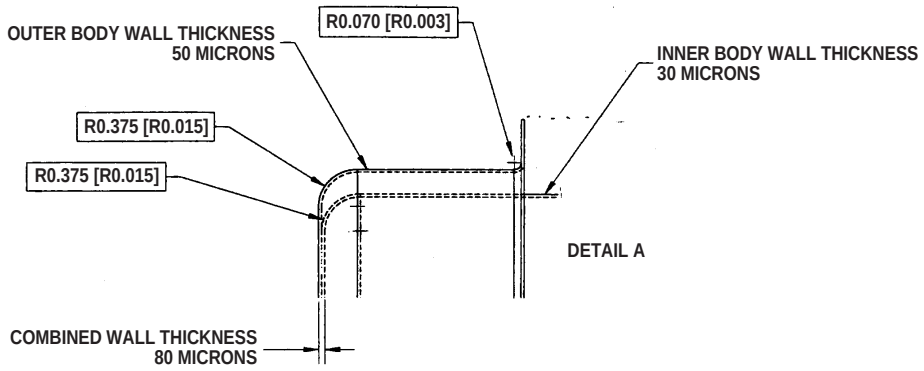

Fig. 3–1. Schematic for double-walled gold hohlraum.

After removal of the copper in nitric acid, the final double-walled hohlraum as shown in Fig. 3–2 was obtained.

Using this procedure, we were able to fabricate and deliver four double-walled hohlraums to partially satisfy the request by LLNL. More of the hohlraums are under production.

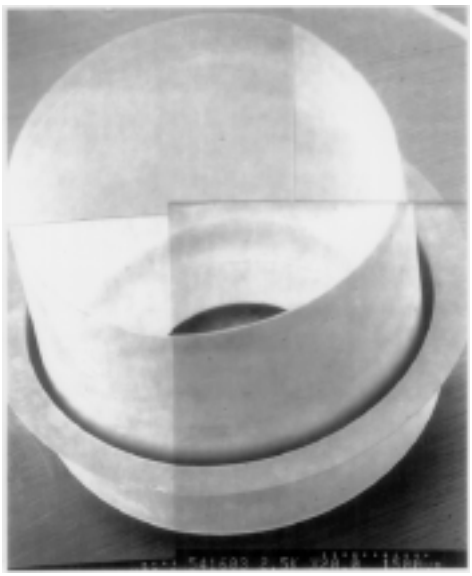

Fig. 3–2. Final double-walled gold hohlraum.

For further information, please contact F. Elsner (GA).

3.3. LOW-DENSITY FOAM PRODUCTION AND MACHINING

The production of low density foams was led by Diana Schroen-Carey of Schafer. The task statement specified the production of low-density foam "cylinders and annuli varying in dimensions, densities and polymer. About seventy (70) target components will be required." This task statement understated the number of foams that would be requested. During the 1998 task year, 179 TPX foams were requested and delivered: 380% more than the previous year and 250% more than required by the task statement. This dramatic increase in deliveries was achieved by taking a "production approach" to the entire process of requesting, producing, performing quality control.

Sandia National Laboratory (SNL) requested the foams by sending electronic AutoCAD drawings. There are three aspects of these drawings that dramatically improve productivity. First the request is written. Second, the drawing is complete with tolerances and a 3–D model. This enables SNL and Schafer to discuss the critical features of the design and proposed tolerances. Third, all revisions are made to the drawing to avoid confusion.

The production of the foams is expedited by the use of molds. Groups of molds are cast at the same time using solutions of 250 ml or more. Various geometries can be cast at the same time — the only requirement is that the final requested foam density is the same. The initial fabrication of the mold can be quite involved, but the use of molds yields great time savings as the molds are reusable an indefinite number of times. We begin by making a prototype mold to confirm the dimensional tolerance and the mold design. Mold design obviously involves shaping of all the pertinent features of the foam, but less obvious are the issues involved with removing the foam from the mold. As the

density of the foam decreases, the removal becomes more difficult. Low density foam designs often require the molds to be made in several pieces so that the removal of any one piece affects only a small portion of the surface area. The foams are not removed from the molds until after the solvent has been extracted. This prevents damage to the foams during the extraction and while removing them from the freeze drier. See Fig. 3–3 for an example of a mold and the resultant foam.

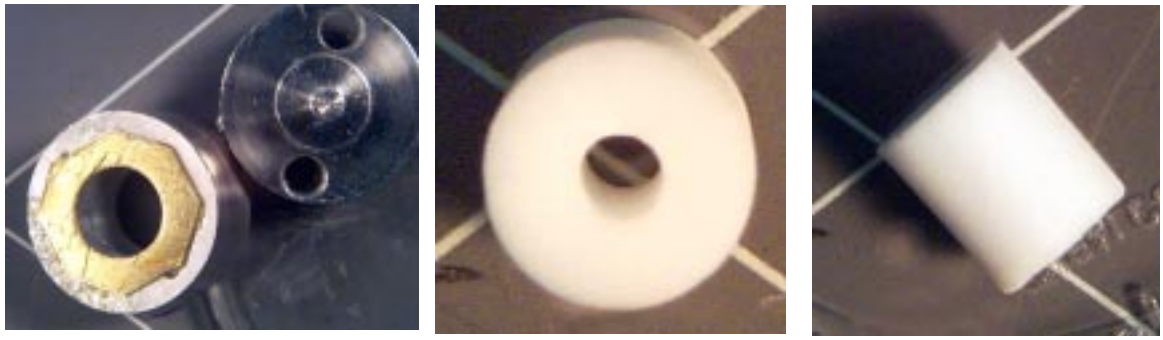

Fig. 3–3. SNL generated an AutoCAD drawing requesting a TPX foam annulus with a 5 deg slope toward the center on one end and a radius on the other. Pictured on the left is the two piece mold we fabricated to cast a TPX foam to the required dimensions. On the right are two photographs of the 6 mg/cm^3 foam showing the radius on one end and the inner diameter.

The foams are removed from the mold at the quality control station. This station includes a "set up" microscope for manipulation and overview of the foams, a calibrated characterization microscope for checking the dimensional tolerances, a precision balance for confirming the weight of each foam and a computer with CD–ROM writing ability. All data is directly entered into the computer and a CD–ROM is created for each order.

As we improved the speed with which we could produce foams, we gave ourselves time to address quality issues. The two primary concerns that SNL voiced was the need for tighter dimensional tolerances and low foam densities. We incrementally stepped down the density of the foams until we were routinely producing 6 mg/cm^3 foams with dimensional tolerances of 150 μm or less. As one example of a foam with precise dimensional tolerance see Fig. 3–4. This figure shows a 6 mg/cm^3 foam with a hemispherical depression. The depression was used to hold a capsule in the center of a hohlraum. The tolerance on the radius of the depression was 0.825 mm +0.000/ –0.0010 mm. Twenty eight foams of this type were produced.

The geometry of the requested foams did include cylinders and annuli as specified by the task statement, but also requested were thin squares, circles, and ovals that are called "hole closure foams." These foams are placed in diagnostic holes of metallic target components to prevent the holes from closing prematurely due to the plasma. Thickness is usually 0.3 to 1.0 mm and pieces are either press fit or glued on with external tabs. Figure 3–5 shows a current return can with two hole closure foams.

In summary, the 98SL02 task was a very successful task that exceeded even the most optimistic projection of deliveries. In FY99, we expect to continue deliveries at this pace with again incremental improvements to the dimensional control and lower density limit. We also hope to begin characterization of the foam structure with the acquisition of a confocal microscope.

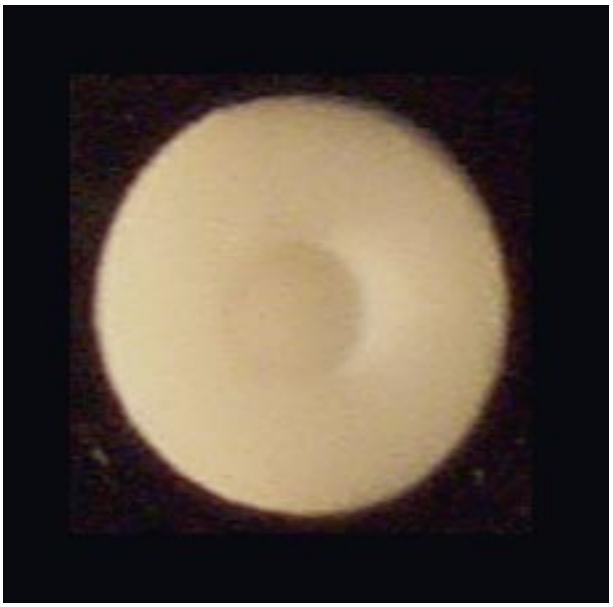

Fig. 3–4. An end on view of a 6 mg/cm^3 TPX foam with a hemispherical depression. This depression is used to hold a capsule in a Hohlraum. The target is assembled by placing one foam in the hohlraum (depression facing up), then the capsule, then another foam (depression facing down).

Fig. 3–5. A new application for low density foams is shown here. The photograph on the left is an overview of a current return can with two hole closure foams. The inner diameter of the can is approximately 51 mm. Close-up views of the foams are shown on the right side. The inside view confirms that there is no foam protruding into the can where it could interfere with other target components. The outside view documents the method of securing the foam. The 11 by 4 mm oval is cast with thin side extensions that can be tacked in place with four drops of epoxy — one at each corner. The epoxy is far from the hole so that it is not seen by any diagnostic.

For further information, please contact D. Schroen-Carey (Schafer Corporation).

3.4. REFERENCES FOR SECTION 3

[3–1] Project Staff, “Inertial Confinement Fusion Target Component Fabrication and Technology Development Support, Annual Report to the U.S. Department of Energy, October 1, 1996 through September 30, 1997,” General Atomics Report GA–A22816 (1998) p. 3–2.

[3–2] Project Staff, “Inertial Confinement Fusion Target Component Fabrication and Technology Development Support, Annual Report to the U.S. Department of Energy, October 1, 1996 through September 30, 1997,” General Atomics Report GA–A22816 (1998) p. 3–5.

[3–3] Project Staff, “Inertial Confinement Fusion Target Component Fabrication and Technology Development Support, Annual Report to the U.S. Department of Energy, October 1, 1996 through September 30, 1997,” General Atomics Report GA–A22816 (1998) p. 3–6.

4. PLANAR TARGET DEVELOPMENT

During this year, the task descriptions and requests for targets for the NIKE and OMEGA laser programs have, on the face, been very similar to those of previous years. However, significant changes in specific types of targets requested by Laboratory for Laser Energetics (LLE) and Naval Research Laboratory (NRL) have occurred throughout the year. These changes have required development of new target fabrication and characterization techniques and rapid solutions of production problems.

4.1. NIKE LASER TARGETS

NIKE targets, in the past, have generally been flat polymeric material foils mounted on polycarbonate frames designated "NIKE frames" [4–1]. The foils have been made from films cast from a solution of the polymer on a flat or patterned substrate. After casting, drying, and annealing, the films were cut into target-sized foils approximately 3×6 mm which were then characterized. After the foils were mounted on frames, characterized again and cleaned if necessary, they were shipped to NRL.

This year (FY98), many of the targets for NRL have been the flat foils on NIKE frames but more of the targets have been more complex targets of polyimide, gold, and aluminum films and various low-density foam parts. These various parts were mounted on truncated conical aluminum supports designated target front plates (TFP) or modified versions designated cryogenic target mounts (CTM) [4–2].

The simple polyimide films for the NRL targets have been obtained commercially or spin cast in our Schafer Corporation laboratory. The films ranged in thickness from 50 nm to more than 70 μm. Multilayer films have also been produced and assembled into NIKE targets. Films of three layers of polyimide (each 0.5 μm thick) interleaved with three layers of gold (each 20 nm thick) and films of ten layers of polyimide (each 0.15 μm thick) interleaved with ten layers of gold (each 6 nm thick) were developed for NIKE targets. For example, to produce the 20-layer films, the polyimide layers were formed by spincasting enough monomer on to a 10 cm diameter silicon wafer to produce a layer of the polymerized material 0.15 μm thick. After the first layer was cured in an oven following spincasting, a 6 nm layer of gold was sputtered onto the polyimide. The process was then repeated over and over until all 20 layers were deposited. We have regularly deposited four layers — two polyimide and two gold per day. However, sometimes other tasks interfered and we only managed one pair of layers per day. Thus, it required between one and two weeks of elapsed time to produce one 20-layer film, 1.5 μm total of polyimide and 60 nm total of gold. It should be noted, however, that

the film-making processes proceeded in batches so that as many as ten or more wafers were in the process at a time so that the long-term average was several completed films per day.

The multilayer films as well as uniform polyimide single layer films 1.5 μm thick were stretched over the conical surfaces of the CTMs to serve as NIKE targets. After mounting on the CTMs, many of the 1.5 μm polyimide films were coated with layers of gold or aluminum a few tens of nanometers thick.

A series of equation of state (EOS) targets was produced for NRL. Figure 4–1 is a schematic diagram of the general EOS target configuration although there were several variations on the initial design. Some of the EOS designs required several small holes in a 40 μm thick aluminum witness plate. The holes were large enough (75 μm diameter) that it was possible to drill the holes mechanically with a microscopic twist or spade drill. However, it was considered possible that the mechanical drilling would disturb the properties of the metal around the hole. We considered several ways of drilling the holes: laser drilling, chemical milling, and electrical discharge machining (EDM). We did not have a laser system which was set up to drill such holes and because of time and funding constraints, it did not seem feasible to acquire and set up a laser drilling system. Similar constraints removed chemical milling as a possible method to produce the holes. Several of us were familiar with electric discharge milling systems, having used them previously. However, commercial EDM systems were expensive and had time availability disadvantages as well. We decided to construct a simple system using Schafer parts which were available and unused.

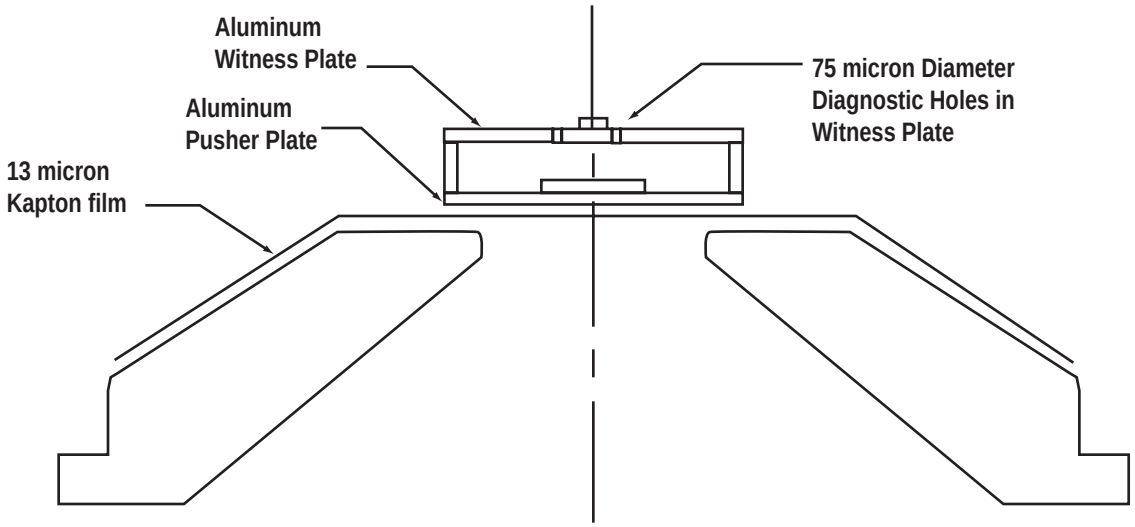

Fig. 4–1. Equation of state (EOS) witness plate step target.

4.1.1. EQUATION OF STATE (EOS) TARGETS

EOS targets for NIKE laser experiments consist of parallel machined aluminum plates accurately separated by spacers. The assemblies are mounted on a polymer film attached to a conical cryogenic target mount (CTM). Typically, the aluminum plates are 2.5 mm squares machined to provide

diagnostic ports in one plate, integral spacers at each corner to assure proper spacing and parallelism, and a central pedestal on one plate (Fig. 4–1). Individual spacers located at each corner of the plate with the pedestal were produced individually before the decision was made to machine them in place. Targets were assembled with the upper plate located with all sides parallel to the sides of the lower plate and also with the upper plate rotated 22.5 deg.

Typical thickness of the parts were 40 μm for both plates, 20 μm for the thickness of the pedestal on the lower plate, 20 μm for a groove in the top plate for some versions and an assembled spacing of 50 or 55 μm between the upper and lower plates.

Both round (nominally 75 μm diameter) and slotted (nominally 75 μm wide by 150 μm long) diagnostic holes were produced in the top plates. Each upper plate contained three such holes, two located close together to one side of the center of the target, and the other to the other side of the target center. Additionally, one of the holes was filled with a transparent polymer, machined level with the top surface of the upper plate, and coated with 200 nm of aluminum to serve as an optical barrier.

Surface finish specifications limit peak-to-valley roughness to be less than 10 nm.

The plates and their surfaces were specified to be parallel to 1 milliradians or better.

Plate curvatures less than 0.1 μm/mm were required..

Diamond-turning techniques were utilized to produce the very smooth surfaces of the upper and lower plates. A method of drilling the diagnostic hole was needed which did not work harden the surrounding metal, deform the plate, or leave burrs around the holes. Since mechanical drilling and milling operations tend to both deform the material and leave entry and exit burrs, we developed and utilized an EDM capability.

4.1.2. MICRO ELECTRICAL DISCHARGE MACHINING (EDM) APPARATUS

Conventional mechanical micro-drilling and milling techniques tend to leave defects at hole edges in the planar parts used as witness plates in the EOS targets. The defects are extremely difficult to remove without inducing additional distortion or altering the grain structure of the material. To minimize the likelihood of producing target parts that did not meet specifications because of burrs and/or material deformation, we developed entirely with on-hand Schafer Corporation materials an EDM apparatus (Fig. 4–2) for producing the diagnostic holes consistent with design specifications. The apparatus we assembled not only allowed us to produce the necessary holes but has provided us with other capabilities as well.

Among our micro-EDM capabilities, all of which are of use in producing the NIKE EOS target witness plates, are:

1. Drilling — Round holes through materials susceptible to EDM. Minimum diameters are limited by the size of tool (wire) obtainable and our abilities for aligning it in its mount. Maximum diameters are limited by the strength and size of the machine.

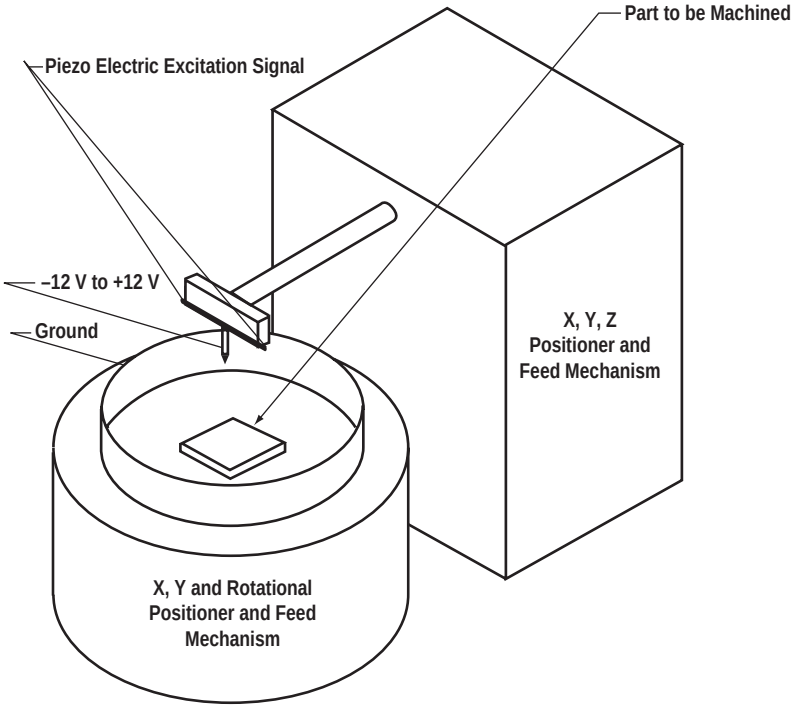

Fig. 4–2. Schematic diagram of Schafer micro-EDM apparatus.

2. Drilling — Irregular (nonround) holes through materials susceptible to EDM. Subject to the same limitations and those associated with producing the shaped tool and the need for a few microns clearance between the side of the tool and the material being machined.

3. Slotting — The production of holes of predetermined length and consistent width. This capability is used to accurately cut the plates for the EOS targets to their final dimensions (2.5 mm square).

4. End milling — As a special case of those operations described above. Micro-EDM end milling is performed with our machine to remove material from the lower plates of the EOS targets to produce the four integral spacers at the corners of the plate on which the upper plate rests and is cemented.

The operation of our micro-EDM apparatus is similar to that of all EDM machines in that a current is made to flow between an oscillating electrically conducting tool and a material susceptible to EDM in a dielectric liquid. Typical values for the voltage between the tool and the material to be machined range from approximately –12 to +12 V. Excitation frequencies have ranged from about 200 Hz to 1.5 kHz.

The mode of oscillation of the tool can be controlled by choosing an appropriate excitation frequency for the micro-machining operation desired. For instance, to drill a hole the size and shape of the tool, the tool must be made to oscillate in line with the axis of the hole to be produced. To perform slotting operations, it is desirable to choose a mode where the tool oscillates in a plane

determined by the tool and the slot to be cut. End milling operations seem to do best where the tool is made to oscillate in a plane perpendicular to the direction of cut. Additionally, elliptical holes can be produced by choosing an excitation frequency that causes the tip of the tool to describe the desired elliptical pattern.

4.1.3. PATTERNED-SURFACE TARGET FILMS

In mid-FY98, NRL supplied us with two substrates manufactured by Gentec, Inc. The substrates have a surface function, $(A/2)\sin[(2\pi/\lambda)x]*(B/2)\sin[(2\pi/\lambda)y]$, ion etched into a flat quartz surface. The two substrates have been designated Gentec No. 16 and Gentec No. 17 which have the following amplitude and wavelength parameters:

Substrate	Amplitude (Peak-to-Valley)	Wavelength
Gentec #16	0.34 μm	30.0 μm
Gentec #17	0.25 μm	60.0 μm

Using Gentec No. 16 and No. 17 as substrates on which to cast films, we have provided a series of successful sin(x)sin(y) foil targets on polycarbonate mounts for the NIKE laser program. In addition, the other quartz substrates in the list in Table 4–1 have been used to provide foils for both the NIKE laser program at NRL and the OMEGA laser program at LLE.

We have other substrates which were produced by precision micromachining of gold, copper, silver, or aluminum blanks. The surfaces of some of these have eroded to the point at which they are no longer usable. With difficulty, we can sometimes release small pieces of films cast on the eroded metal substrates but they are not useful for larger sized films, i.e., pieces larger than a few millimeters in lateral extent.

4.1.4. NIKE LOW-DENSITY FOAM TARGETS

Several versions of NIKE targets were assembled that had low density Resorcinol-Formaldehyde (RF) or other foams as integral parts of the targets. The RF foam parts were precision machined from blocks of the material either in the initial dry state or after the foams were carbonized in pure argon. The raw foams were prepared for us by Diana Schroen-Carey.

To carbonize the foams, they were heated slightly above 1000°C in flowing argon for several hours. Pieces of the carbonized foams were cut to correct size and shaped by Scott Faulk at Schafer on a precision, single-point diamond turning machine. As was expected, the surfaces of the foams were very difficult to characterize to the precision required by NRL. An infrared (IR) interferometer was assembled to examine the surfaces at long wavelengths and proved to be useful but not definitive.

TABLE 4–1
PATTERN SUBSTRATES

Substrate Number	Surface Function	P-V Amplitude (μm)	Wavelength (μm)
Gentec #01	sin(x)	0.25	12.0
Gentec #02	sin(x)	0.14	6.1
Gentec #03	sin(x)	0.10	60.0
Gentec #04	sin(x)	0.25	60.0
Gentec #05	sin(x)	0.10	20.0
Gentec #06	sin(x)	0.25	20.0
Gentec #07	sin(x)	0.10	30.0
Gentec #08	sin(x)	0.25	30.0
Gentec #09	sin(x)	0.50	30.0
Gentec #10	sin(x)	0.50	20.0
Gentec #11	sin(x)	1.00	20.0
Gentec #12	sin(x)sin(y)	0.10	30.0
Gentec #13	sin(x)sin(y)	0.10	60.0
Gentec #14	sin(x)	0.47	60.0
Gentec #15	sin(x)	0.42	20.0
Gentec #16	sin(x)	0.34	30.0
Gentec #17	sin(x)	0.25	60.0
NPL01	sin(x)	0.94	30.8
Glass Plate	Gnd 600 Sic Grit	Random Rough	
Gnd Quartz #3	Gnd 3 μm Grit	Random Rough	

To produce glassy smooth surfaces on foam parts without machining, foam parts were cast between two silicon wafer flats. The surfaces of the foams which were against the smooth silicon surfaces were glassy smooth and when the parts were carbonized, the smooth surfaces were retained. White light interference fringes were observed from the foam surfaces and showed that the surfaces were, indeed, flat and smooth. By spacing the silicon flats appropriately as the foams were being cast, pieces of foam with correct thickness were produced for NIKE targets. This technique will be pursued further during FY99 to make parts for the NRL program.

4.2. OMEGA LASER TARGETS

OMEGA laser targets are similar in nature and specifications to some NIKE laser targets. However, a large fraction of the OMEGA laser targets are multilayer films of at least two different polymers: Polystyrene (CH) and silicon doped polystyrene (SiCH). We have found the two polymers behave quite differently when they are processed to provide target films. The regular CH (nominal

molecular weight = 250,000) forms films which have good lateral strength and can be easily manipulated when they are used for target foils. The SiCH material has a much lower molecular weight. Films made from the SiCH material which we have available are very fragile and tend to crumble and require very careful handling. However, we have developed film casting and handling techniques which permit us to provide target films which are circular and several centimeters in diameter. The films are subsequently cut into much smaller discs and mounted to be used as OMEGA laser targets.

Many of the films used for the OMEGA targets are required to have a sinusoidal pattern imposed on one face, a layer of polymer, a smooth interface and another layer of a different polymer. If the layer with a sinusoidal pattern on one face is very thin, there is a tendency for the pattern to also appear on the obverse face. To avoid this "bleed-through" phenomenon, we have developed an air brush technique to apply very thin layers of the polymers. After the application of several thin layers to build up the film to an appropriate thickness, the bleed-through pattern tends to wash out to amplitudes which are quite satisfactory.

OMEGA targets which consisted of a layer of one polymer with a layer of a different polymer overlaid on the first provided some interesting and somewhat difficult problems of fabrication. The composite films were nominally 20 μm thick and were usually made up of two layers — one of normal CH and the other of SiCH. Either of the two layers could be 4 to 16 μm thick and the other layer would be thick enough to add up to 20 μm for the total thickness of the film. The interface between the layers was specified to be flat, smooth, and parallel to the two outer surface of the layered film. The first layer of a film was cast on an appropriate substrate, either a smooth silicon wafer, quartz plate, or the sinusoidal patterned surface of a fused quartz substrate. As discussed in a previous paragraph, if a thin layer was to be applied to a patterned surface, it was applied successively in very thin layers to avoid "bleed-through" of the pattern to the interface surface. After the first layer was completed, it was thoroughly cured and the second layer was applied. To avoid mixing the two polymers at their interface, we often applied the second layer of the film by air brush techniques or cast in very thin layers to build up to the final thickness without disturbing the first layer. When the films were complete and thoroughly cured, they were characterized, i.e., surfaces and thickness measured over the entire film area. The characterization data was recorded and mapped onto a 1:1 diagram of each film.

For further information, please contact Dr. C. Hendricks (Schafer Corporation).

4.3. REFERENCES FOR SECTION 4

[4–1] Project Staff, “Inertial Confinement Fusion Target Component Fabrication and Technology Development Support, Annual Report to the U.S. Department of Energy, October 1, 1996 through September 30, 1997,” General Atomics Report GA–A22816 (1998) p. 4–1.

[4–2] Project Staff, “Inertial Confinement Fusion Target Component Fabrication and Technology Development Support, Annual Report to the U.S. Department of Energy, October 1, 1996 through September 30, 1997,” General Atomics Report GA–A22816 (1998) p. 4–4.

5. CRYOGENIC SCIENCE AND TECHNOLOGY DEVELOPMENT

The OMEGA laser at the University of Rochester/Laboratory for Laser Energetics (UR/LLE) and the National Ignition Facility (NIF) at Lawrence Livermore National Laboratory (LLNL) will need cryogenic targets. We devoted effort in support of the ICF Labs to understand and control various solid fuel layer smoothing processes for both D_2 and DT fuel. We designed equipment and test pieces for laboratory work in development of cryogenic targets for NIF, and we carried out design and planning activities for the NIF Cryogenic Target System. This chapter reports some of the interesting technical results from these efforts in FY98.

5.1. CRYOGENIC LAYERING DEVELOPMENT

The major effort in support of Cryogenic Layering Development at LLNL (Task 98CR/LL1) has been in the refinement of infrared (IR) heating and beta layering techniques in spherical geometries. These experiments are designed to closely duplicate the relevant physics of the UR/LLE cryogenic layering system configuration. Experiments are performed using 1 mm o.d. plasma polymer capsules with an attached fill tube inside a 25 mm i.d. layering shroud. In the case of IR heating, the layering shroud also serves as an optical integrating sphere. We have collaborated closely with UR/LLE on the adaptation of the IR heating technique to the OMEGA Cryogenic Target System. This is scheduled to be operational near the end of FY99.

5.1.1. IR HEATING

Initial IR layering experiments used sapphire ball lenses mounted on the integrating sphere viewports to disperse the IR light inside the integrating sphere [5–1]. Using this method, more IR was incident on the shell's equator on the beam's first pass than on subsequent reflected beam passes. This resulted in a thinning of the layer near the shell equator. To remove this type of layer defect a different IR injection scheme was implemented (Fig. 5–1). The sapphire ball lenses were removed and the collimated IR laser beam was injected into the integrating sphere at an angle to miss the shell before hitting the integrating sphere wall. Experiments conducted this fiscal year employed this direct-injection technique.

Initial layering experiments were performed with shells containing HD layers typically 150 to 200 μm thick. Layers of interest for cryo targets are around 100 μm thick. Therefore, the focus of our activities this fiscal year was studying thinner layers. In addition to working on protocols for generating uniform 100 μm thick layers, we studied the time evolution of layers to determine if the surface roughness changed with time, and the effects of temperature change on a layer. Figure 5–2 shows a 90 μm thick layer. The layer rms roughness was monitored for approximately 2-1/2 h at

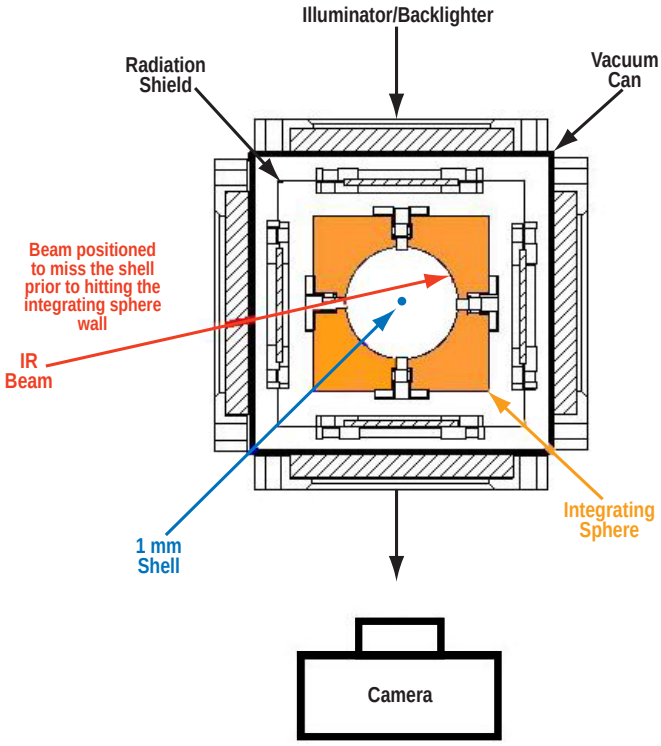

Fig. 5–1. Schematic diagram of IR direct injection technique.

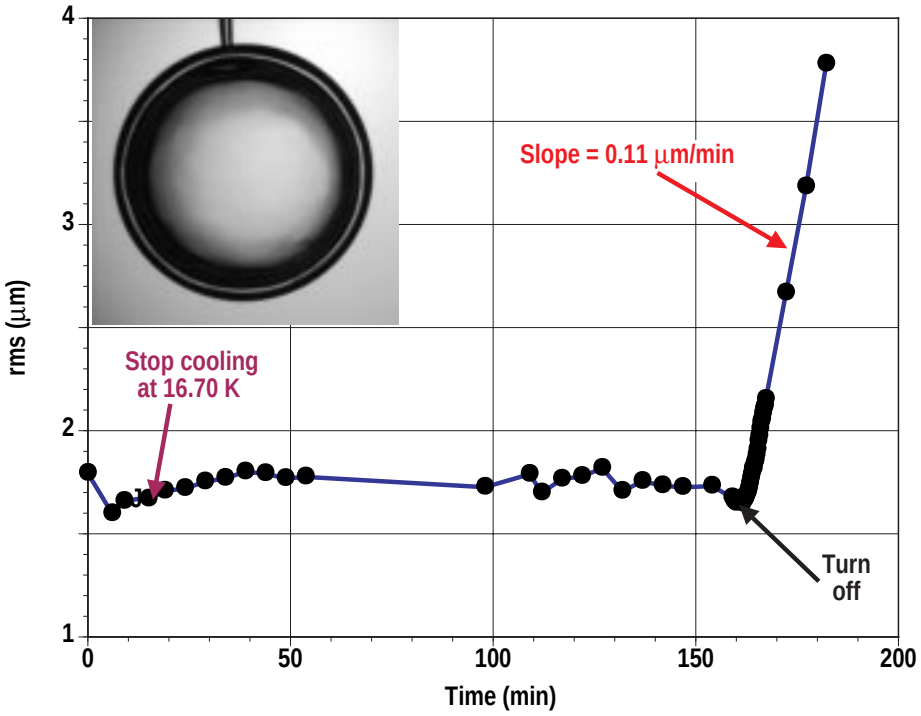

Fig. 5–2. Plot of the time evolution of the surface smoothness of a 90 μm thick HD layer.

constant temperature (16.7 K) and laser power (~1.8 Q_{DT}) without noting significant changes in the rms value. At the end of this time period, the IR was turned off and the degradation in the layer quality with time was monitored. In this case, the layer roughness increased at a rate of ~0.11 μm/min. Typically, thinner layers generated at lower illumination intensities degraded less quickly than thicker layers generated at higher illumination intensities.

Experiments conducted at Los Alamos National Laboratory (LANL) on DT layers formed in a toroidal cell indicate that the rms surface roughness of the layer decreases by abruptly increasing or decreasing the temperature of the cell [5–2]. Based on these results, one should expect to improve the surface finish of the layer by warming and cooling the layer in a step-wise fashion. We attempted a set of three temperature stepping experiments to try and reproduce the LANL results. The experiments were performed at three different layer thicknesses (150 μm, 140 μm, and 100 μm). In each case, the initial layer generation protocol was the same. First, under IR illumination, the layer was warmed up to melt the solid and then immediately cooled down at a rate of 2.5 mK/min until a solid HD layer formed. The temperature was held constant for a period of time and then a temperature step sequence was applied. Below are the results from the 140 μm thick layer experiment (Fig. 5–3). Here "t = 0" indicates the earliest time roughness calculations could be performed on the layer. These results are typical of the three experiments. We did not observe an improvement in the layer roughness. Instead, the layer degraded in quality. This apparent discrepancy of the results in spheres compared to the results in cylinders reported by LANL will be investigated in FY99.

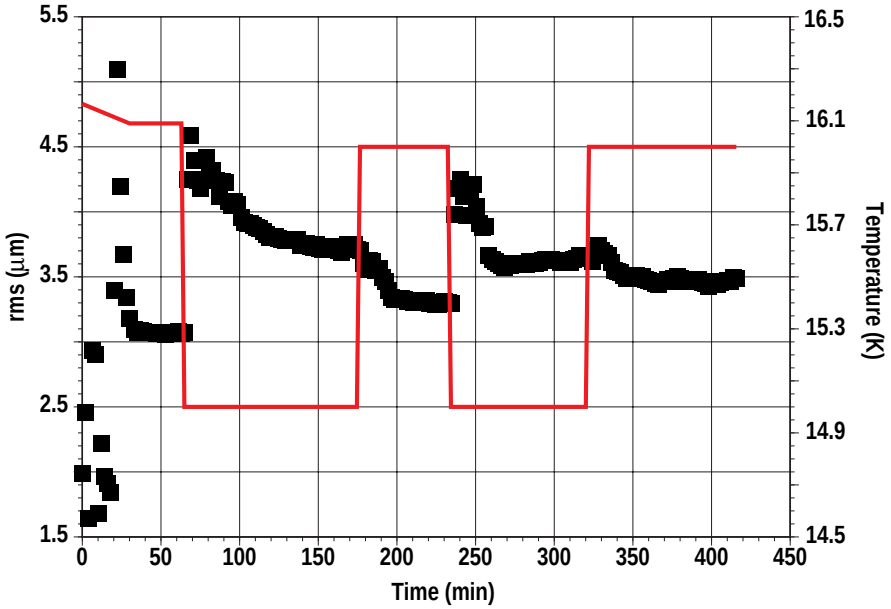

Fig. 5–3. Layer roughness and corresponding temperature versus time for a temperature stepping sequence. The solid line tracks the integrating sphere temperature and the squares indicate the layer rms roughness.

For further information, please contact Dr. D. Bittner (Schafer Corporation).

5.1.2. BETA LAYERING

Beta layering experiments have been conducted on DT in spherical capsules over the past year. The experimental apparatus has been previously described in Section 5.1.1 in Ref. [5–1]. Figure 5–4 shows the temperature and rms surface roughness, σ, evolving during the course of an experiment carried out on a three-day-old sample of DT. The roughness is calculated from Modes 2 through 128. In this experiment, we cool slowly through the triple point at a constant rate of 0.5 mK/min until the set point temperature of 19.78 K is reached. The temperature is then held constant for a period of time. The DT layer grows during the temperature ramp with a single growth front that begins near the top of the shell. The crystal growth front converges at the bottom of the shell to complete the layer. After formation, T = 19.78 K, time is 295 min, and σ = 2.65 μm. The layer continues to smooth, reaching a minimum σ of 1.15 μm at about 383 min. Afterwards, the layer roughens. This roughening behavior is not well understood.

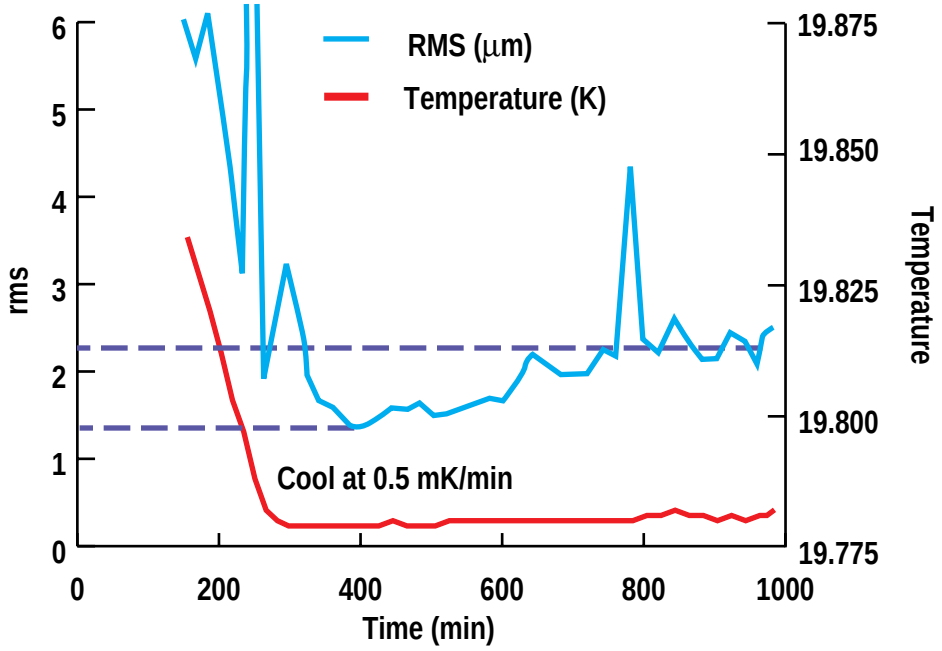

Fig. 5–4. We observe that the layer smoothes to a minimum value and then roughens with longer times.

Figure 5–5 shows the power spectral density for the layer at 400 min and at 1000 min. It is apparent that the layer at 400 min is smoother at all mode numbers except perhaps at a singular point at Mode 7. Most of the difference between the two layers occur in Modes 2 through 4.

Data indicate that σ increases with decreasing layer thickness. In Fig. 5–6, we have collected all of our layering data with cooling rates between 1 and 2 mK/min and layer thicknesses between 150 and 225 μm. The 4.2 μm point was for a layer formed at the upper end of the cooling rate. Figure 5–7 contains the power spectral density for a 152 μm layer and a 220 μm layer. The thicker layer is substantially smoother at all mode numbers. This could be due to the observed relative ease that thick

layers nucleate as compared to thin layers. A contributing factor is the increase in the variation of temperature near the ice/gas interface with thicker layers, i.e., $\delta T_{bump} = Q\ h\ \delta h_{bump}/k$. δT is the variation from the average temperature at the ice/gas interface. δh is the variation from the mean ice thickness.

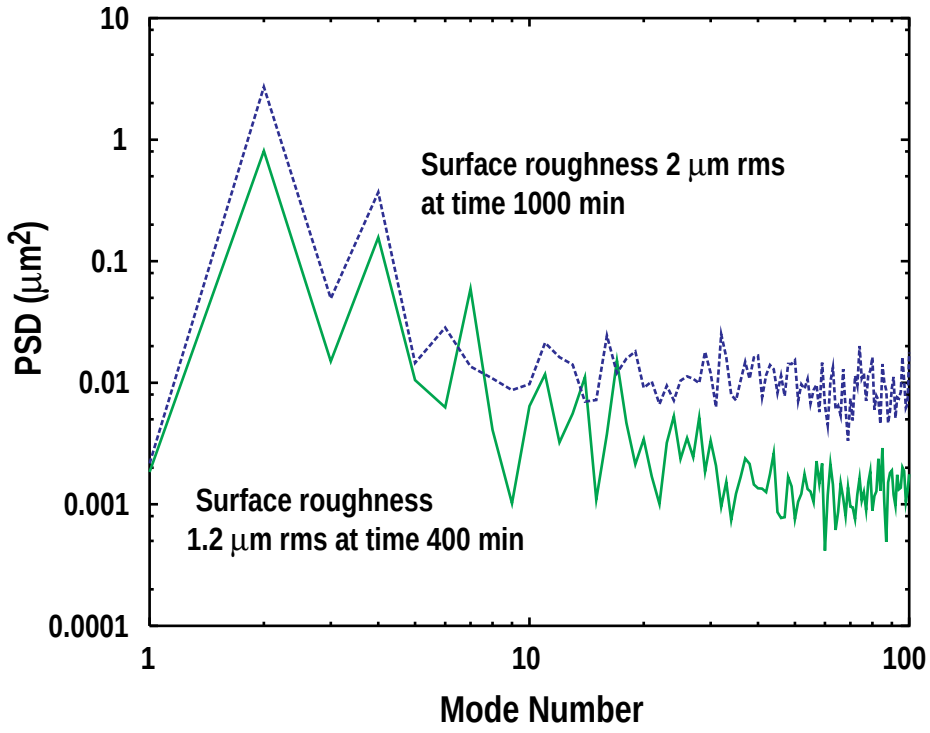

Fig. 5–5. Increase in roughness over time after minimal is largely due to effects at modal numbers between 2 and 4 though the largest relative increase occurs above Mode 20.

Layers at temperatures below $T_{TP} - 0.5$ K are typically rougher than layers produced just below T_{TP}. Currently, NIF ignition target designs contain 80 μm thick DT layers at 18 K inside a 2 mm o.d. capsule. Our best DT layers are produced just below T_{TP} at about 19.7 K. The gas density inside of the capsule is $\rho_{gas} = 0.7$ mg/cc instead of the specified $\rho_{gas} = 0.3$ mg/cc, and thus would change the convergence of the ignition capsule design.

For further information, please contact Dr. J. Sater (Schafer Corporation).

5.1.3. PARTING JOINT TESTS

To implement IR-enhanced layering on the OMEGA cryogenic target handling system, a method must be developed to couple the IR radiation from a laser into the layering shroud containing the D_2 filled capsule. The current concept is to run an optical fiber from the laser into the moving cryostat, up along the outer cryostat shroud, and into the layering shroud. The path will be basically the same as that for the electrical wiring. This requires a remote make-and-break connector at the shroud parting joint. A mockup of the parting joint was fabricated and parts were designed, fabricated, and

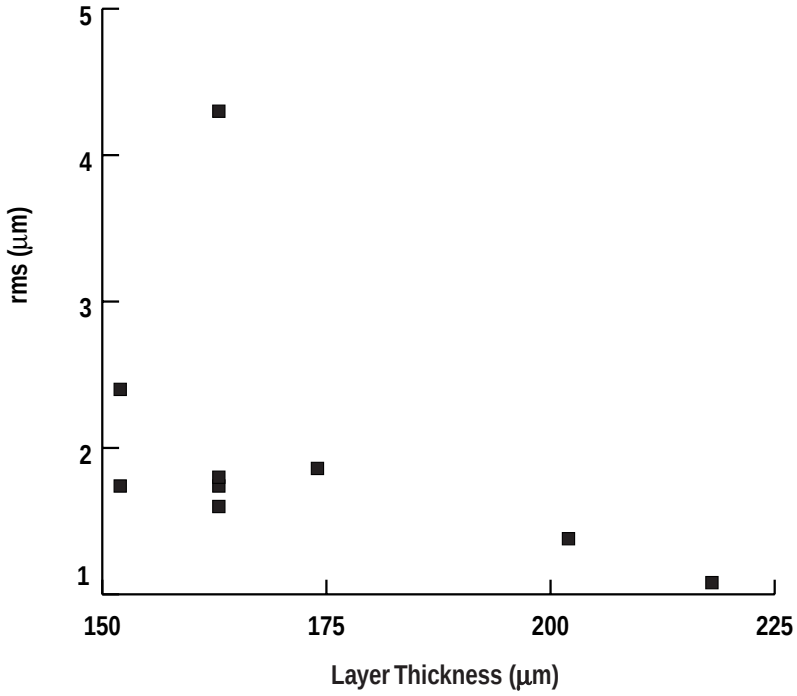

Fig. 5–6. Thinner ice layers have a larger σ.

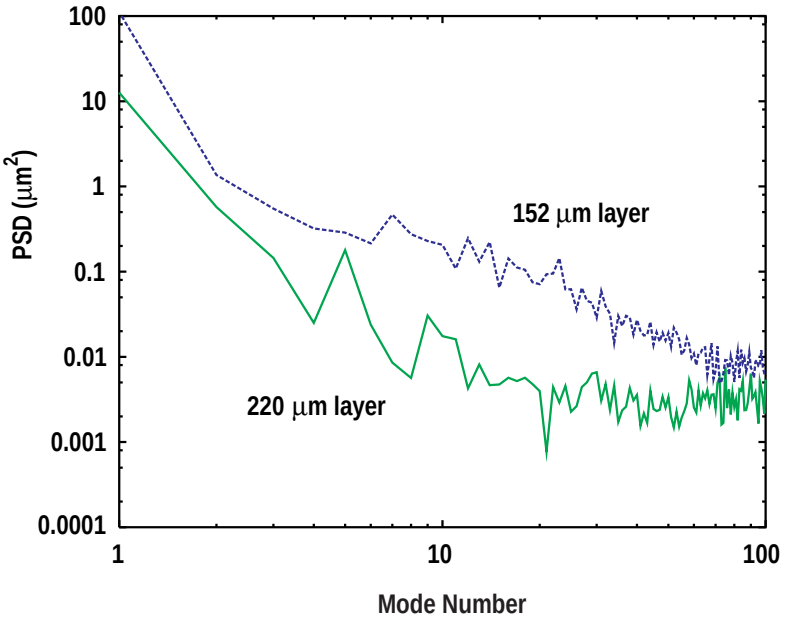

Fig. 5–7. The power spectral density plots indicate that a large amount of excess power for the thinner layers is in the middle part of the modal spectrum.

tested for connecting the optical fiber cable in the lower half of the moving cryostat to the optical fiber in the upper retractable shrouds. Below is a picture of the parting joint mockup (Fig. 5–8).

Fig. 5–8. Picture of the parting joint mockup.

Since the optical fiber connection will be made remotely, a relatively simple and reliable method needed to be developed. The concept used involves a pair of conical shaped parts that self-align as the two sides of the parting joint come together. Figure 5–9 is a close-up of the conical fittings that screw onto SMA fiber connectors. To maintain compression at the joint, one side of the assembly is spring-loaded. A small sleeve contains the spring and also helps to maintain alignment. Figure 5–10 is a picture of the assembled connectors.

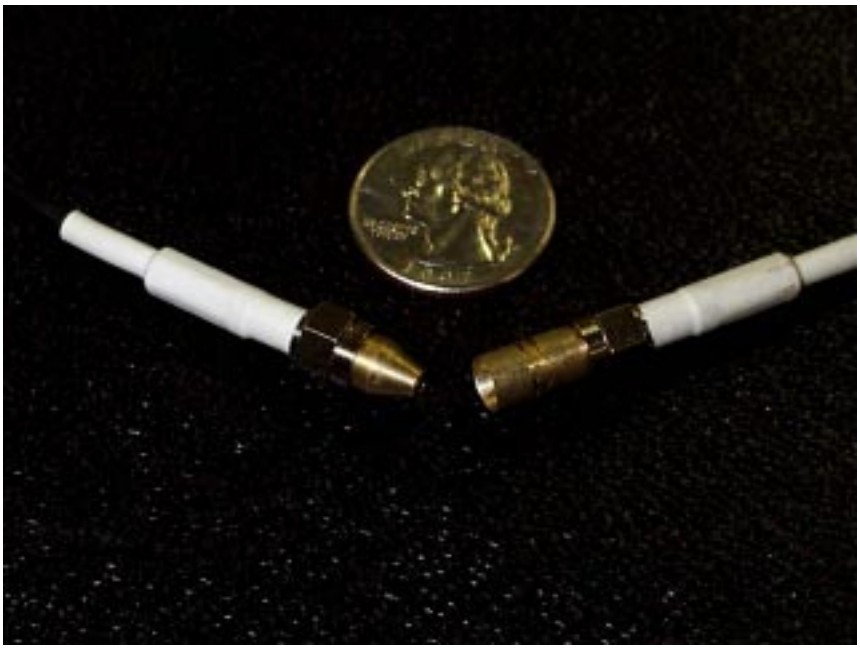

Fig. 5–9. Picture of the conical fittings attached to SMA connectors.

Fig. 5–10. Picture of the assembled parting optical fiber connection.

For further information, please contact Dr. D. Bittner (Schafer Corporation).

5.1.4. MONTE CARLO STUDIES OF SHADOWGRAPHIC ANALYSIS OF UNIFORM ICE LAYERS IN SPHERICAL CAPSULES

A Monte Carlo analysis of theoretical shadowgraphic images is being conducted. We are using TracePro, a program developed by Lambda Research, to study the quantitative effects of surface defects on the image of the ice layer. Figure 5–11 shows the layout we use in our analysis. It should be noted that the incident light source is a plane wave. This is an idealization, since our experimental setups use a diffuse source for illumination.

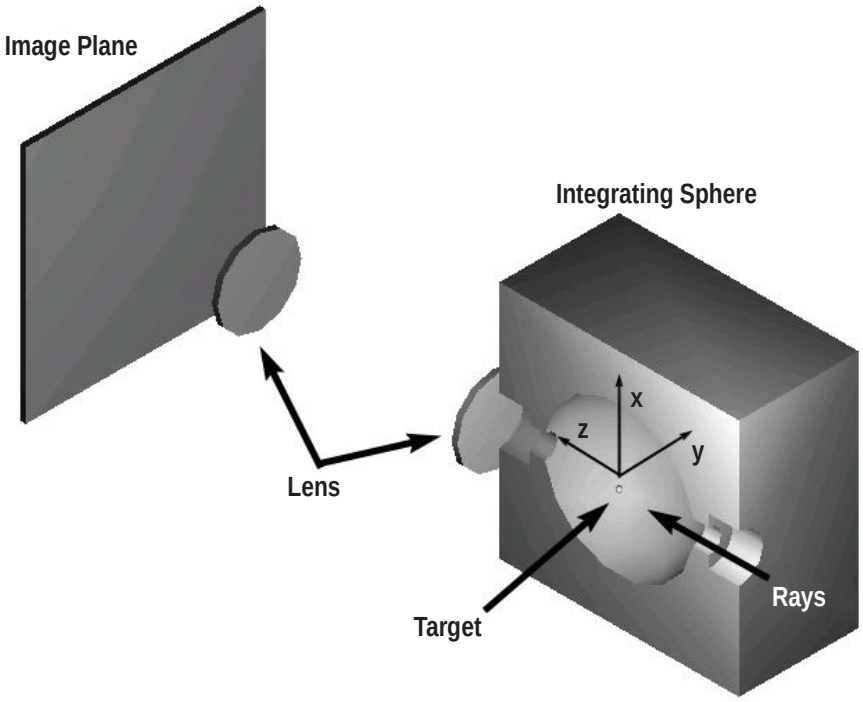

Fig. 5–11. Model setup for investigating ice surface defects (only half of the integrating sphere is drawn for clarity).

A 1 mm o.d. capsule with 10 μm wall thickness is located at the center of the integrating sphere. The inside of the capsule has a uniform ice layer 100 μm thick. Different sizes of bumps or holes are added (Fig. 5–12) to the ice solid/vapor interface to simulate layer defects.

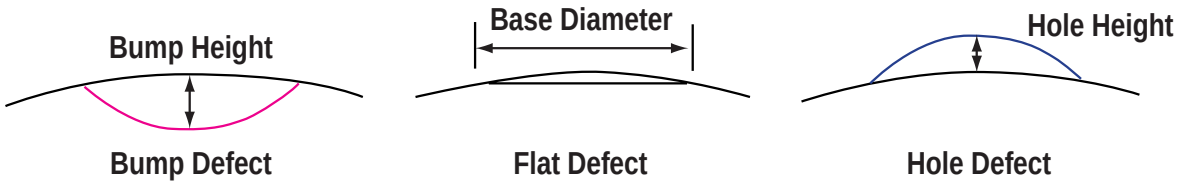

Fig. 5–12. Possible surface defects on the ice layer.

A simple optical system consisting of two thin lenses with identical focal lengths is used in our analysis to form an image of the ice layer edge. The location of the center and the irradiance (brightness) of the bright band is calculated with and without a bump or hole. Figure 5–13 shows the visual effect on the bright band image with the presence of various surface defects. Currently, only small (~5 μm) and moderate (20 to 90 μm) size defects have been studied.

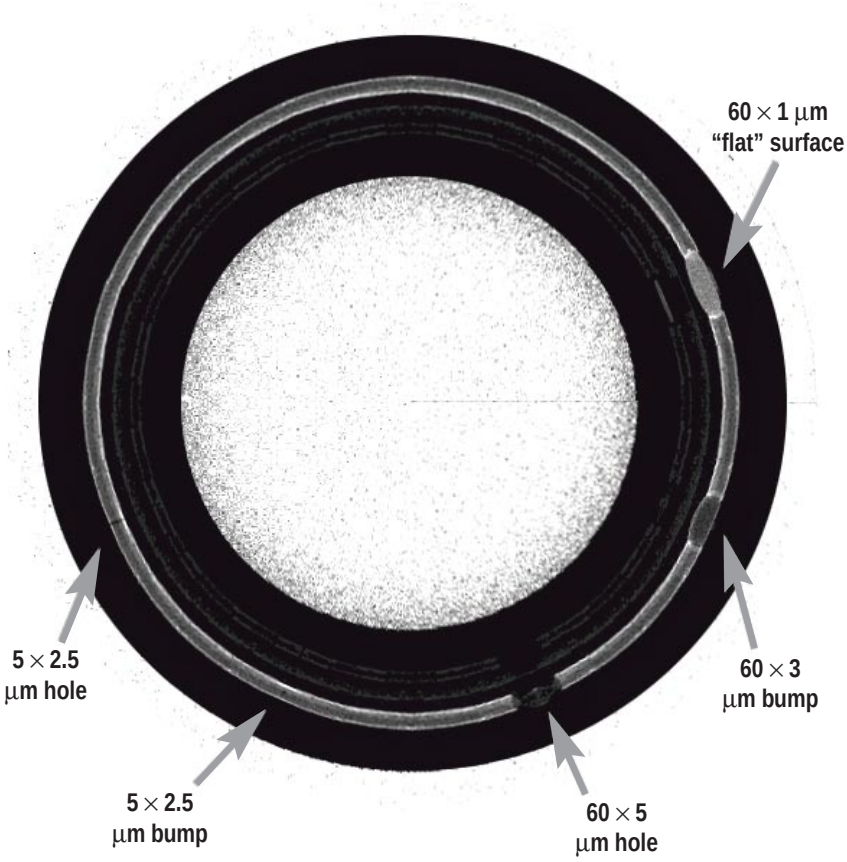

Fig. 5–13. Target image generated computationally with different types of surface defects.

When a small 5 μm diameter bump is placed on the layer, some of the rays that would normally contribute to the bright band impinge upon the bump and are refracted to other areas of the image plane. This causes a very small loss in band brightness at that location. For small bumps, the bright band center position does not change, since the spatial extent of the bump is smaller than the area on the ice surface that contributes to the bright band. In contrast, when a small hole of 5 μm diameter is placed on the ice layer, there is a loss of intensity because the rays aimed directly at the hole plus most of the other rays that would contribute to the bright band are scattered by the hole boundary. The bright band is drastically reduced in intensity at that location, and the presence of a small hole is much more noticeable than a similarly sized bump.

One to 3 μm thick bumps and holes with base diameters ranging from 20 to 90 μm have also been investigated. Results are shown in Fig. 5–14.

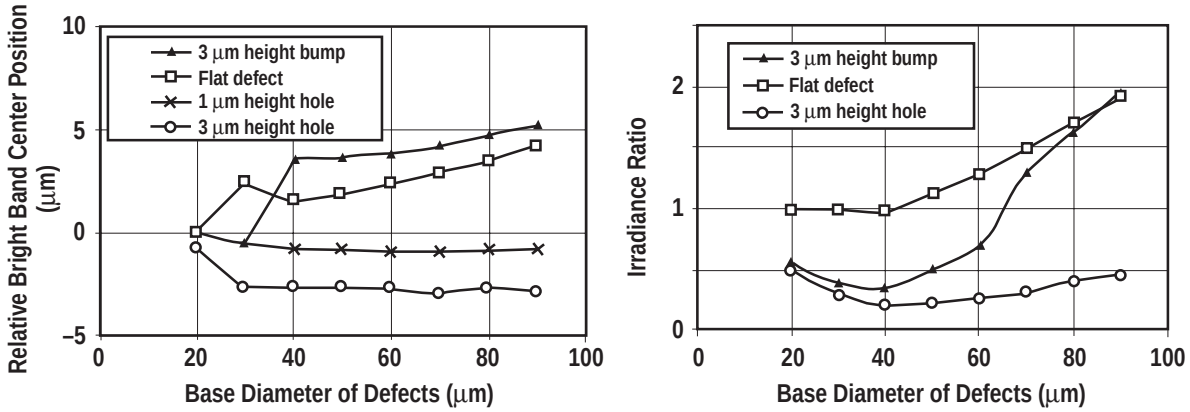

Fig. 5–14. Effect on the location and irradiance ratio (average brightness of the defect band region/average brightness of perfect band region) of the bright band due to the presence of moderate size defects.

In general, the band tends to move away from the center of the image when a hole is present and moves toward the center when there is a bump. If the defect is from 20 to 40 μm in size, the band position becomes difficult to determine. The extent of the defect is roughly the same size as the ice surface area that reflects light into the bright band.

As shown in the right side of Fig. 5–14, a hole will create a dark spot on the band. A bump will also create a dim spot on the band until the curvature of the bump gets close to a flat surface. For a flat defect (a bump with infinite curvature), a bright spot will be formed.

For further information, please contact Dr. Y. Lee (Schafer Corporation).

5.2. BETA LAYERING SUPPORT AT LANL

Experiments were performed in a 2 mm beryllium torus, to examine the effects of progressively lower tritium fractions on the surface roughness (σ_{rms}) of solid DT. Each experiment consisted of several β-layering equilibrations, in which the DT solid layer was melted and refrozen at the end of each equilibration.

The preliminary design of the cryogenic pressure loader (CPL) data acquisition and control system was completed and most of the parts are now in-house and ready for assembly. This system will control the target insertion and layering sphere mechanisms as well as the optical system x-y-z stage positioners. Additionally, the system will acquire DT cell image data as well as cell and cryostat temperature data.

5.2.1. TRITIUM FRACTION EXPERIMENTS IN THE 2 mm BERYLLIUM TORUS

Tritium fraction experiments [5–2] were those in which the fraction of tritium in the DT mixture was progressively reduced from an initial value of 98.5% to a final value of 3.9% for each successive experiment. Each experiment was performed at a temperature of about 0.5 K below the mixture triple point; and each consisted of β-layering equilibrations in which the equilibrated layer was melted and refrozen several times. These experiments were performed to examine the effects of tritium fraction on the surface roughness of a β-layered DT solid.

At the end of each experiment about 350 torr of the DT mixture was first removed to provide a sample for mass spectrometer analysis. This was followed by a dilution in which a predetermined quantity of D_2 gas was added to the DT mixture. After several experiments and once the tritium fraction reached 50%, a predetermined quantity of DT gas was removed prior to the dilution to keep the total DT gas inventory nearly constant.

Figure 5–15 is a graph of the layering cell temperature (liquid fill, equilibration, and triple point temperatures) as a function of tritium fraction in the DT mixture. The three data points shown were obtained from Table 1.1 in Souers [5–3], for pure T_2, a 50–50 DT mixture, and pure D_2. The curves shown are second-order polynomial fits to the three data points. This graph was used to properly set the liquid fill and equilibration temperatures as the DT mixture was diluted from the 98.5% initial value down to 3.9%.

Figure 5–16 shows three images of equilibrated DT layers at 98.5%, 31.1%, and 3.9% tritium. Each of these images represents one cycle of several for each dilution experiment. Equilibration time and temperature, solid layer thickness, and σ_{rms} are also indicated in this figure. Roughening of the solid layer, as the tritium fraction is reduced, can be clearly seen in these three images; but the layer is remarkably smooth (4.1 μm) even with the tritium fraction at 3.9%. Layer thickness for these three experiment cycles ranges from 73 to 96 μm and is not a factor influencing the final rms roughness values. Faceting can be clearly seen in the 3.9% tritium equilibration of image 3, and is an indication that the beta heating generated in the 3.9% tritium solid layer is not enough to overcome the energy barrier presented by the D_2 crystal structure described by Bernat [5–4].

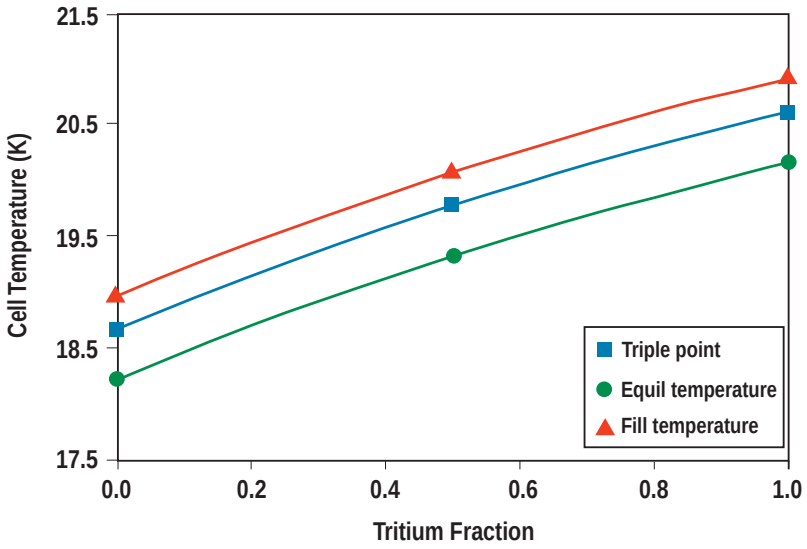

Fig. 5–15. Variation in cell temperature required to maintain the proper liquid fill and solid layer equilibration temperatures as the tritium fraction in the DT mixture is reduced from 100% down to 0%. The DT liquid fill temperature was selected to be 0.3 K above the triple point, and the equilibration temperature was selected to be 0.5 K below the triple point.

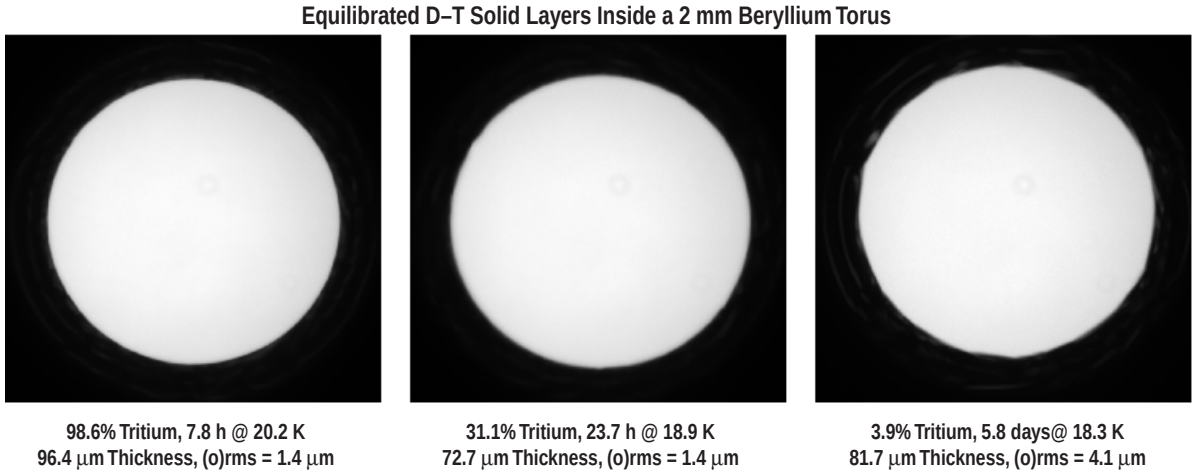

Fig. 5–16. Image sequence showing the degradation in the equilibrated DT solid surface roughness as the tritium fraction is reduced from 98.5% to 3.9%. The equilibration times and temperatures are indicated as well as the solid layer thickness (μm) and rms roughness (σ_{rms}).

Several β-layering cycles were performed for each experiment with the final equilibrated σ_{rms} values averaged for each dilution. Figure 5–17 is a graph of these averaged σ_{rms} values as a function of tritium fraction [f = T/(T+D)]. Also included in this graph is plot of theoretical values calculated by Bernat [5–4] for a 100 μm DT solid layer at 18 K. The points shown for the calculated values were extracted from the Bernat curve and are shown as squares; and the LANL experimental values

are shown as solid circles. Both experimental and theoretical values are fit with a hyperbolic function as shown. This graph shows that σ_{rms} for solid DT equilibrated at 0.5 K below the triple point is nearly flat ($\sigma_{rms} \approx 1.4\,\mu m$) down to 30% tritium after which the surface slowly roughens. Nonetheless, the solid surface is remarkably smooth even at a fraction of 3.9% T in the DT mixture. This provides an opportunity for using a low T-fraction DT mixture in possible future dudded experiments at the NIF.

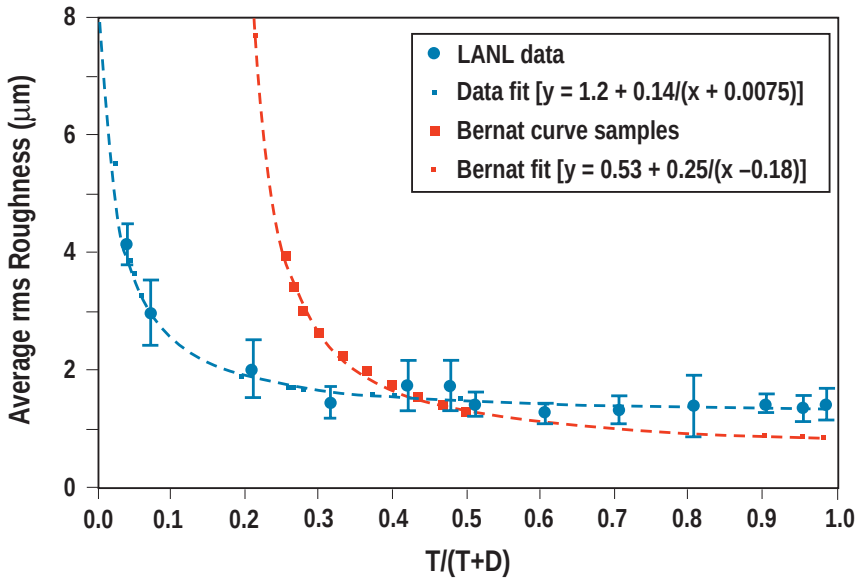

Fig. 5–17. The relationship between σ_{rms} and tritium fraction in a DT solid layer (solid circles), for experiments performed in a 2 mm beryllium torus at an equilibration temperature 0.5 K below the triple point. Also shown are theoretical values calculated by Bernat (solid squares) [5–4], for a 100 μm DT solid layer equilibrated at 18 K.

5.2.2 CPL DATA ACQUISITION AND PROCESS CONTROL SYSTEM DESIGN

The CPL system is a target filling and β-layering apparatus designed to test permeation fill operations with DT, as well as measure tritium migration from the permeation cell apparatus to other regions within the cryostat and associated plumbing. This system is intended to provide process and operational data relevant to DT operations with the OMEGA Cryogenic Target System at UR/LLE, before it begins tritium operations. The CPL will also permit the study of native β–layering in a permeation-filled Inertial Confinement Fusion (ICF) target under actual field conditions.

The CPL cryogenic apparatus includes a permeation cell, in which targets are inserted and filled; a layering sphere into which filled targets are inserted and positioned for β-layering operations; numerous temperature sensors; and an optical system that monitors the DT filled cell and acquires image data at specified intervals, once the cell is positioned in the layering sphere apparatus. The data acquisition and control system for the CPL apparatus is designed to provide automated control of the target insertion and layering sphere apparatus, automated control of the optical apparatus used to

position image acquisition optics, and automated computer acquisition of temperature and image data. Figure 5–18 is a block diagram schematic of the data acquisition and control system showing all of the components currently designed into the system. This system will be interfaced within a LabView [5–5] integrated software environment running in MicroSoft Windows NT™.

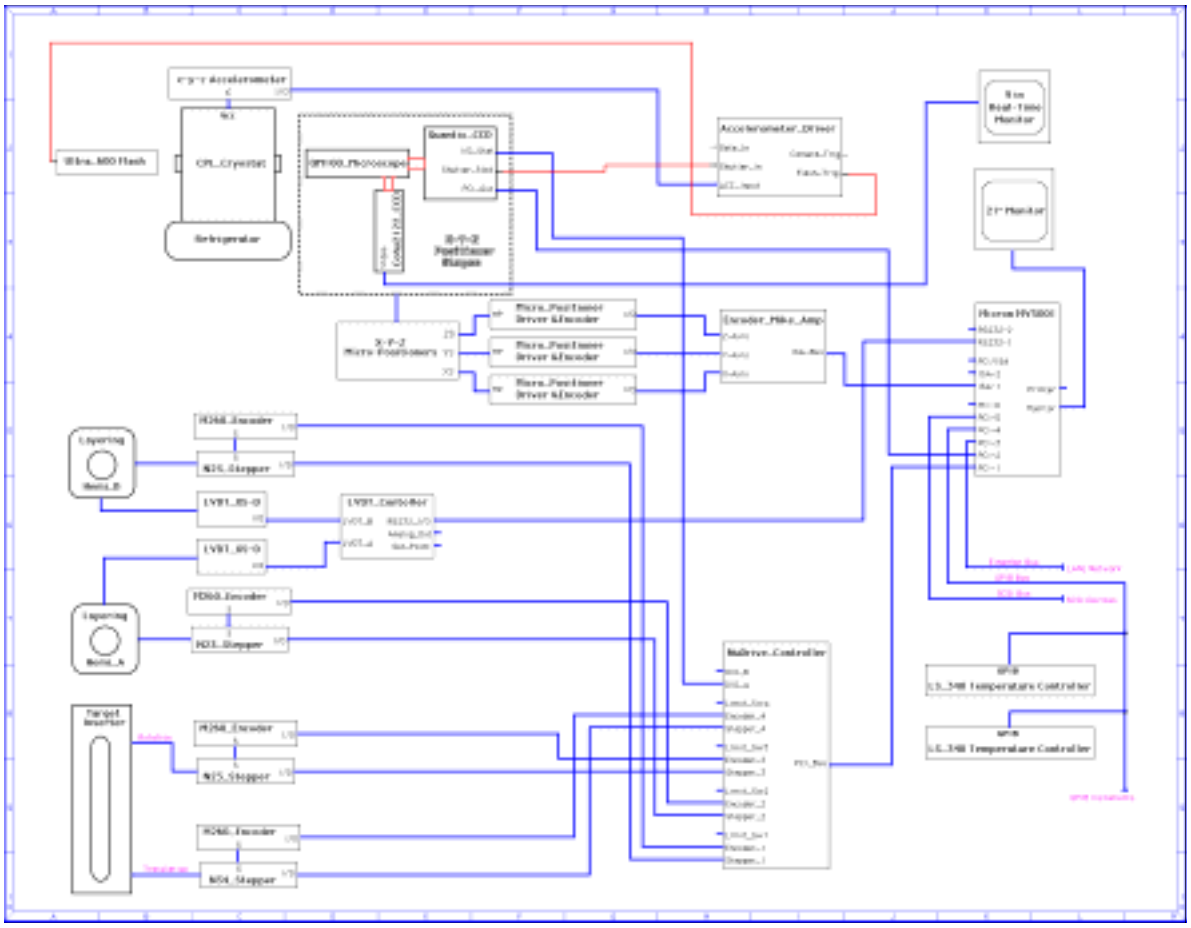

Fig. 5–18. Block diagram of the CPL data acquisition and control system. The controlled devices are the target insertion mechanism, layering sphere mechanism, cryostat temperature controllers, and the x-y-z positioning stages and flash illuminator for the target imaging system. Data is acquired from temperature sensors, position sensors, and shaft encoders and cryostat motion accelerometer.

For further information, please contact J. Sheliak (GA).

position image acquisition optics, and automated computer acquisition of temperature and image data. Figure 5–18 is a block diagram schematic of the data acquisition and control system showing all of the components currently designed into the system. This system will be interfaced within a LabView [5–5] integrated software environment running in MicroSoft Windows NT™.

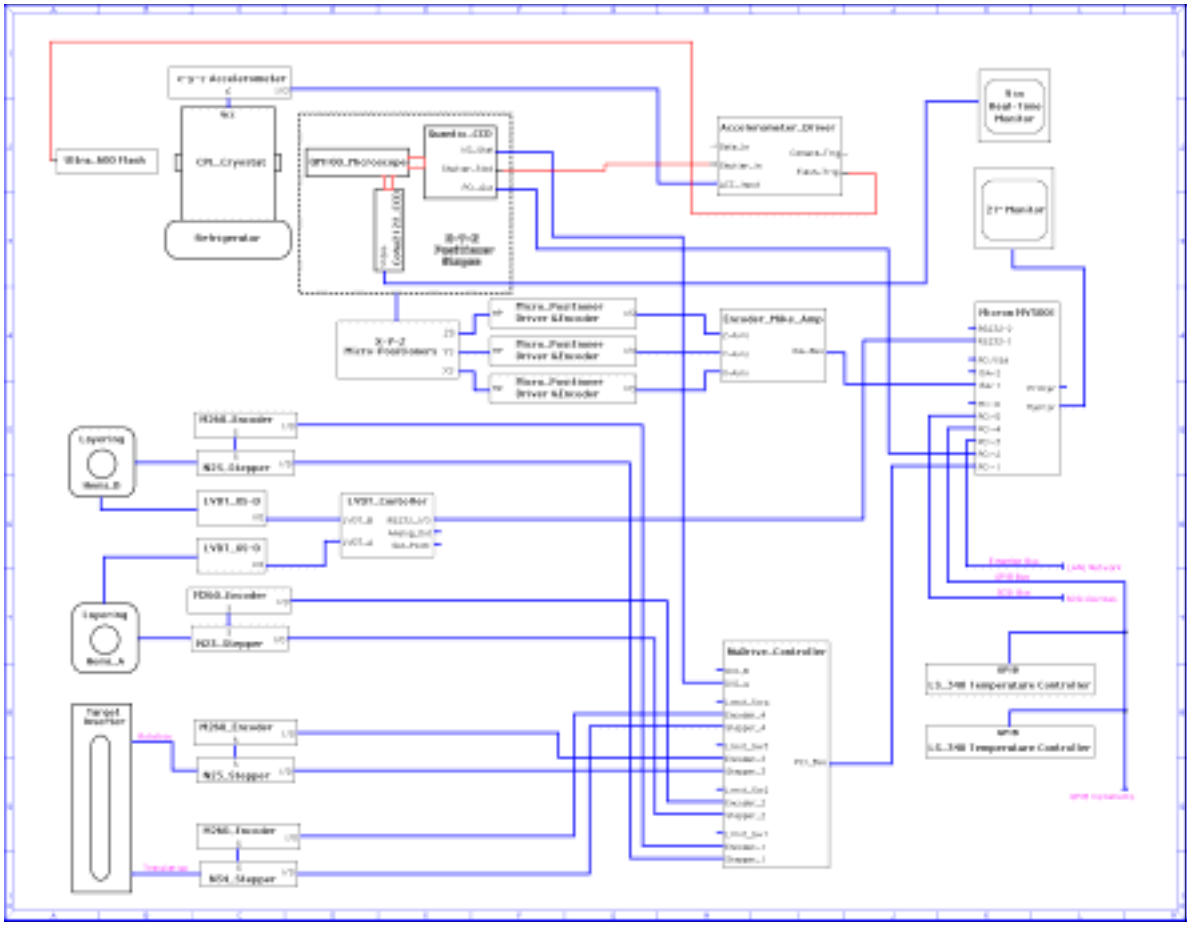

Fig. 5–18. Block diagram of the CPL data acquisition and control system. The controlled devices are the target insertion mechanism, layering sphere mechanism, cryostat temperature controllers, and the x-y-z positioning stages and flash illuminator for the target imaging system. Data is acquired from temperature sensors, position sensors, and shaft encoders and cryostat motion accelerometer.

For further information, please contact J. Sheliak (GA).

5.3. CRYOGENIC HOHLRAUM DEVELOPMENT FOR NIF

One of the possible ways to field a cryogenic ignition target on the NIF is to layer the DT fuel in the capsule before the hohlraum is assembled around the capsule to form the target. To keep the fuel solid, the assembly of the hohlraum must be done cryogenically — at approximately 18 K. The beta-layering process that is on-going in the DT fuel causes the fuel to distribute along isotherms. The addition of the hohlraum around the capsule imposes a cylindrical symmetry to the isotherms surrounding the capsule. Thus, the target must be shot immediately after the hohlraum has been assembled, before the fuel has had time to redistribute into a nonuniform layer corresponding to the altered isotherms. This is anticipated to occur in approximately 10 s. With this short a time, the assembly would have to be done in the NIF Target Chamber. This fielding technique is referred to as the in-chamber cryogenically assembled hohlraum (CAH) technique.

We have supported the CAH technique by developing a design for the CAH target that is suitable for cryogenic assembly. Experimental tests were conducted on possible seals to be used in fastening together the hohlraum.

A conceptual design was developed for a cryostat for the D_2 Test System. This system is meant to allow high density deuterium-filled targets to be filled, layered, and examined, and to allow some key component and interface tests for the NIF Cryogenic Target System to be conducted.

5.3.1. CRYOGENICALLY ASSEMBLED HOHLRAUM (CAH) DESIGN

A CAH target design has been developed. The design allows for the target to be rapidly assembled at cryogenic temperatures. The hohlraum is separated into two halves. Each half has a brim added to it that attaches the hohlraum half to an inner seal ring. The capsule is mounted between tented films that extend out to an outer seal ring. The outer seal ring is made up of two halves that are glued together to trap the capsule's mounting film. Both the inner and outer seal rings have a face, tapered at a 9 deg angle, running their circumference. This is where the seal rings attach to each other. Assembly is done by opposing anvils that grab the inner seal rings and press them simultaneously into the outer seal ring. This locks the inner seal rings and outer seal ring together in a frictional lock in the same way that collets are held into engine lathes. The 9 deg cone seal of the rings must hold in approximately 1/2 atm (8 psi) of a helium-hydrogen tamping gas mixture that will be added into the hohlraum just before the shot. The leak and sealing characteristics of the 9 deg cone seal will be reported on in Section 5.3.2. The inner and outer seal rings are copper. The hohlraum and brim are gold, 30 μm thick. The mass of the target is 0.5 g. The design is shown in Fig. 5–19 just as the hohlraum halves are being joined to the mounting ring. The large anvils holding the hohlraum halves by their inner seal ring are part of the cryogenic assembler — they are not part of the target. They will be removed just before the shot as the target insertion cryostat's (TIC) shroud is retracted.

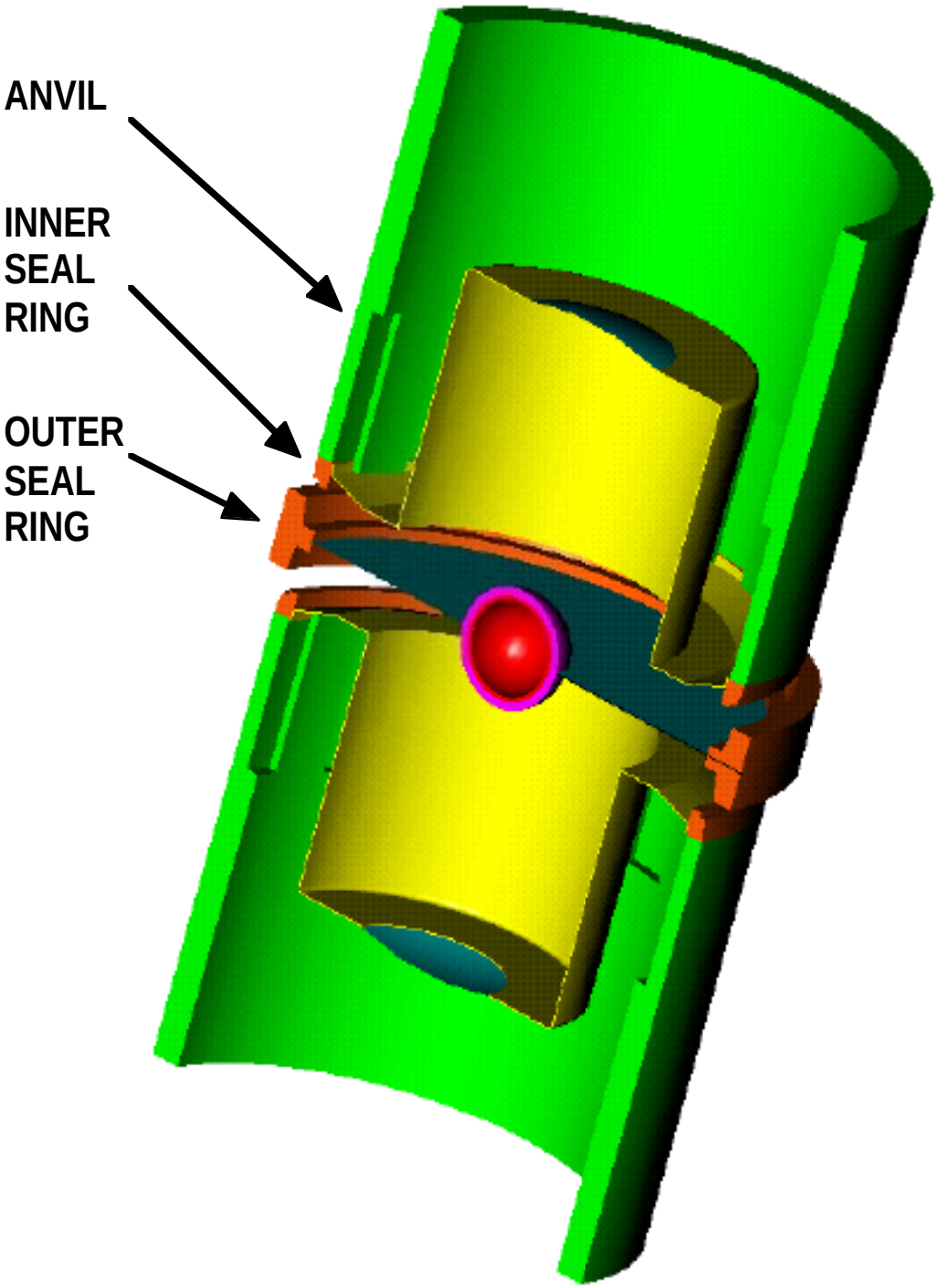

Fig. 5–19. The CAH target design has been modeled in a 3D solid CAD program and is shown with a half section removed. The anvils are part of the assembler mechanism that will build the hohlraum. They are not part of the target. The target is shown in this figure as it is being assembled, just before the inner and outer seal rings are joined. For scale, the outer diameter of the capsule is 2.22 mm.

Finite element thermal analyses were done in ANSYS to determine the effect of the inner mounting ring (closer to the target) on the uniformity of the DT fuel layer in the capsule. A number of inner ring geometries were analyzed (Fig. 5–20). The results from all of these models is shown in Fig. 5–21. This figure plots the maximum variation in the heat flux on the capsule versus the thermal conductivity of the outer seal ring. In these models, the capsule and inner seal ring are placed into a 15 mm radius spherical cavity with uniform temperature wall. The cavity is also filled with a low-pressure helium gas. The design concept shown in Fig. 5–19 corresponds to the "Ring7" model of the thermal analysis. It performs well thermally with only a 0.20% maximum heat flux variation around the outer surface of the DT ice. This is expected to directly correspond to the DT layer thickness variation.

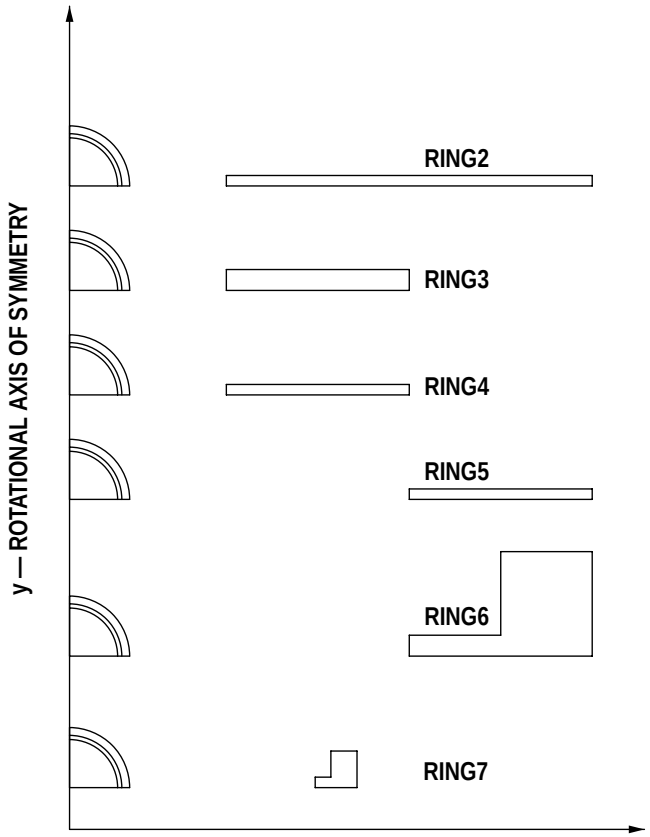

Fig. 5–20. The cryogenic target design of Fig. 5–19 has an inner seal ring geometry that was modeled as shown by Ring7. The mass of the total target in this concept is 0.5 gm. For use as scale, the capsule inner radius shown is 1 mm.

A finite element stress analysis was also done on the inner and outer seal rings for the CAH target design in the case where they are being pressed together by the assembler. The load pressure used to model the seal compression corresponds to 507 N (114 lbf) on the top face of the inner ring. This is typical of what was used in the experiments that were done on the 9 deg cone seals. The modeling was done in COSMOS/M using its nonlinear module. The model is an axisymmetric model of two

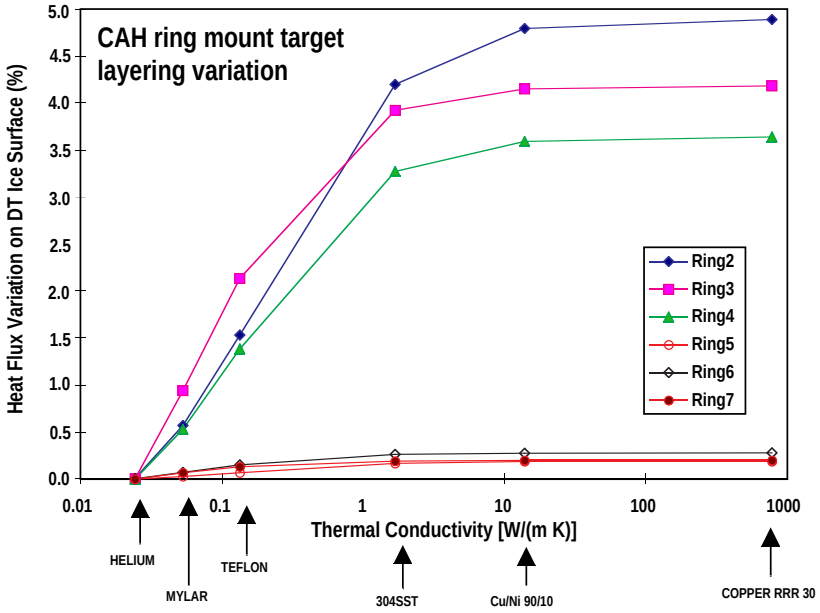

Fig. 5–21. Even when the inner seal ring is made up of copper, the maximum variation in heat flux, which corresponds to DT layer thickness variation, is below 0.2% for Fig. 5–19 design of a cryogenically assembled cryogenic target — see Ring7 results. The thermal conductivity of representative materials at 18 K is also shown on the thermal conductivity axis.

parts: the upper inner ring to which the hohlraum would be attached, and the upper half of the outer (mounting) ring to which the capsule's support film would be attached. The bottom surface of the mounting ring is constrained to remain on the x-axis, which inputs the reflection symmetry of the full problem of two seal rings being attached to the full mounting ring — one from the top and one from the bottom. Contact elements were put on the touching surfaces of the inner and outer rings to prevent them from passing through or into each other. The very soft truss elements connected to the inner ring prevent singularities in the stiffness matrix. The elements of the model are shown in Fig. 5–22. The Von Mises stress is shown in Fig. 5–23.

The stresses induced into the copper when the seal rings were forced together were high. Portions of the inner ring had stresses of up to 2900 kg/cm^2. The ultimate yield strength of annealed C10100 (OFHC) copper at 18 K is about 4000 kg/cm^2 according to NIST Monograph 177. The parts should survive, but experiments should be conducted to gain experience with parts that are strained this highly. In the model, the inner ring's inside surface was deformed inwards by about 10 μm when the seal was closed. The outer ring's inside surface was deformed outwards by about 4.6 μm when the seal was closed. These deformations were input into a symmetric shell model of the hohlraum. This model looked at stress and deformations induced into the hohlraum by the deformation of the inner and outer rings during the sealing process.

Seal/24

Axisymetric (about y-axis), Plane 2D Elements (2 DOF)

Material: Copper (20 K)
Units: MKS (COSMOS/M)

Integration:
Full Integration
Displacement: Updated Langragian

Pressure:
Pressure = 401.25 kg/cm^2 (114 lb force)

Pressure Range:
Start: 0
End: 1
Increment: 1

Pressure Convergence:
Slope = 1/1

Boundary Conditions:

Gap Distance = 0.11 mm

Constrained in the y-direction at bottom

Soft Trusses: Elastic Modulus = 0.005

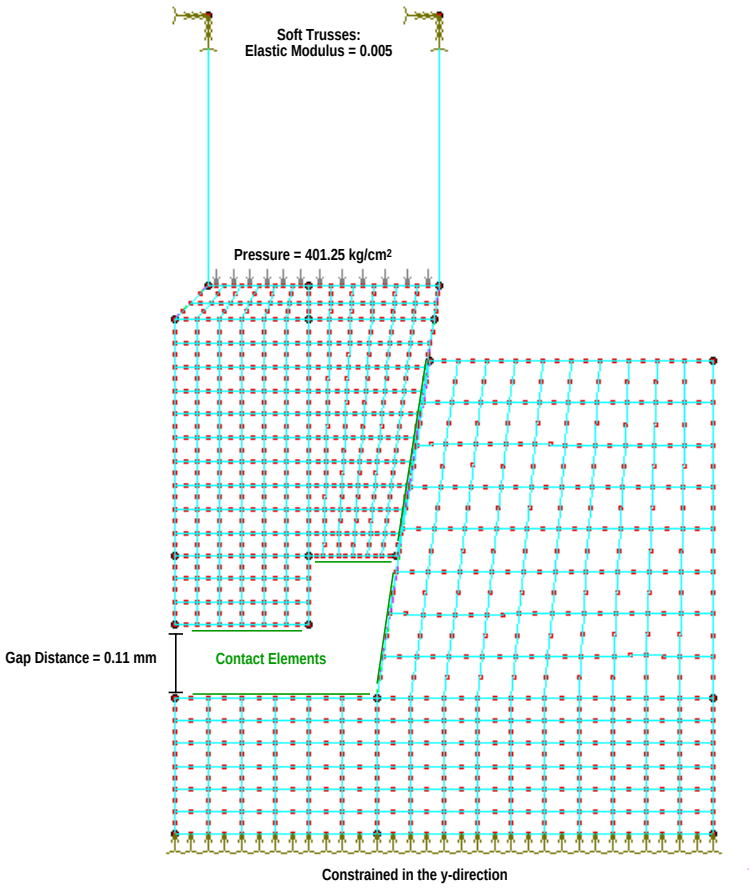

Fig. 5–22. The elements, constraints, and loads used for the stress analysis of the model. Since the elements are axisymmetric, these entities represent rings. Note that contact elements were put on the surfaces of the inner and outer seal rings to prevent the two items from passing through each other or into each other.

The axially symmetric shell model of the hohlraum had the displacement of its brim, calculated from previously described model of the inner and outer seal ring, imposed as a boundary condition. This corresponds to the movement of the inner and outer seal rings when they are pressed together during the hohlraum assembly process. The displacements used were obtained from results of the previously described model of the sealing process for inner and outer seal rings in the 9 deg cone geometry. The initial geometry and the displacements are shown in Fig. 5–24. The properties used for the gold of the hohlraum were an elastic modulus of 0.76×10^6 kgf/cm^2, a shear modulus of 0.27×10^6 kgf/cm^2, and a Poisson's ratio of 0.42.

The displacement of the hohlraum due to the sealing process is shown in Fig. 5–25 in a vector plot. The displacement of the hohlraum due to assembly process is 31 μm along the inner walls of the hohlraum. This means that the initial gap of the brim above the capsule's mounting film must be increased from 3 to 28 μm to avoid contacting the film and the other hohlraum half that would be coming up from below. The inner walls of the hohlraum experience very little radial displacement, most of the radial displacement is in the brim that connects that hohlraum proper to the inner seal

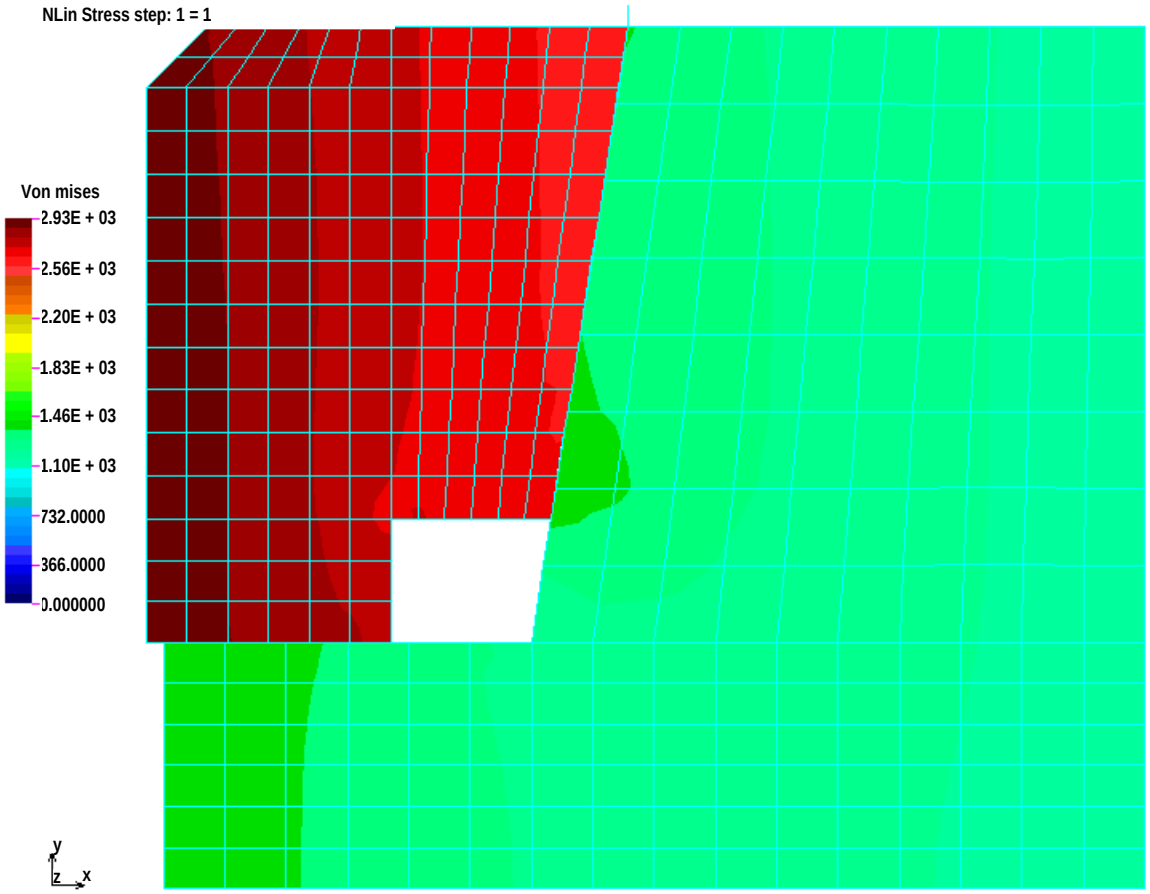

Fig. 5–23. The Von Mises stress is plotted in units of kg/cm^2 on the deformed plot of the inner and outer seal rings. Notice that the inner ring is now bottomed out on the outer ring. The inner ring is highly stressed, but this stress is below the ultimate yield strength of about 4000 kg/cm^2 for annealed C10100 copper at 18 K.

ring. The stresses in the hohlraum due to the assembly of the inner and outer seal rings are at the ultimate tensile strength of gold. The highest stress is in the element attached to the inner seal ring. The hoop stresses for this element range from 860 kg/cm^2 to 1720 kg/cm^2 and the meridian stresses from 120 kg/cm^2 to 600 kg/cm^2. Gold's ultimate tensile strength can range from 1100 kg/cm^2 for well annealed high purity gold to 2200 kg/cm^2 for work hardened gold. Gold has a 24% elongation at failure. The gold will yield and deform to relax the stress. A computer code capable of large deformations will be needed to accurately predict the final configuration and stress. Further investigation will be needed to determine if the stresses in this region will present a problem.

This design of a cryogenic hohlraum appears to be feasible. However, due to the high stresses that the model predicts for some of the parts, real physical parts will have to be built and assembled to verify this design for a CAH.

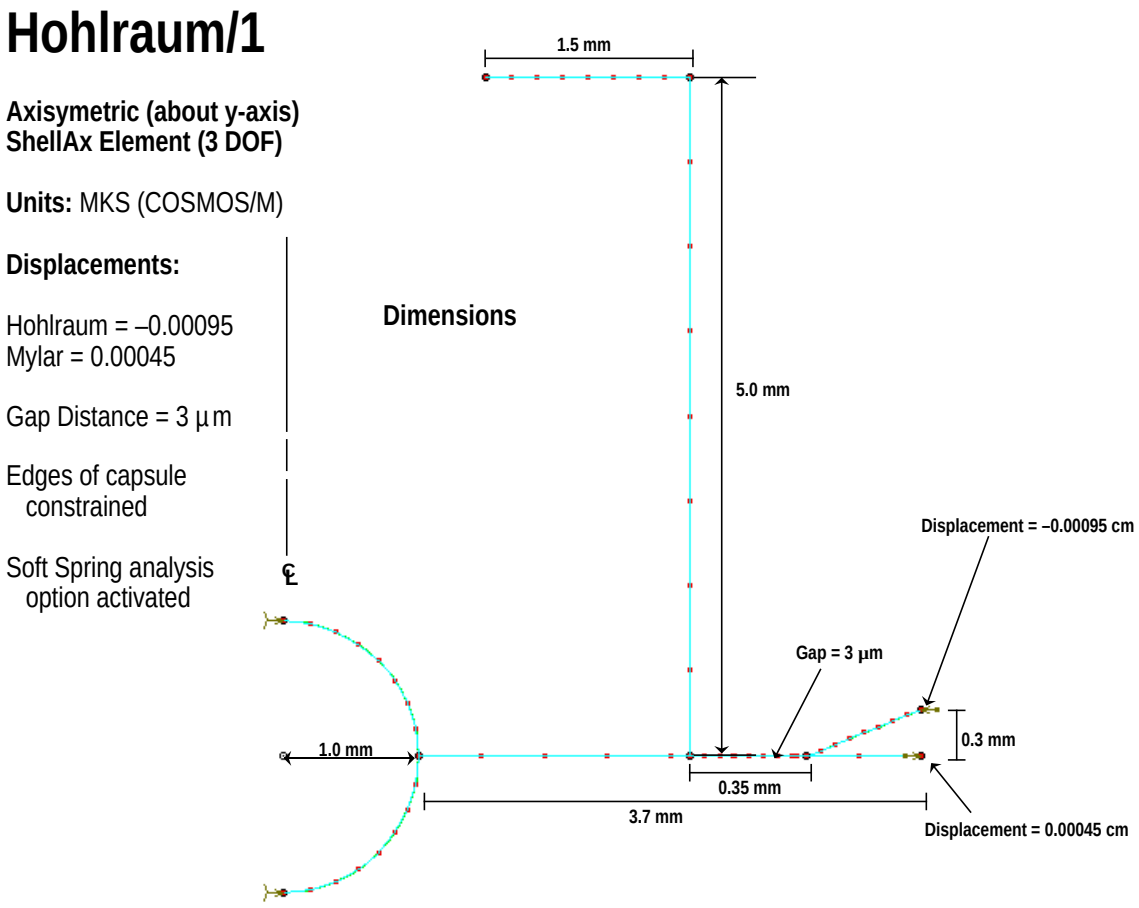

Fig. 5–24. An axially symmetric finite element shell model of the CAH NIF target was built and loaded with radial displacements corresponding to the movement of the inner and outer seal rings.

5.3.2. SEALS TESTS IN SUPPORT OF CAHs

To support the design and analysis effort for developing a CAH target, a number of tests were conducted on potential seal designs for fastening the hohlraums together. Two main styles were tested, the tapered cone seal, and a straight interference seal between cylinders. The test fixtures were designed only to investigate the seal. A sketch of one of the cone seal test fixtures is shown in Fig. 5–26.

For a seal to be successful, it must hold together and have a low leak rate while zero applied force holds it together and about 0.5 to 1 atm (8 to 15 psi) of helium is applied to its interior (simulating the tamping gas pressure at 18 K). The interference seals tested all had high leak rates, producing large quantities of large bubbles in Snoop when pressurized. These seals were diamond-turned copper with a diameter of 1/2 in. and interference fits of 0.0005 and 0.001 in. Copper cone seals that had cone angles of 45 and 50 deg, and used 0.002 in. thick indium gaskets failed to hold together when gas pressure was applied. These were sealed with up to 200 to 300 lb of force. The results for 9 deg cone

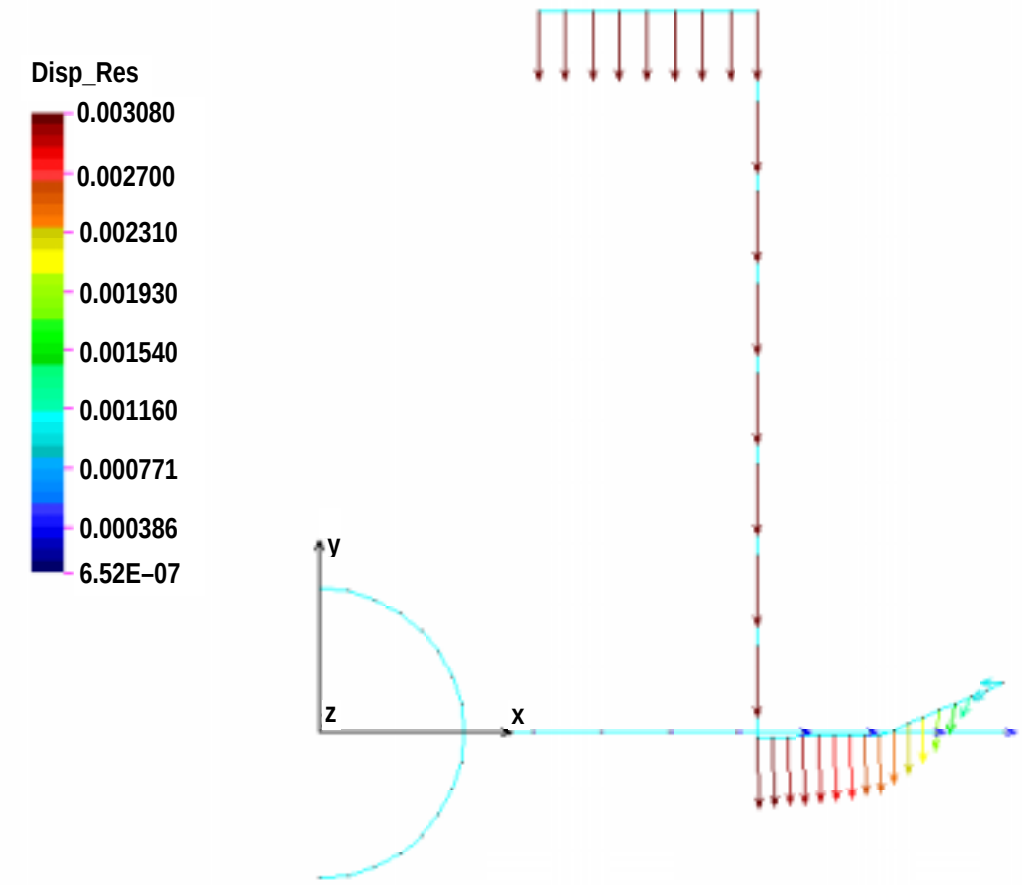

Fig. 5–25. The displacement of the hohlraum due to assembly process is 31 μm along the inner walls of the hohlraum. This means that the initial gap of the brim above the capsule's mounting film must be increased from 3 to 28 μm to avoid contacting the film and the other hohlraum half that would be coming up from below. The scale is in centimeters. The inner walls of the hohlraum experience very little radial displacement, most of the radial displacement is in the brim that connects that hohlraum proper to the inner seal ring.

seals were quite varied. With an 0.002 in. indium gasket, one sample tested at room temperature, leaked at a rate of 2×10^{-9} STD mbar l/s, but a force corresponding to an internal pressure of only slightly more than 1.2 atm (18 psi) separated the sample. Another sample with indium plating yielded leaks larger that the leak detector could detect. Five more samples of 9 deg cone seals were tested, three were sealed at room temperature and two were sealed at cryogenic temperatures of approximately 20 K. The material was straight copper except for one of the cryogenic tests which had silver plated on top of the seal flange faces. Additionally, a copper cone seal with 8.5 deg male cone inserted into a 9 deg female flange was tested.

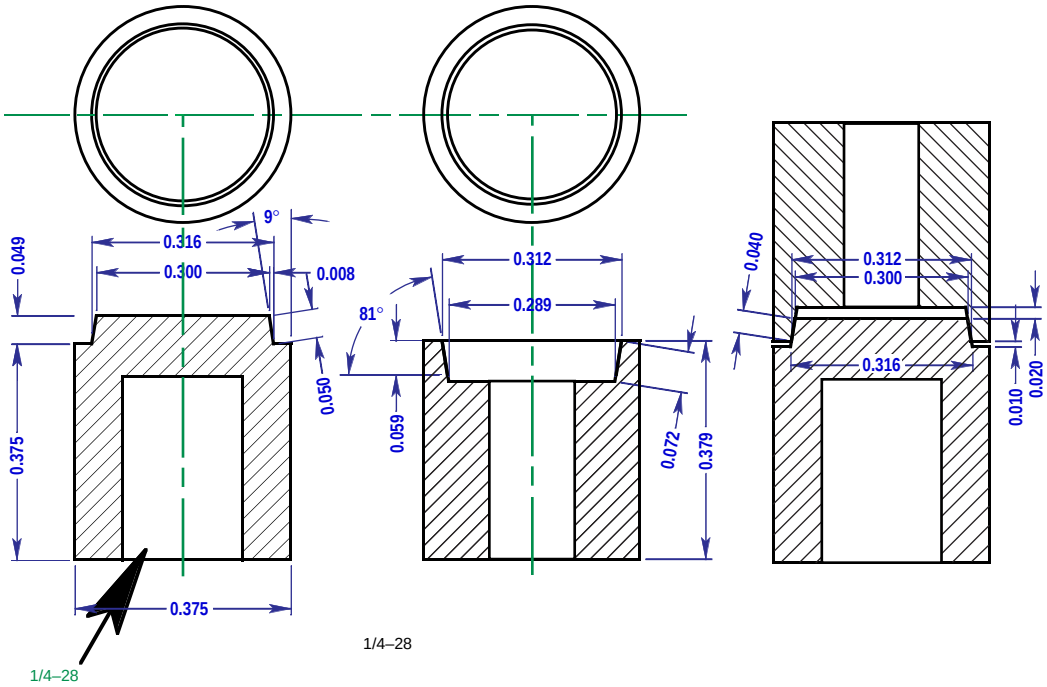

Fig. 5–26. Sketch of the 9 deg cone seal test pieces: on the left is the male cone, in the middle is the female, and on the right they are shown mated.

When quantitative leak rate measurements were obtained on the bare copper 9 deg cone seals, the leak rates ranged from the 7×10^{-10} STD atm cc/s (helium) range to 3 STD atm cc/s. The former result was a room temperature test with an applied helium pressure of 690 kPa (100 psi) and used 980 N (220 lbf) to set the seal. The larger leak rates were measured by timing the pressure drop of a fixed volume of helium gas attached to the seal test piece. The smaller leak rates were determined with a helium mass spectrometer leak detector. Where possible, the initial and final tilt of the flange faces and the amount of overlap of the cones at their initial contact were looked at. There was no clear trend as to when the seals performed well and when they perform poorly. Possible causes are the variability of manufacturing tolerance, surface finish tolerance, alignment tolerance during the sealing process, and cleanliness. The first two could be addressed in the future by switching manufacturing to a diamond turning lathe from the current standard machine engine lathe. The alignment can be addressed by providing a bearing aligned fixture to hold the parts during sealing. Moving the tests to a clean room laboratory would help to eliminate surface contamination from causing seals' leak rate variability.

The lowest leak rates obtained from the cone seals are likely low enough to be used for a CAH target that is assembled at the center of the NIF Target Chamber. However, much work needs to be done before the cone seals are understood well enough that this can be done reliably.

5.3.3. CONCEPTUAL DESIGN FOR D_2 TEST SYSTEM CRYOSTAT

A conceptual design for a cryostat for the D_2 Test System was produced. The cryostat is to be used to house a permeation cell and cryogenic manipulator for full-scale NIF cryogenic target assemblies. A target assembly consists of an indirect target, its cooling support rods, and a small robust base for manipulators to handle. The full test system is to be used to fill targets to full density with deuterium in the permeation cell, to remove a target from the cell to where it can be observed and layered, and to test key components and interfaces for the NIF Cryogenic Target System. The concept was modeled in 3D solid CAD. A section of this model is shown is Fig. 5–27. The walls of the cryostat have been sized to be in accordance with the ASME code Section VIII, where the inner and outer walls were sized to handle a pressure differential of 1 atm (15 psi) in both a crush and burst direction. Thermal analysis of the cooldown has begun. This is being done with GA's finite difference, transient, thermal analysis code, TAC–2D. While initial results are still under review, they indicate that the cryostat can be cooled in under 8 h to 15 K. This was for a condition of using 1 g/s of 6 K helium gas running through tubes wrapped around the cryostat's inner vessel and just the top of its shield. A stand for the cryostat was modeled in ANSYS. The cryostat was supported so that its cylindrical axis was horizontal, supported at one or both ends. The analysis looked at the movement of the cryostat shells, where the windows are located, with respect to the top of an optical table that the stand is attached to. The optical table was modeled as sitting on vibration damping legs. The transmissibility of the legs and the optical table compliance curves were taken from the Newport catalog. The legs were driven by a power spectra density of 10^{-10} g^2/Hz, which Newport recommends for a typical quiet laboratory. The result is that the maximum expected motion of the windows with respect to the table top is 64 μm (0.25 μin.), when the outer vessel of the cryostat is supported from both ends and the cryostat's inner vessel and shield are supported from one end.

5.3.4. TARGET FIELDING SYSTEMS

A number of potential concepts for the NIF Cryogenic Target System, which fills targets with DT and cryogenically fields them in the NIF Target Chamber, were developed. They were discussed at the Tritium Filling Options Workshop held June 24, 1998, at GA. A pamphlet describing them was written for the meeting. The four concepts are the temperature shimmed hohlraum for beryllium capsules, the in-hohlraum diffusion fill, the in-chamber cryogenic assembly, and the ex-chamber cryogenic assembly. The consensus of the meeting was that attention should be focused on a concept that fills multiple target assemblies in a fill cryostat, cold transports them to a transfer station cryostat, mounts an individual target assembly onto a target insertion cryostat (TIC) (while it is connected to the transfer station cryostat), and layers and inserts the target using the TIC. The target assembly includes the indirect drive target, its sapphire support rods, and a small robust base (used by manipulators to grasp the assembly). The target's DT fuel would be layered in the target's capsule by temperature shimming the target's hohlraum. A work breakdown structure and schedule were started to aid with producing a cost estimate of this system. This will be completed in early FY99.

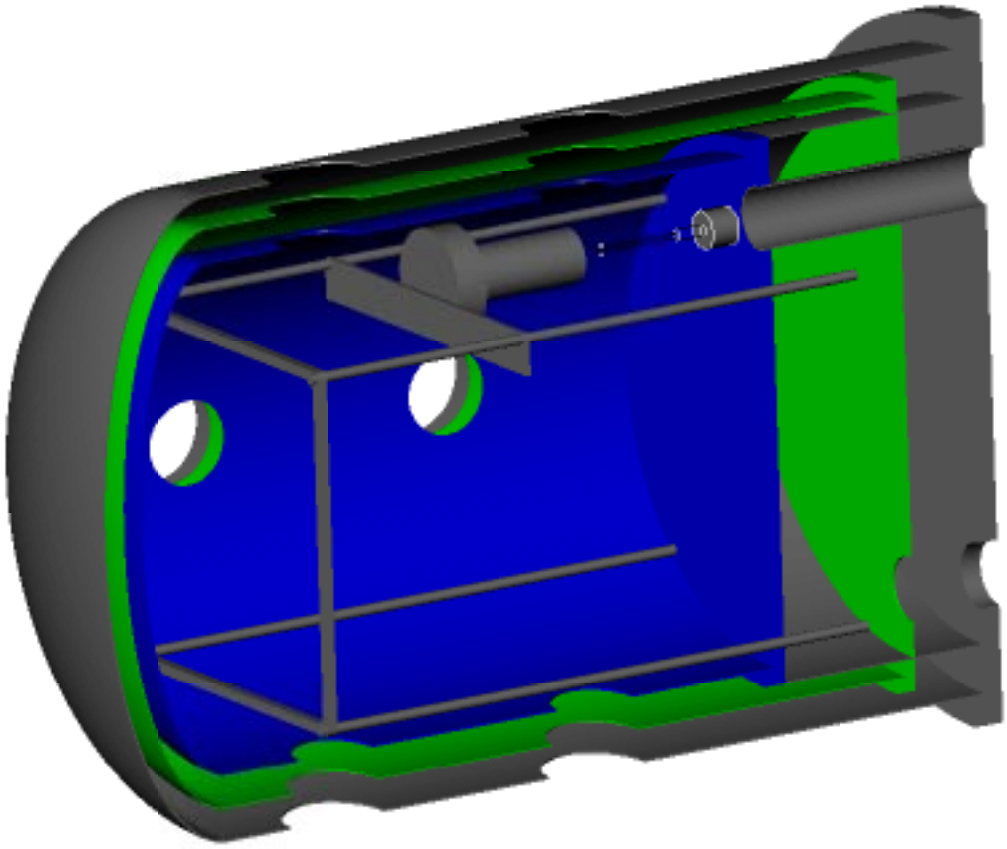

Fig. 5–27. The concept for the D_2 Test System cryostat is a helium gas stream cooled, multishell vessel, supported horizontally at both ends. Only the cryostat is shown, the stand and the cooling module have been omitted. The permeation cell is shown supported on a scaffolding attached to the inner vessel's base plate.

The cryogenic target fielding option of using a cryogenic target that is assembled cryogenically in the NIF Target Chamber was examined for issues that would prohibit or render this option impractical. The two most serious issues found were alignment of the lasers to the target and building the miniature, high precision, cryogenic assembler. The laser beam alignment becomes problematic because the fully assembled target will only be available in fully assembled form for approximately 3 s before the shot. This is insufficient time to align the 192 beams and retract the target alignment system from the target chamber. The assembler is a difficult project due to the required high precision, high force, low heating actuators that must be miniaturized to fit inside of the TIC shroud. The position resolution required for the assembler mechanism is on the micron level and the force requirements are anticipated to be in the 45 to 450 N (10 to 100 lbf) range. The heat of the assembler's actuators must not heat the target by more that a few tenths of a degree Kelvin.

A potential solution for the laser alignment issue was proposed. This solution would use a surrogate target and TIC to align the beams around a point in the chamber. The surrogate would be removed and the real target placed at the same point in the chamber. Unfortunately, this would

involve modifying the chamber center reference system (CCRS) to measure the location of fiducials on the TIC, adding a metrology station to determine the target to the TIC's fiducial location offset, and it depends on the NIF Target Chamber, optics, Target Positioner, the metrology station, and the TIC to hold their dimensions to the one micron level over the time span required to swap in the surrogate and real targets; likely to be several hours. While this solution is conceivable, a lot more work is required to show that it is practical for the NIF. The NIF's design and construction already determine its dimensional stability and temperature stability. On meter-sized components, only small temperature variations can cause micron level size changes. In addition, the expense of modifying the CCRS to measure TIC fiducials and adding a metrology station for TIC's may make this solution impractical.

For further information, please contact Dr. N. Alexander (GA).

5.4. REFERENCES FOR SECTION 5

[5–1] Project Staff, "Inertial Confinement Fusion Target Component Fabrication and Technology Development Support, Annual Report to the U.S. Department of Energy, October 1, 1996 through September 30, 1997," General Atomics Report GA–A22816 (1998) p. 5–7.

[5–2] Project Staff, "Inertial Confinement Fusion Target Component Fabrication and Technology Development Support, Annual Report to the U.S. Department of Energy, October 1, 1996 through September 30, 1997," General Atomics Report GA–A22816 (1998) p. 5–15.

[5–3] P.C. Souers, *Hydrogen Properties for Fusion Energy*, University of California Press, 1986, p. 3.

[5–4] T. Bernat, "The Limits to the Smoothness of Solid Hydrogen-Isotope Surfaces," Proc. 11th Target Fabrication Specialists Meeting, September 8–12, 1996, Orcas Island, Washington.

[5–5] LabView is produced by National Instruments, 6504 Bridge Point Parkway, Austin, Texas 78730-5039.

6. OMEGA TARGET SYSTEM ENGINEERING

During the past year, the team of the University of Rochester/Laboratory for Laser Energetics (UR/LLE), Los Alamos National Laboratory (LANL) and GA/Schafer made great progress in the design, procurement, installation, and testing of the OMEGA Cryogenic Target System (OCTS). The team accomplished the following major achievements in FY98: (a) the design phase was concluded for all components of the OCTS; (b) nearly all major components were procured by UR/LLE and/or fabricated; (c) the majority of the Fill/Transfer Station and associated components were assembled, tested, and shipped to UR/LLE; (d) significant portions of the moving cryostat (MC) and moving cryostat transport cart (MCTC) were assembled and tested; and (e) the upper pylon housing and vacuum feedthrough, provided by UR/LLE, were installed at the GA test facility.

Remaining procurement and assembly tasks include delivery and assembly of the MC thermal shrouds, final assembly of the MC and the MCTC, and delivery of the shroud puller linear motor, lower pylon, and chain locker. These tasks are scheduled for completion in the second quarter of FY99 with shipment to UR/LLE in May 1999.

The year was not without its challenges, however, and a review of the difficulties is useful from a lessons-learned viewpoint. Many of the difficulties were associated with the inability of vendors to supply and fabricate components on schedule. At year's end, the fabrication of the fill transfer station (FTS) cryostat was incomplete. The specifications for this cryostat were provided by GA on April 30, 1997, and one year was allowed for its fabrication and delivery. The absence of the FTS cryostat at GA resulted in substantial replanning of the work, culminating with performing the mechanical checkout of FTS components on "surrogate plates" that were provided by UR/LLE to simulate the geometry of the cryostat. While this strategy worked well for mechanical testing purposes, no cryogenic testing of the FTS was possible prior to shipment of the FTS-related components to UR/LLE. Cryogenic testing will be done in FY99 at UR/LLE with GA support.

Additional difficulties were encountered with the supplier of the FTS target manipulator, inserter manipulator, and shroud cooler drive units. In this case, mechanical components were delivered but pervasive software problems prevented proper functioning of the systems. UR/LLE is preparing revised control system software.

The supplier of the linear motor for the upper pylon met with significant delays during testing of the motor, and the unit was being shipped to UR/LLE for additional control and data acquisition system work at the end of the year.

The design of the MCTC umbilical spooler had to be revised during this year. Rolling friction in portions of the spooler was much higher than expected resulting in poor initial performance. After

initial testing of the complete spooler system, modifications were identified and implemented (better quality bearings), resulting in excellent performance during a long-term operational test.

The technical difficulties with the umbilical spooler reflect the need to fully understand and accurately determine the controlling factors in an equipment design and, most importantly, assure that those factors are adequately reflected in the prototyping and testing process.

The vendor difficulties reflect the need to evaluate the choice of vendors with respect to cost, but also to critically evaluate their ability to deliver components on-time, and to be realistic about the time needed for such deliveries. It is important for the contractor to ensure that the vendor has delivered similar systems and fully understands the task being undertaken. A contributing factor in the case of the OCTS was the procurement arrangement between GA and UR/LLE, whereby GA provided the technical specifications and interface but UR/LLE handled the contracting task. It is recommended, in the future, that one organization be held responsible for all aspects of achieving results in the procurement process.

6.1. FILL/TRANSFER STATION (FTS) EQUIPMENT TESTING

The FTS comprises about half of the OCTS and is located in the Tritium Lab, Room 157, at UR/LLE.

6.1.1. DT HIGH PRESSURE SYSTEM

The DT high pressure system's function is to slowly permeation fill the OMEGA targets with DT fuel gas to densities as high as 0.157 g/cm^3 using at most 1.67 g of DT. UR/LLE has responsibility for this system. A major component of this system is the compressor being supplied by Fluitron. GA has provided technical input and advice and acted as technical liaison for the compressor throughout the year. The technical specifications for this compressor were supplied by GA in August 1996. At the end of FY98, Fluitron was conducting high-pressure testing of the compressor at the vendor's site.

6.1.2. FILL/TRANSFER STATION (FTS)

The FTS's function is to house four targets as they are permeation filled, to cool them to cryogenic temperatures (~20 K), and to transfer them individually to an MC. A sketch of the FTS is given in Fig. 6–1. Due to vendor delivery delays, the FTS cryostat was not received at GA during the year. Instead, surrogate plates simulating the FTS geometry were fabricated by UR/LLE and used for mechanical checkout and fitup of the many FTS components.

A stand simulating the geometry of the FTS glove box was fabricated by UR/LLE and installed at GA. The surrogate plates, MC interface flange, electrical systems, vacuum systems, compressed air, helium supply lines, gate valves, cooling module spool piece, and all ancillary components were installed on this stand for testing purposes. Wiring harnesses for the FTS control system, including temperature sensors, heaters, and limit switches, were prepared. Overhead wire-ways were installed for routing of the control system and power lines. A programmable logic controller (PLC) for

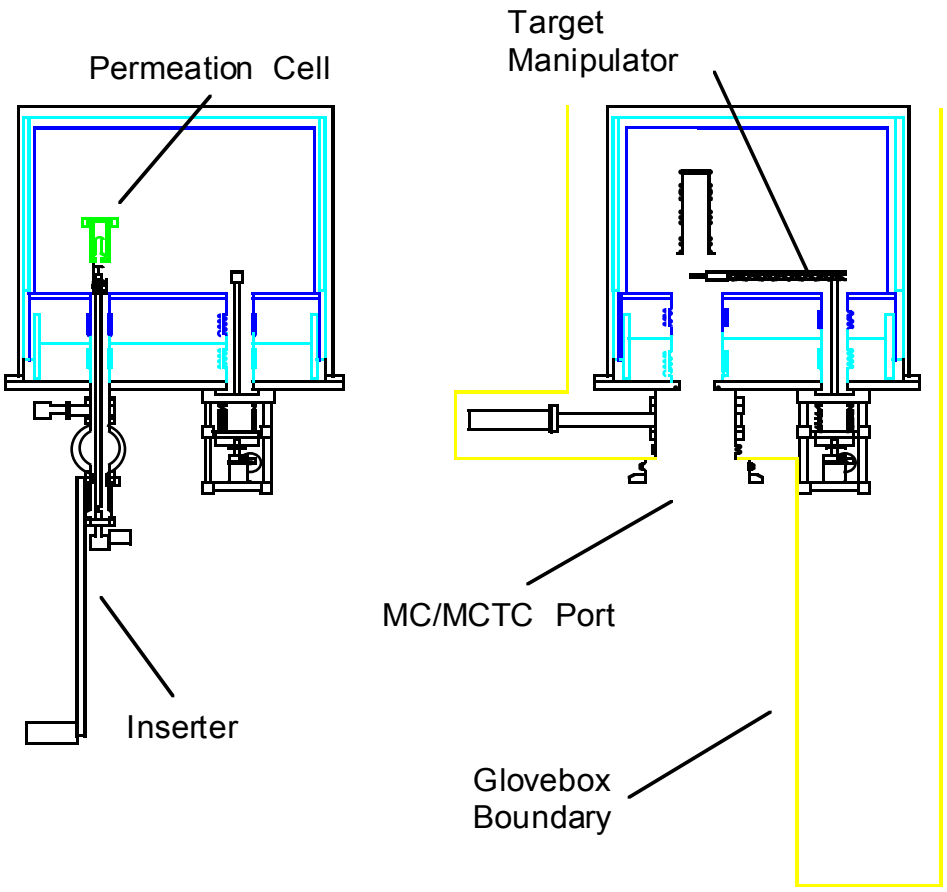

Fig. 6–1. FTS section views.

temperature readout was received from UR/LLE, and sensors were hooked up to the PLC and their readings verified with liquid nitrogen. Selected sensors were also checked with liquid helium. Heater controllers and solid state relays for the helium supply lines and for the FTS O–ring heaters were installed and checked out. A heater overtemperature alarm and shutdown system for the heaters was installed and checked out. Wiring for the FTS limit switches was completed, a corresponding PLC module was installed, and the limit switch LED readouts were checked. Temperature sensors were installed in the inserter, and the inserter wiring feedthrough was prepared.

Major subcomponents of the FTS are the cooling module, the target manipulator, the target inserter, the shroud cooler, the stalk aligner, and the permeation cell. Testing of these subcomponents is described below.

The cooling module (Fig. 6–2) provides refrigeration to the FTS. It consists of a cryostat with an integral liquid nitrogen bath, eight cryocoolers, and five supercritical helium cooling loops. The cooling module was received at GA (in this case delivery was about one month earlier than originally planned), and moved to its final position underneath the FTS stand.

The surrogate plates were removed from the stand and the FTS spool piece was installed. Wiring harnesses were prepared and interfaced to the readout system supplied by UR/LLE. Temperature sensors were verified with liquid nitrogen and selected sensors were checked with liquid helium. Liquid nitrogen was introduced into the tank. The helium compressors were setup and the coldheads were installed and operated. The second stage of all coldheads reached temperatures between 6 and 8 K. The recuperative heat exchangers were fabricated at GA and installed. The cooling module control panel was laid out and all valves, regulators, solenoids, and gas lines were assembled. The

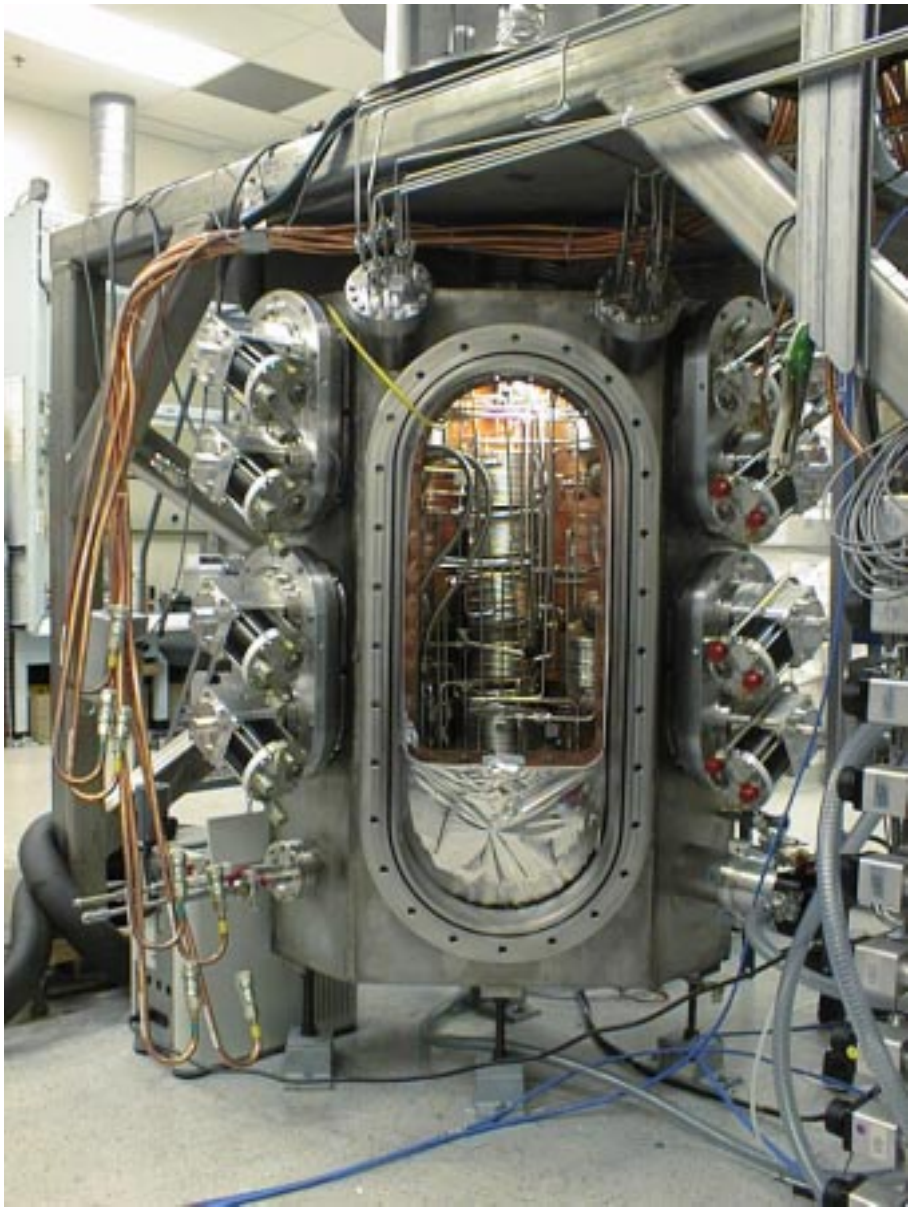

Fig. 6–2. Cooling module supplies refrigeration to the FTS.

cooling module internal plumbing was laid out, installed, and leak checked. The cooling module was closed, evacuated, and the five helium loops from the cooling module to the FTS were purged, back-filled, and vacuum leak checked. Jumpers were added in the place of the FTS for cooling module testing purposes. The cooling loops were individually tested for flow performance at room temperature. One of the five mass flow controllers was found to be defective in its operation and was replaced. Otherwise, the room temperature flow behavior was as expected.

The target manipulator removes individual mounted filled targets from the target rack and places them onto the MC stalk. This device is a computer-controlled four axis (x, y, z, theta) precision manipulator with a precision rotary motion vacuum feedthrough. It is driven by stepper motors which are located, along with all mechanical parts, at room temperature outside of the FTS. The manipulator was installed on the FTS surrogate plates for fitup and mechanical testing during the year. Although the software supplied was a preliminary version, the device was utilized to successfully move target mounts from a simulated target rack to a simulated MC stalk. As testing progressed, however, a large number of software (and some hardware) issues were found during the testing of the target manipulator at GA. Attempts by the vendor to repair the software resulted in additional bugs being created. At year's end, UR/LLE was preparing to replace the manipulator controls with a completely different control system.

The inserter manipulator places a target rack into the permeation cell and also rotates the target rack to (a) close the cell breech lock and (b) allow the target manipulator to pick up individual targets. This manipulator is similar to the target manipulator (same vendor and same control system) except that it has only two axes (Z and theta). The device was tested at GA and performed its intended mechanical functions well. However, it was operated only in a manual mode due to the software problems described above. Temperature sensors were installed in the inserter, and the inserter wiring feedthrough was prepared.

The shroud cooler (Fig. 6–3) incorporates a similar drive manipulator to provide the force for lifting the MC shroud inside the FTS. The manipulator is a one-axis (theta) device provided by the same vendor as discussed above. It operated well in a manual mode to drive the shroud lifting mechanism. Since it shares a control system with the two other manipulators described above, it was not operated under computer control.

The stalk aligner (Fig. 6–4) positions the MC stalk during target drop off and blocks heat from entering the FTS through the MC port. It is operated by helium pressurization of two bellows sealed pneumatic cylinders. The unit was installed on the FTS surrogate plates and tested at room temperature. It operated in a smooth and reproducible manner.

The permeation cell was proof-tested to 125% (~28,000 psi) of its working pressure and several leak tests were performed. The leak tests were conducted at a helium pressure of 22,000 psi and with the cell inside a vacuum chamber. The copper-plated seals supplied by the cell manufacturer were observed to have a thin and erratic layer of copper present and were ineffective in sealing the cell. However, placing a five mil thick copper foil over the seal plug resulted in no detectable ($<1.0 \times 10^{-9}$ mbar l/s) leak in multiple tests.

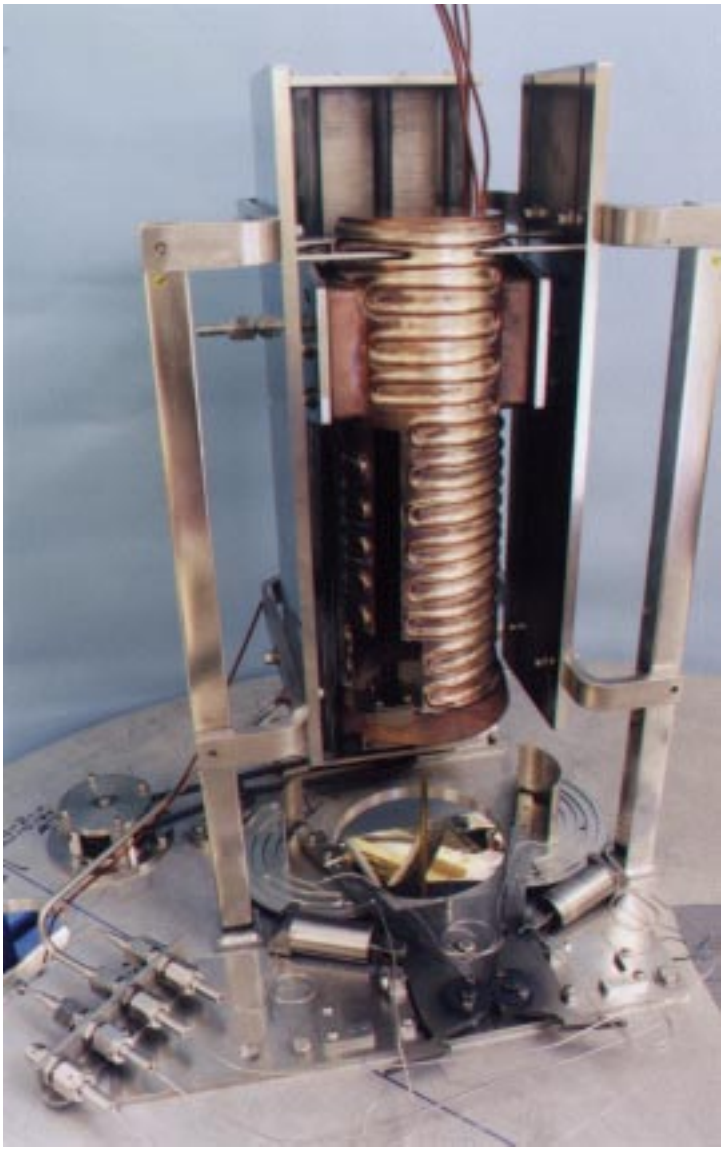

Fig. 6–3. Shroud cooler lifts and cools the MC shroud inside the FTS.

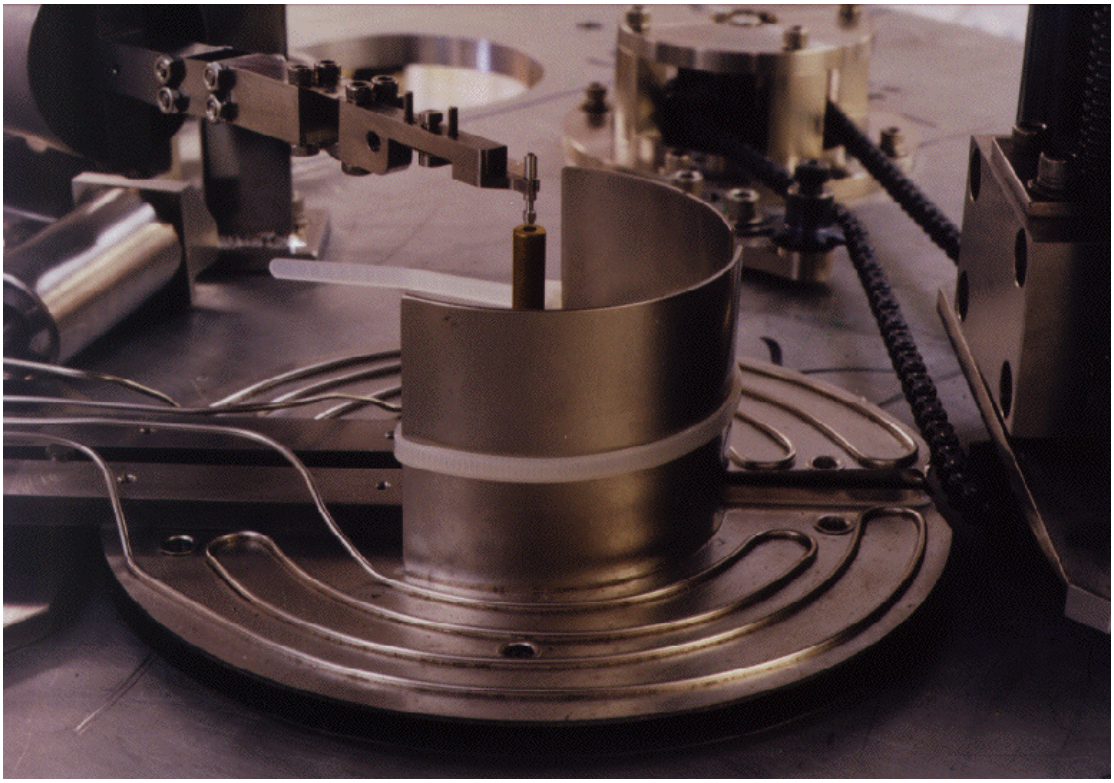

Fig. 6–4. Stalk aligner during placement of a simulated target.

For further information, please contact D. Goodin or C. Gibson (GA).

6.2. CRYOGENIC TARGET POSITIONING SYSTEM (CTPS) EQUIPMENT DESIGN

The cryogenic target positioning system (CTPS) comprises about half of the OCTS. It receives a filled cryogenic target from the FTS, transports it to the target chamber center, and precisely positions it in preparation for the laser shot. As part of this operation, the CTPS maintains the target at temperature and provides the environment required for target layering until milliseconds before the laser shot. This system consists of five subsystems: the MC, MCTC, lower pylon (LP), chain locker (CL), and upper pylon (UP). UR/LLE has taken on the responsibility for the final design and fabrication of the LP and CL.

Moving Cryostat (MC). The major MC subassemblies are the upper shroud, lower shroud, and fine positioner. All assembly and component drawings for the MC were released during the year, and all components for two MC's were ordered by UR/LLE. The parts for the lower one-third of the first MC have been received and assembled at GA. In addition, extensive electrical wiring work has been completed. Delay in the installation of the upper portions of the MC is due to the late delivery of the MC shrouds. The shroud assemblies are very complicated, which resulted in great difficulties finding a vendor and thus delays in delivery. To mitigate this, we designed surrogate shroud components that allowed us to successfully test the interface between the MC with the FTS. These parts provided a means to test the FTS shroud pulling and replacement process prior to shipment of the FTS. There will be a total of five MC/MCTCs needed for OMEGA. GA is building the first unit. Subsequent MC units will be assembled at UR/LLE. Figure 6–5 shows the partially assembled MC as it stood at year end with surrogate shroud parts installed.

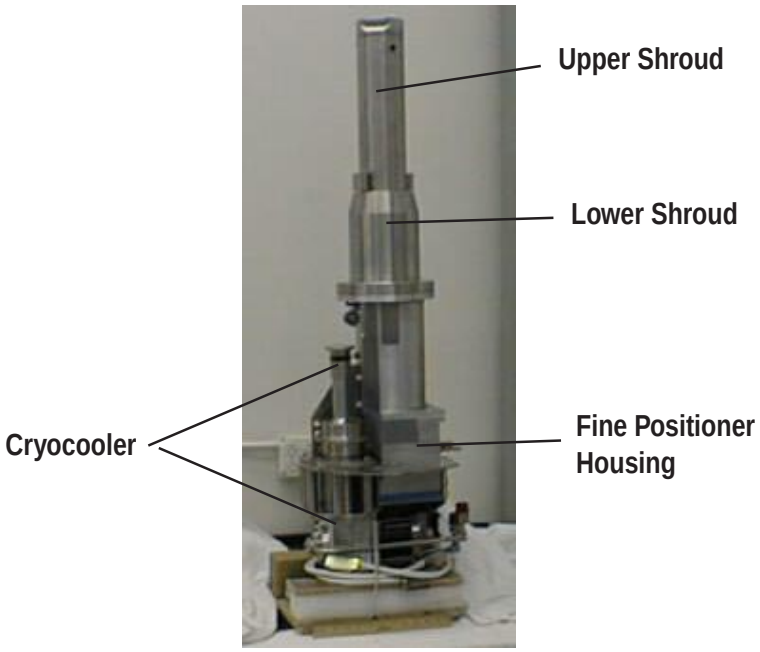

Fig. 6–5. Moving cryostat.

The fine positioner was assembled. Figure 6–6 shows the MC's fine positioner assembly. This assembly contains microstepping motors that enable the target to be moved in x, y, z, and theta axes. The motors for the linear and rotary stages have positioning resolutions of <30 nm and <0.3 mrad, respectively. In addition, the fine positioner assembly contains linear position transducers for the x, y, and z axes, and an absolute encoder for the theta axis. All electrical connections for this area have been completed, and all components have been successfully operated.

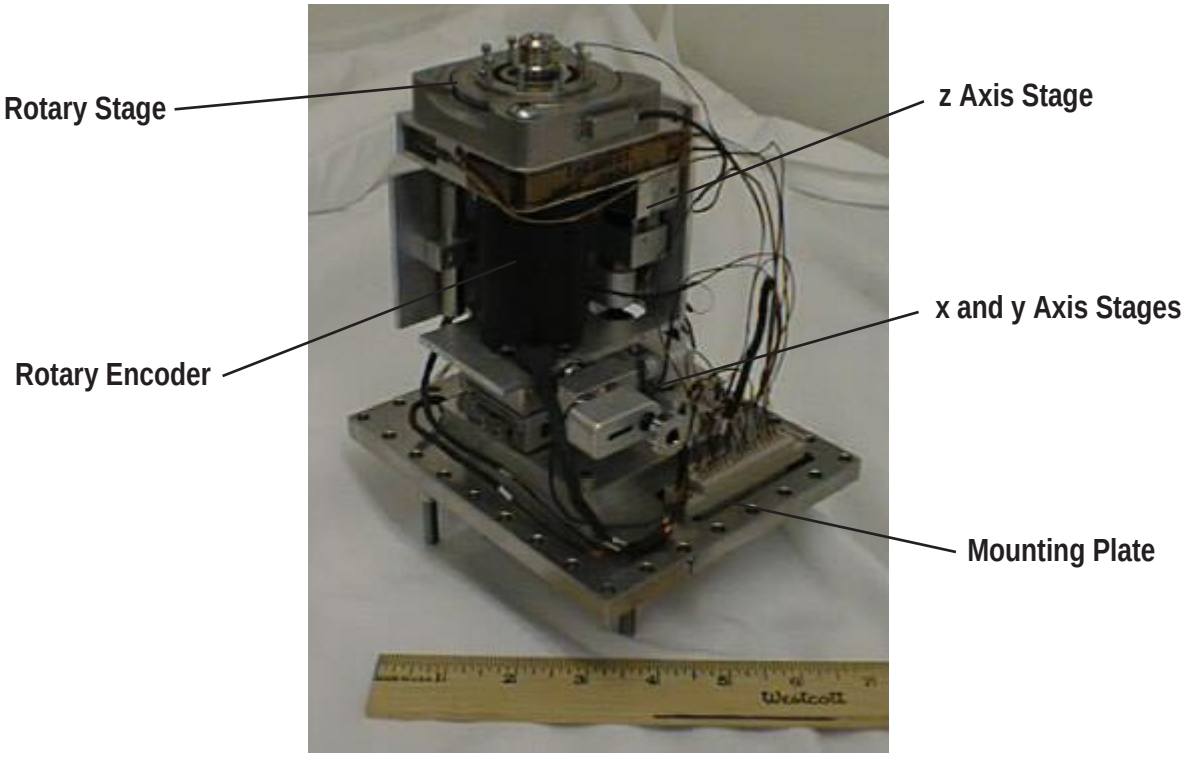

Fig. 6–6 Fine positioner.

Moving Cryostat Transport Cart (MCTC). The major MCTC subassemblies are the spooler and vacuum chamber. All assembly and component drawings for the MCTC were released during the year. Procurement of all components has been completed by UR/LLE for the first MCTC, and assembly work was more than 75% complete by year end. Components were also procured for the second MCTC, which will be assembled at UR/LLE.

Figure 6–7 shows the partially assembled MCTC. It weighs about 4000 lb and must be moved and precisely positioned at four process stations within the UR/LLE facility. These stations are the FTS, characterization station, prep station, and LP (target chamber). Four air casters are mounted under the vacuum chamber, and compressed air is used to float the MCTC on a thin cushion of air when it needs to be moved. Tooling balls are mounted to the MCTC which dock against locating surfaces when the cart is positioned at each process station. Tests were performed at UR/LLE which demonstrated that the MCTC can be repeatedly located within ±0.005 in.

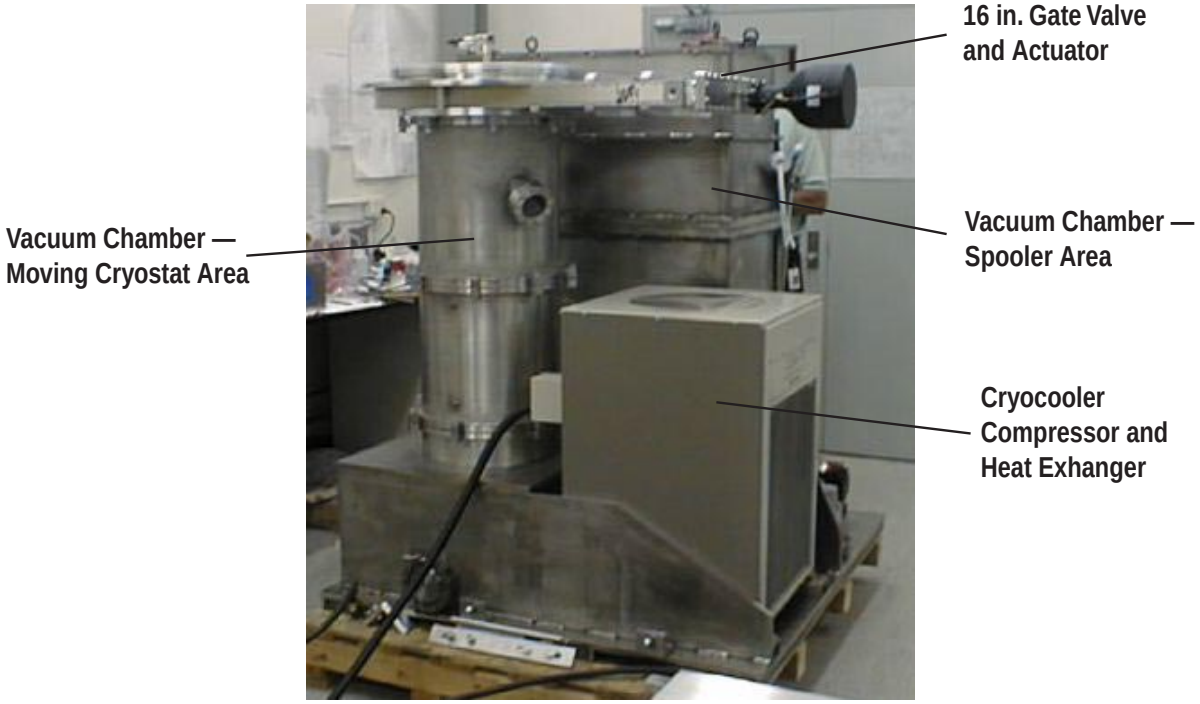

Fig. 6–7 Moving cryostat transport cart.

The umbilical spooler is an integral part of the MCTC. When the MC is deployed into the OMEGA target chamber, it is elevated 20 ft from its starting position. While in transit, the cryostat must continue to receive electric power, control signals, and pneumatic services from the MCTC, which remains outside the target chamber. The utility "umbilical" that provides these services consists of three electrical cables with a total of 130 conductors and 5 gas lines. When the MC returns to its home position, the umbilical must be recoiled and stored in the smallest possible volume due to space considerations in the MCTC. Because this entire process occurs in vacuum at 10^{-6} Torr, low leakage rates from the gas lines is essential, and rotary seals could not be used at the hose termination points.

The spooler was designed to accomplish this task. It consists of upper and lower carriages which contain banks of ball bearings, a linkage similar to a large scissor jack, pneumatic and metal springs, and the umbilical hoses and cables. The pneumatic spring is the primary driver and, via the scissor, pushes the upper carriage to its home position. The hoses and cables are wound over the carriages' ball bearing banks and span vertically between the two carriages as can be seen in Fig. 6–8. Low rolling friction in the bearing carriages is key to successful operation of the spooler. An operational test equivalent to 1 year of normal usage on OMEGA was successfully completed. Figure 6–8 shows two views of the spooler mounted in the test stand. The long-term test confirmed that the friction loads did not change noticeably over time.

The MCTC attaches to the FTS to receive a filled cryo target. The interface connection between these two systems needed to be tested. This process was successfully demonstrated and included docking the MCTC under the FTS, repeatedly locating it correctly, and connecting the interface

Fig. 6–8. Two views of the spooler.

flanges. Since the FTS had to be shipped to UR/LLE before the MC/MCTC was completely assembled, the portions of the docking process that involve the MC could not be demonstrated.

Upper Pylon (UP). The major UP subassemblies are the housing, vacuum feedthrough, shroud puller system, and gripper. All assembly and component drawings for the UP were released during the year. With the exception of the shroud puller motor, all components have been received. The UP housing and vacuum feedthrough have been installed at GA. Figure 6–9 shows the portion of this installation that is visible from the 17–ft elevation in Bldg. 35.

The shroud puller system is nearing completion. It has been operated at high velocities (up to 4.8 m/s) during factory acceptance tests. This linear motor operates in atmospheric conditions and provides the force and speed required to remove the MC shroud at precisely controlled acceleration and velocity profiles. The shroud puller system was shipped to UR/LLE at year end for final control and data acquisition work. It will be mounted inside the housing shown in Fig. 6–9.

The gripper is the component at the lower end of the UP assembly. It is the active interface between the shroud puller system and the MC. The gripper grabs the top of the MC's upper shroud, enabling the shroud puller system to remove it. After the shroud puller has lowered the gripper into position and it has engaged the shroud, a drive motor screws the gripper's compliant parts together, securing the grip. Fabrication of the gripper is complete, and UR/LLE was developing controls for it at year end.

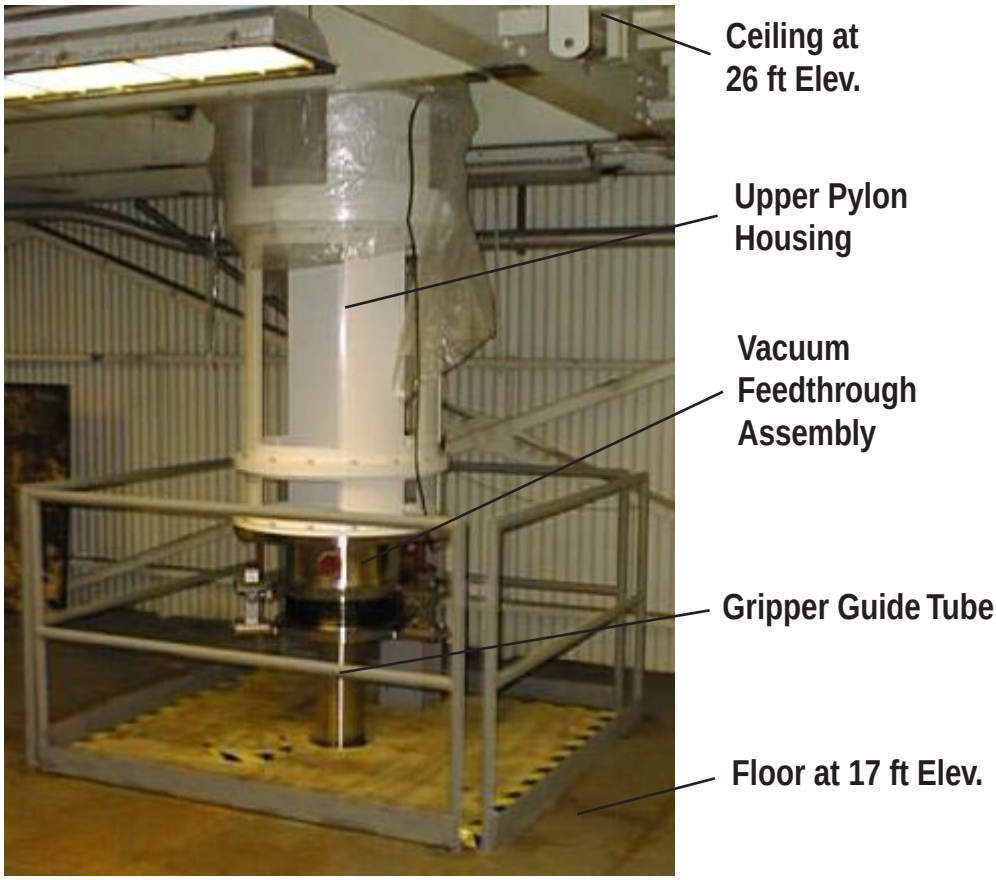

Fig. 6–9. UP segment installed at GA Bldg. 35.

Building 35 Test Facility. GA Bldg. 35 will be the primary facility for testing the fully integrated CTPS. The CTPS test installation requires about 35 ft of unobstructed height, provisions for lifting heavy equipment into place, and large amounts of electrical power (~60 kW peak). Building 35 is extremely well suited for this task. It has very high ceilings (up to 80 ft), large overhead cranes, and a heavy interior structure with flooring at convenient elevations. In addition, it is supplied with enough power at all voltages to meet the demands of the testing activity. The design and construction work required for making the necessary modifications to the building for the OCTS testing were completed during the year.

For further information, please contact K. Boline (GA).

6.3. OCTS SUPPORT SYSTEMS

Two major support systems for the OCTS were designed and constructed by the Tritium Group at Los Alamos National Laboratory, led by Dr. Art Nobile. GA provided interface information support to LANL for these tasks.

6.3.1. GLOVE BOX (LANL)*

The ability of the OCTS to safely contain tritium is critical to the successful operation of the system. Several major OCTS components will be placed within two glove boxes for tritium containment purposes. Last year the design of these glove boxes was completed, and a contract was awarded to Absolute Control Systems of Wheat Ridge, Co. for construction of the glove boxes. This year, both glove boxes were constructed. One glove box has completed final acceptance testing and has been shipped to UR/LLE. The second glove box is now undergoing final acceptance testing and is scheduled to be shipped to UR/LLE by the end of CY98.

One of the above glove boxes is unique in that it must contain and support the 3700 lb fill/transfer cryostat, and yet allow docking of the MCTC beneath the cryostat. This feature placed stringent structural requirements on the glove box. It was also a requirement that the glove box maintain its structural integrity during a seismic event. A review of the glove box final design earlier this year by a consultant on seismic issues was held to ensure that the glove box would meet the seismic requirement. During this review, the consultant recommended placing additional structural members inside the glove box. As a result of this modification to the design, the schedule for delivery of the glove box was delayed by about two months. However, due to similar delays in delivery of the fill/transfer cryostat, the overall schedule was not impacted significantly by the glove box delay.

6.3.2. VACUUM SYSTEM (LANL)*

The OCTS will require vacuum for operation of many components of the system. Two vacuum systems will be needed: one for the Room 157 equipment, and one for the La Cave equipment. Two vacuum systems have been designed to provide the necessary vacuum. The vacuum systems will need to handle a wide range of tritium levels, thus the systems have been designed with separate pumping manifolds that allow separation of evacuated gases with different tritium concentrations. This year, most of the vacuum components have been ordered and delivered. Installation of the vacuum system will begin after the glove boxes and fill/transfer cryostat are placed in Room 157 at UR/LLE.

*(*Note: This work was done by Art Nobile and Joe Nasise of LANL. Please contact them for further information.)*

7. PUBLICATIONS

Collins, G., Bittner, D., Moll, G., Monsler, E., Unites, W., Stephens, R., Tiszauer, D., Feit, M., Burmann, J., Sanchez, J., Maples, E., Bernat, T., "Forming and Smoothing D_2 and HD Layers for ICF by Infra-Red Heating," Bull. Am. Phys. Soc. **42**, 2009 (1997).

Elsner, F., "Thickness Distribution for Gold and Copper Electroformed Hohlraums," Proc. 12th Target Fab. Spec. Mtg., April 19–23, 1998, Jackson Hole, Wyoming, to be published in Fusion Technology; General Atomics Report GA-A22894 (1998).

Goodin, D.T., et al., "The Design of the Omega Cryogenic Target System," in Proc. 17th IEEE/NPS Symp. on Fusion Engineering, October 6–11, 1997, San Diego, California (Institute of Electrical and Electronics Engineers, Inc., Piscataway, New Jersey, to be published); General Atomics Report GA-A22714 (1997).

Goodin, D.T., et al., "Status of the Design and Testing of the Omega Cryogenic Target System (OCTS)," Proc. 20th Symp. on Fusion Technology, September 7–11, 1998, Marseille, France; General Atomics Report GA–A22900 (1998).

McQuillan, B.W., Greenwood, A., "Microencapsulation Process Factors which Influence the Sphericity of 1 mm o.d. Poly(-Methylstyrene) shells for ICF," Proc. 12th Target Fab. Spec. Mtg., April 19–23, 1998, Jackson Hole, Wyoming, to be published in Fusion Technology; General Atomics Report GA–A22850 (1998).

McQuillan, B.W., Elsner, F.H., Stephens, R.B., "The Use of CaCl and Other Salts to Improve Surface Finish and Eliminate Vacuoles in ICF Microencapsulated Shells," Proc. 12th Target Fab. Spec. Mtg., April 19–23, 1998, Jackson Hole, Wyoming, to be published in Fusion Technology; General Atomics Report GA-A22851 (1998).

Nikroo, A., Woodhouse, D., "Bounce Coating Induced Domes on Glow Discharge Polymer Coated Shells," Proc. 12th Target Fab. Spec. Mtg., April 19–23, 1998, Jackson Hole, Wyoming, to be published in Fusion Technology; General Atomics Report GA–A22869 (1998).

Nikroo, A., Steinman, D.A., "Enlargement of Glass and Plastic Shells to 2 mm in Diameter by Redropping Through a Short Heated Tower," Proc. 12th Target Fab. Spec. Mtg., April 19–23, 1998, Jackson Hole, Wyoming, to be published in Fusion Technology; General Atomics Report GA–A22870 (1998).

Nikroo, A., Steinman, D.A., "Thin Sputtered Glass as a Permeation Barrier for Plasma Polymer Shells," Proc. 12th Target Fab. Spec. Mtg., April 19–23, 1998, Jackson Hole, Wyoming, to be published in Fusion Technology; General Atomics Report GA–A22871 (1998).

Sater, J., Kozioziemski, B., Collins, G., Mapoles, E., Pipes, J., Burmann, J., Bernat. T., "Cryogenic D-T Fuel Layers Formed in 1 mm Spheres by Beta-Layering," to be published in Fusion Technology.

Sheliak, J., Hoffer, J., "Surface Roughness Statistics and Temperature Step Stress Effects for D-T Solid Layers Equilibrated Inside a 2 mm Beryllium Torus," to be published in Fusion Technology.

Stephens, R.B., McQuillan, B.M., Miller. W.J., "Prospects for 2 mm Diameter NIF Polymer Capsules," Proc. 17th IEEE/NPSS Symp. on Fusion Engineering, October 6–11, 1997, San Diego, California; General Atomics Report GA–A22732 (1997).

Steinman, D.A., Nikroo, A., Woodhouse, D., "Strengthening Large Thin Glass Shells by Overcoating with GDP," Proc. 12th Target Fab. Spec. Mtg., April 19–23, 1998, Jackson Hole, Wyoming, to be published in Fusion Technology; General Atomics Report GA–A22868 (1998).